

**Contact Stiffness and Dry Friction Damping
to Mitigate Turbomachinery Vibrations**

BY

FRANCESCO BECCARISI
B.S., Politecnico di Torino, Turin, Italy, 2014

THESIS

Submitted as partial fulfillment of the requirements
for the degree of Master of Science in Mechanical Engineering
in the Graduate College of the
University of Illinois at Chicago, 2016

Chicago, Illinois

Defense Committee:

Piergiorgio Uslenghi, Chair and Advisor

Farid M. L. Amirouche

Daniele Botto, Politecnico di Torino

ACKNOWLEDGMENTS

I would like to acknowledge my advisors, Professor M. Gola and Professor P. Uslenghi, for their continuous support, patience and immense knowledge. I would like to express my sincere gratitude to my co-advisor, Professor Daniele Botto, for his enthusiasm, motivation and crucial experience.

I would like to acknowledge my family, my parents Rossella and Sandro Beccarisi, and my little brother Carlo Alberto, for their love and assistance. Everything I realized, my successes and achievements, are the results of their wise guidance and infinite affect. I am grateful for the prestigious opportunity to study in an American university that they, and my grandparents Lucia and Donato Latino, gave me.

I would like to thank my girlfriend, Valentina Vergine, for her love and innovative ideas. She has been the main source of strength and happiness all this years of university.

Finally, I want to thank my friends and colleagues for their encouragement. No matter where they are around the world, they always make me joyful.

BF

TABLE OF CONTENTS

<u>CHAPTER</u>	<u>PAGE</u>
1 INTRODUCTION	1
1.1 Turbomachinery vibrations damping	1
1.2 Thesis methodologies and objectives	3
1.3 Analytical solutions	4
1.4 Thesis overview	4
2 CYLINDER IN CONTACT WITH A PLANE	6
2.1 Bodies design and mesh generation	6
2.2 Normal contact problem: analytical vs numerical solutions	8
2.2.1 Hertz contact model	9
2.2.2 Normal approach	10
2.2.2.1 Norden - 1973	10
2.2.2.2 Harris - 1991	10
2.2.2.3 Brandlein - 1999	11
2.2.2.4 Roark's Formulas - 2002	11
2.2.2.5 Johnson - 2003	11
2.2.2.6 Kosarev - 2011	12
2.2.3 Specific case: normal force=350 N	12
2.2.4 System behavior for several loading conditions	16
2.2.5 Cylinder compression influence in normal approach	19
2.2.5.1 Diameter and length effect in cylinder compression	23
2.2.6 Diameter and length influence in normal approach	25
2.2.6.1 Normal approach: numerical formulation	30
2.3 Tangential contact problem: analytical vs numerical solutions	32
2.3.1 Specific case: tangential displacement $du=2 \mu m$	33
2.3.2 Tangential displacement against tangential force	36
2.3.2.1 Tangential approach: numerical formulation	39
2.3.2.2 Frictional hysteresis loop	41
3 PLANE ON PLANE CONTACT	44
3.1 Bodies design and mesh generation	45
3.2 Normal contact problem	46
3.3 Tangential contact problem	49
3.3.1 Tangential displacement against tangential force	51
4 CONCLUSION	61

TABLE OF CONTENTS (continued)

<u>CHAPTER</u>	<u>PAGE</u>
APPENDICES	62
Appendix A	63
Appendix B	78
CITED LITERATURE	108
VITA	112

LIST OF TABLES

<u>TABLE</u>		<u>PAGE</u>
I	CYLINDER COMPRESSION INFLUENCE IN NORMAL APPROACH: DIAMETERS AND LENGTHS	23
II	DIAMETER AND LENGTH INFLUENCE IN NORMAL APPROACH . . .	26
III	NORMAL APPROACH: EXPONENTS COMPARISON	31
IV	DIAMETER AND LENGTH INFLUENCE IN TANGENTIAL APPROACH	37
V	NORMAL AND TANGENTIAL APPROACH: EXPONENTS COMPARISON	40
VI	STEEL POISSON'S RATIOS	85
VII	STEEL YOUNG'S MODULI	85

LIST OF FIGURES

<u>FIGURE</u>	<u>PAGE</u>
1 Dampers common shapes.	1
2 Dampers position and forces.	2
3 Half cylinder model: cylinder-plane contact.	7
4 Plane model: cylinder-plane contact.	8
5 Contact area comparison: cylinder.	13
6 Hertz pressure distribution: cylinder.	14
7 Numerical pressure distribution: cylinder.	14
8 Pressure distribution comparison 3D: cylinder.	15
9 Pressure distribution comparison 2D: cylinder.	15
10 Normal force vs dz: cylinder.	16
11 Contact area vs NF: cylinder.	17
12 Mean pressure vs NF: cylinder.	18
13 Bodies deformation.	19
14 Cylinder compression influence in normal approach.	20
15 Cylinder: body1 displacements.	21
16 Cylinder: body2 displacements.	21
17 Sphere compression influence in normal approach.	22
18 Cylinder compression influence in normal approach: length effect 1.	24
19 Cylinder compression influence in normal approach: length effect 2.	24
20 Sphere compression influence in normal approach: diameter effect.	25
21 Dz vs normal force: cylinders comparison.	27
22 Dz vs NF/L: cylinders comparison.	27

LIST OF FIGURES (continued)

<u>FIGURE</u>	<u>PAGE</u>
23 Dz vs NF/L: cylinders with equal diameter.	28
24 Normal force vs dz: cylinders 1 and 8 comparison.	29
25 dz vs normal force: numerical equation and results.	31
26 Stick/Slip areas: cylinder.	34
27 Tangential traction comparison 3D: cylinder.	35
28 Tangential traction comparison 2D: cylinder.	35
29 Tangential force vs tangential displacement: cylinders comparison CND case. .	37
30 TF/L vs normal displacement: cylinders comparison.	38
31 TF/L vs normal displacement: cylinders with equal diameters comparison. . .	39
32 Tangential force vs du: numerical equation and results.	41
33 Tangential force vs tangential displacement: cylinders comparison CNF case. .	43
34 Frictional hysteresis loop comparison: cylinders 1 and 4.	43
35 Damper 45°.	44
36 Damper model: plane-plane contact.	45
37 Damper model: plane-plane contact.	46
38 Numerical pressure distribution: plane.	47
39 Dz vs normal force: plane.	48
40 Mean pressure vs dz: plane.	48
41 Tangential traction distribution: plane.	49
42 Slip distribution: plane.	50
43 Stick/Slip nodes: plane.	50
44 Tangential displacement against tangential force: NF misalignment.	51
45 Eccentricity and pressure distribution: part I.	52
46 Eccentricity and pressure distribution: part II.	53

LIST OF FIGURES (continued)

<u>FIGURE</u>	<u>PAGE</u>
47 Tangential force vs tangential displacement: eccentricity comparison part I. . .	54
48 Tangential force vs tangential displacement: e0.	55
49 Tangential force vs tangential displacement: e1.	55
50 Tangential force vs tangential displacement: e2.	56
51 Tangential force vs tangential displacement: e3.	56
52 Tangential force vs tangential displacement: eccentricity comparison part II. .	57
53 Tangential force vs tangential displacement: e4.	58
54 Tangential force vs tangential displacement: e5.	59
55 Tangential force vs tangential displacement: e6.	59
56 Tangential force vs tangential displacement: e7.	60
57 Tangential force vs tangential displacement: e8.	60
58 Iterative procedure for normal contact problem.	64
59 Potential energy equation: elements display.	69
60 Iterative procedure for tangential contact problem.	72
61 Half sphere model: volume cutting technique.	80
62 Plane model: volume cutting technique.	80
63 Half sphere model: hard points projection technique.	81
64 Plane model: hard points projection technique.	82
65 Contact area comparison: sphere LNF.	86
66 Hertz pressure distribution: sphere LNF.	87
67 Numerical pressure distribution: sphere LNF.	87
68 Pressure distribution 3D: sphere LNF.	88
69 Pressure distribution 2D: sphere LNF.	88
70 Contact area comparison: sphere HNF.	89

LIST OF FIGURES (continued)

<u>FIGURE</u>	<u>PAGE</u>
71 Numerical pressure distribution: sphere HNF.	90
72 Hertz pressure distribution: sphere HNF.	91
73 Pressure distribution 3D: sphere HNF.	91
74 Pressure distribution 2D: sphere HNF.	92
75 Boundary conditions: normal problem.	93
76 Dz vs normal force: sphere.	94
77 Contact area vs normal force: sphere.	94
78 Max and mean pressure vs normal force: sphere.	95
79 Stick/Slip areas: sphere STD.	98
80 Numerical tangential force: sphere STD.	99
81 Mindling tangential traction: sphere STD.	99
82 Tangential traction comparison 3D: sphere STD.	100
83 Tangential traction comparison 2D: sphere STD.	100
84 Stick/Slip areas: sphere LTD.	101
85 Numerical tangential force: sphere LTD.	102
86 Mindling tangential traction: sphere LTD.	102
87 Tangential traction comparison 3D: sphere LTD.	103
88 Tangential traction comparison 2D: sphere LTD.	103
89 Slip: STD - LTD comparison.	104
90 Boundary conditions: tangential problem.	105
91 Tangential force vs du.	106
92 Stick area vs du.	107

LIST OF ABBREVIATIONS

AMS	American Mathematical Society
BC	Boundary condition
CA	Contact Area
CF	Centrifugal Force
CAL	Contact Area Length
CAW	Contact Area Width
CG	Center of Gravity
CND	Constant Normal Displacement
CNF	Constant Normal Force
CR	Cylinder Radius
CW	Cylinder Width
DR	Damper Radius
DW	Damper Width
DOF	Degree of Freedom
FF	Friction Force
HNF	High Normal Force
LNF	Low Normal Force

LIST OF ABBREVIATIONS (continued)

LTD	Large Tangential Displacement
MP	MATLAB Program
NA	Normal Approach
NF	Normal Force
SR	Sphere Radius
STD	Small Tangential Displacement
TA	Tangential Approach
TF	Tangential Force
UIC	University of Illinois at Chicago
UoM	Unit of Measurement

SUMMARY

This thesis deals with the problem of modeling dry friction contacts, that is a crucial aspect of the design of "dry friction dampers"; these devices are responsible for the absorption and dissipation of the energy of the turbomachinery blades vibrations.

A numerical method for the contact problem solution was developed and implemented in a MATLAB program. The tangential force-displacements curves were derived for the cylinder on a plane and for the two planes contacts using the proposed method. The corresponding tangential contact stiffness and the representation of the frictional hysteresis loops were computed. In particular, for the cylindrical contact, the influence of diameters and lengths were investigated, instead the behavior of these loops for non-uniform normal pressure distribution were also analyzed for the planar contact.

With the flexibility of the proposed method, it was possible to formulate two "numerical" equations for the normal and the tangential displacements of the cylindrical contact using multiple models with different dimensions. It is worth mentioning that no analytical solutions are available in the literature for the tangential displacement, so the solution presented in this thesis can be considered original.

CHAPTER 1

INTRODUCTION

1.1 Turbomachinery vibrations damping

Fatigue and large amplitude vibrations, due to working conditions close to resonance, are the major causes of failure in turbomachinery blades. Their design is particularly complex because they are thin and profoundly twisted and they have strict restrictions in terms of weight and dimensions. In order to guarantee and extend the predicted life of these components, special devices called "*friction dampers*" are adopted. They consist of a block of metal that is pressed by centrifugal force against the lower portion of the platforms of two adjacent blades. They can be of several shapes (Figure 1) but they exploit the same phenomenon: the vibrations enable the relative motion between the blade and the damper (Figure 2) and the friction at the contact determines the energy dissipation and the consequent smoothing of vibrations amplitude.

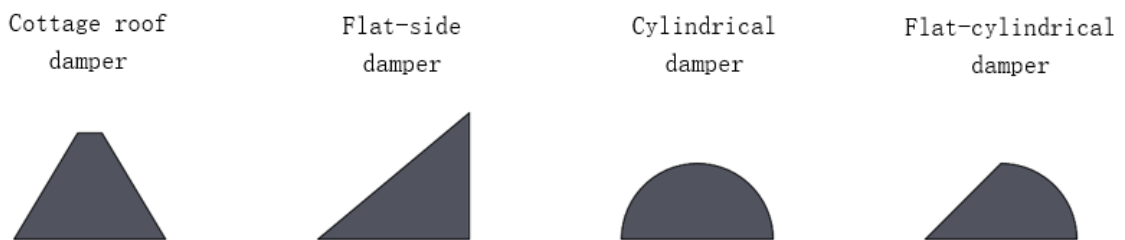


Figure 1: Dampers common shapes.

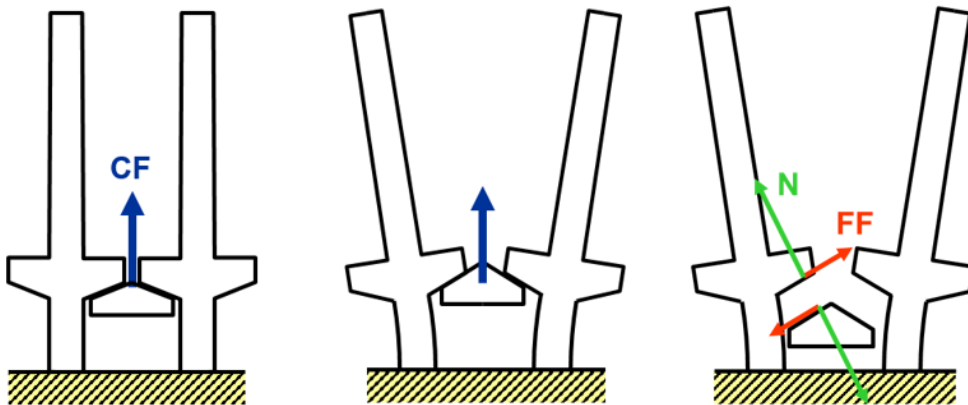


Figure 2: Dampers position and forces.

In order to optimize the design of these devices, maximizing the energy dispersion, it is essential to model the contact behavior and friction influence. Some researchers approached the problem using Harmonic Balance method [1; 2; 3; 4; 5], more recent studies adopted the Dynamic Lagrangian method [6; 7; 8], some others performed experimental simulations using a damper between two adjacent blades under controlled excitations [9; 10]. All the models take as input the friction coefficient of the two materials in contact μ and the normal and tangential contact stiffnesses, k_n and k_t . These parameters are so important that Ewins, at the end of his paper [11], said *"The two measured friction interface parameters μ and k_t are sufficient to model the friction interface with a high accuracy ... With these parameters, the simulation suite*

is able to accurately reproduce the dynamic behavior.” .

In this work of thesis a numerical model is implemented in a MATLAB program [12] to simulate the dry friction contact between bodies of any shape; the program is used to determine the normal and tangential contact stiffnesses and to plot the frictional hysteresis loop of those bodies.

1.2 Thesis methodologies and objectives

In Appendix A, the numerical method used to solve the contact problem is described in detail. It is based on the assumption that the normal and the tangential problems can be decoupled: the effectiveness of this approximation is confirmed in Appendix B, where the results of the MATLAB program for sphere on plane contact problem are validated using the analytical solutions that Hertz proposed [13]. The program takes as input the normal displacement of a surface that is distant from the contact area even if the force applied to the same surface could be used; the first approach was preferred because it is the same adopted to derive the analytical equations. Where the force value is required as input, an iterative algorithm is utilized to determine the correct displacement that generates that force.

Considering the different shapes of the friction dampers (Figure 1), two types of contact are possible between the damper and the blades, cylindrical and planar. One of the two main objectives of this thesis is to define which are the factors that influence the normal and tangential stiffnesses in this type of contacts and to integrate the analytical solutions with numerical equations where it is necessary. The other objective is to derive the frictional hysteresis loops

from the tangential force-displacement curves and to analyze how they are affected by various loading conditions.

1.3 Analytical solutions

For the validation process of the program, in the normal problem, the Hertz theory is considered for the sphere on sphere contact, instead for the tangential problem, Mindlin results are used as reference [14; 15; 16]. Both of them propose an equation that relates force and displacements.

For what concerns the cylindrical contact, Hertz derived a solution to compute normal contact pressure but he did not provide one for the normal approach; consequently, there are several formulations, some empirical [17; 18], some others analytical [19; 20; 21], and this creates an opportunity for further analyses using the MATLAB program. Johnson in his book [22] re-elaborated Mindlin theory to adapt it to the cylindrical tangential problem but also in this case there is not an expression for the tangential approach.

There are no analytical models to describe the behavior of the plane on plane contact therefore the finite element discretization and numerical method are the only viable solutions.

1.4 Thesis overview

This paragraph is intended to guide the reader through the thesis.

In Appendix A, the numerical method that is implemented in the MATLAB program is explained with graphs, equations and further details regarding the approximations.

In Appendix B, the sphere on sphere contact problem is solved with numerical and analytical approaches; the results are initially compared in two specific loading conditions to have a clear

view of stresses and displacements distributions and then in a wide load range to confirm the program can work without restrictions. The same structure is adopted for normal and tangential problem.

The analysis of the cylindrical contact problem is presented in Chapter 2. In the normal problem section, a numerical formulation for the normal approach is derived thanks to the interpretation of the results concerning the influence of the compression, the diameter and the length of the cylinder. In the tangential problem section, the same analysis is performed for the tangential approach with the help of several tangential force-displacement trends; these curves are used to plot different hysteresis loops and to make considerations regarding their area.

Chapter 3 deals with plane on plane contact and the focus here is on the influence that non uniform normal pressure distributions can have on the frictional hysteresis loop. In particular, this section is divided in two parts: in the first part the entire potential contact area is involved in the contact, in the second part the normal pressure acts on an increasingly narrow portion of the potential contact surface.

CHAPTER 2

CYLINDER IN CONTACT WITH A PLANE

In this chapter, the focus is on the contact between a cylinder and a plane. This is one of the two types of contact that is possible to find in the dampers studied to mitigate turbomachinery vibrations. The problem is much more complicated than that of the sphere because the cylinder is not an axisymmetric solid and the analytical solutions that are available treat the problem as if it was 2D [22] [13]. As previously stated, the MATLAB program that was developed (see Appendix B) is capable to compute the normal and tangential displacements and force distribution for bodies of any shape in contact, but even more important, it can calculate this values for several loading conditions; therefore, it is possible to have the correlation between tangential force and tangential displacements that no analytical solution can predict.

In section 2.2.2, the results of several models are presented and compared and they are used to formulate an equation that links normal force and normal displacements; it is validated using the equations proposed in the literature.

In section 2.2.5, a study is conducted to identify which is the influence of the bodies compression on the total deformation in the contact.

2.1 Bodies design and mesh generation

In order to simulate the contact, two bodies are modeled, half of a cylinder and a plane. ANSYS apdl modeling environment is used to build the bodies and to approximate them with

finite elements [23]. The 'hard points projection techniques' (see Appendix B.1.2) is preferred and the parameters used are:

- $CR = 5,000 \mu\text{m}$
- $CAL = 1,200 \mu\text{m}$
- $CW = 1,200 \mu\text{m}$

The potential contact area is dimensioned considering the area involved in the contact when an applied force produce a maximum pressure value of 2500 MPa: this pressure peak will never be reached so the maximum CA extension will not exceed the potential value. But this value is further increased because it is interesting to investigate how the cylinder is deformed far from the actual contact area; the surface where contact is more likely to occur has a denser mesh. Figure 3 and Figure 4 show the two bodies and a detail of the contact area.

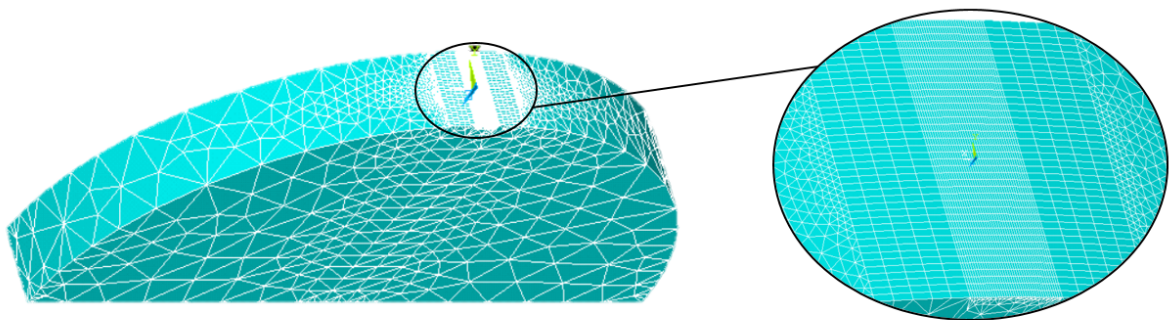


Figure 3: Half cylinder model: cylinder-plane contact.

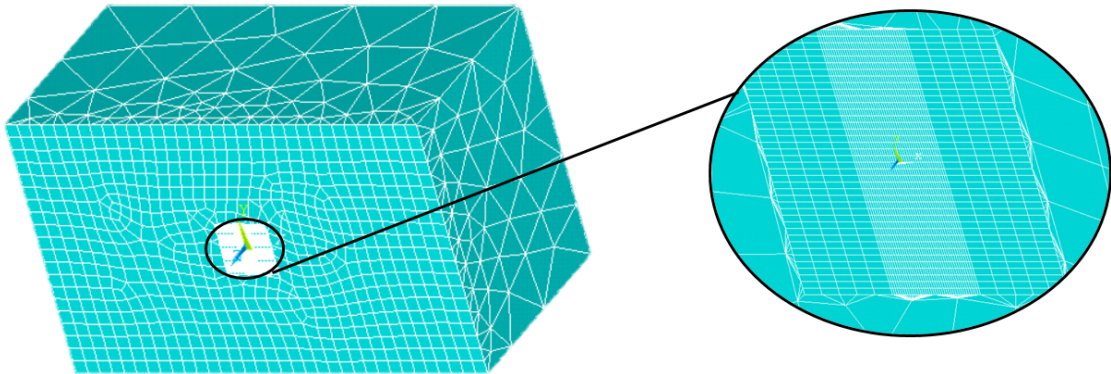


Figure 4: Plane model: cylinder-plane contact.

2.2 Normal contact problem: analytical vs numerical solutions

In his work [13], Hertz formulated a theory also for cylinder-cylinder contact, so his results can be compared with that of the MATLAB program. However, the theory does not take into account the stress concentration along the borders due to the edge effect because it was developed considering a slice of the sphere in plane strain conditions.

For what concerns the vertical displacement, several solutions have been attempted to date: some researchers proposed empirical formulations obtained with experiments [17; 18], some tried to extend Hertz results for sphere-sphere contact considering the cylinder as a sphere with infinite radius [20; 19; 21], some others developed their own model [22].

2.2.1 Hertz contact model

The hypothesis of the solution are the same of Appendix B.2.1.

Contact Area Semi-width

$$b = \sqrt{\frac{4 F}{\pi L} \frac{1}{2(\alpha_x + \beta_x)} \left(\frac{1 - \nu_1^2}{E_1} + \frac{1 - \nu_2^2}{E_2} \right)} \quad (2.1)$$

where

- b is the contact area semi-width
- F is the force that compress the bodies one against the other
- L is the width of the cylinder
- E_1 and E_2 are the elasticities of the two bodies
- ν_1 and ν_2 are the Poisson's coefficients of the two bodies
- $\alpha_x = \frac{1}{2R_1}$ $\beta_x = \frac{1}{2R_2}$ represents the curvatures of the two cylinders in x-z plane (R_1 and R_2 are spheres radii)

The total value of the contact area is $CA = 2bL$.

Pressure distribution

$$p = \frac{2F}{\pi L b} \sqrt{1 - \left(\frac{Y}{b}\right)^2} \quad (2.2)$$

2.2.2 Normal approach

2.2.2.1 Norden - 1973

Norden developed two solutions for normal approach. They are based on the assumption that the cylinder can be considered as a sphere with infinite radius.

Solution 1

$$\delta = \frac{F}{L}(\lambda_1 + \lambda_2) \left[1 + \ln \frac{L^3}{(\lambda_1 + \lambda_2)FR} \right] \quad (2.3)$$

where

- δ is the normal approach
- F is the force that compress the bodies one against the other in N
- L is the width of the cylinder in mm
- $\lambda_i = \frac{1-\nu_i^2}{E_i}$

Solution 2

$$\delta = \frac{F}{L}(\lambda_1 + \lambda_2) \left[-0.608205 + 1.5 \ln \frac{L^3}{(\lambda_1 + \lambda_2)FR} \right] \quad (2.4)$$

2.2.2.2 Harris - 1991

Harris cites Palmgren in [18]: the formulation is valid for steel on steel contact.

$$\delta = \frac{3.84}{10^5} \left(\frac{F^{0.9}}{L^{0.8}} \right) \quad (mm) \quad (2.5)$$

2.2.2.3 Brandlein - 1999

$$\delta = \frac{4.05}{10^5} \left(\frac{F^{0.925}}{L^{0.85}} \right) \quad (mm) \quad (2.6)$$

2.2.2.4 Roark's Formulas - 2002

The hypothesis here is the diameter of the cylinder is small if compared to the length.

$$\delta = \frac{2p(1-\nu^2)}{\pi E} \left(\frac{1}{3} + \ln \frac{2D}{b} \right) \quad (2.7)$$

where

- $p=F/L$
- $b = 1.6\sqrt{pk_d C_E}$
- $C_E = \frac{1-\nu_1^2}{E_1} + \frac{1-\nu_2^2}{E_2}$
- $K_d = D$ is the cylinder diameter

2.2.2.5 Johnson - 2003

$$\delta = \frac{F}{L} \frac{(1-\nu^2)}{\pi E} \left\{ 2 \ln \frac{4R}{a_1} - 1 \right\} \quad (2.8)$$

where

- $a_1 = \sqrt{\frac{4FR}{L\pi E}}$
- R is the cylinder radius

2.2.2.6 Kosarev - 2011

Kosarev cites Dinnik [24] for his formulation.

$$\delta = \frac{F}{L} \lambda \left\{ 0.407 + \ln \frac{2R}{b} + \ln 4 \left(\frac{z}{b} \right)^2 \right\} \quad (2.9)$$

where

- $\frac{z}{b} = 7.5$ (empirical)
- $b = \sqrt{\frac{4FR\lambda}{L}}$
- $\lambda = \frac{2(1-\nu^2)}{\pi E}$

2.2.3 Specific case: normal force=350 N

To begin with, the solutions obtained with the numerical program are compared with that of analytical formulations in a specific case. The target normal force NF=350 N is selected in order to have a maximum pressure lower than 2000 MPa in the contact area for the same reason of B.2.2. It is important to remember that the term 'target' is used because the MP takes the displacements as input; in this case an iterative algorithm is performed to select the appropriate displacements to get the target force.

Contact area

In Figure 5, the yellow shading represents the contact area calculated with Hertz equation, the red squares are the nodes inside contact area and the blue asterisks those outside. The numerical area is enlarged at the two extremes, for $y = \pm 600 \mu m$, so the program is correctly simulating the real behavior of the cylinder compressed that tends to squeeze at the edges.

The Hertz CA semi-width is slightly higher than the numerical solution. It is important to remember that Hertz developed his solution for 2D body using the plane strain approximation, instead the software works directly with 3D and consequently is more precise.

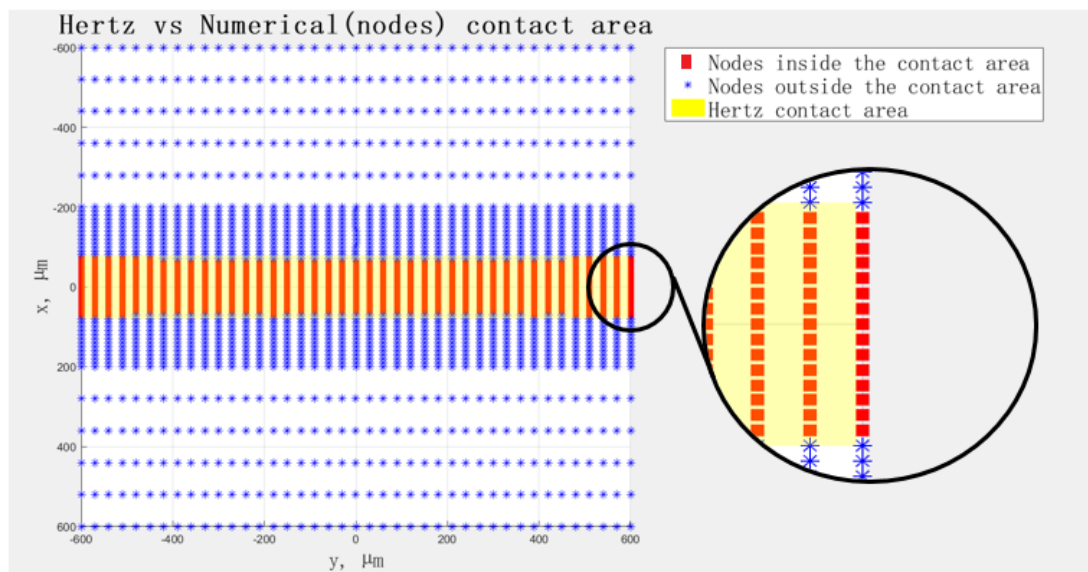


Figure 5: Contact area comparison: cylinder.

Normal pressure distribution

In Figure 6 and Figure 7, the Hertz and the numerical pressure distributions are presented and in Figure 8 and Figure 9 they are compared in 3D and in 2D. In cylinder case there is not the perfect coincidence that there is in sphere case but it is due to the edge effect and the misalignment in CA dimensions.

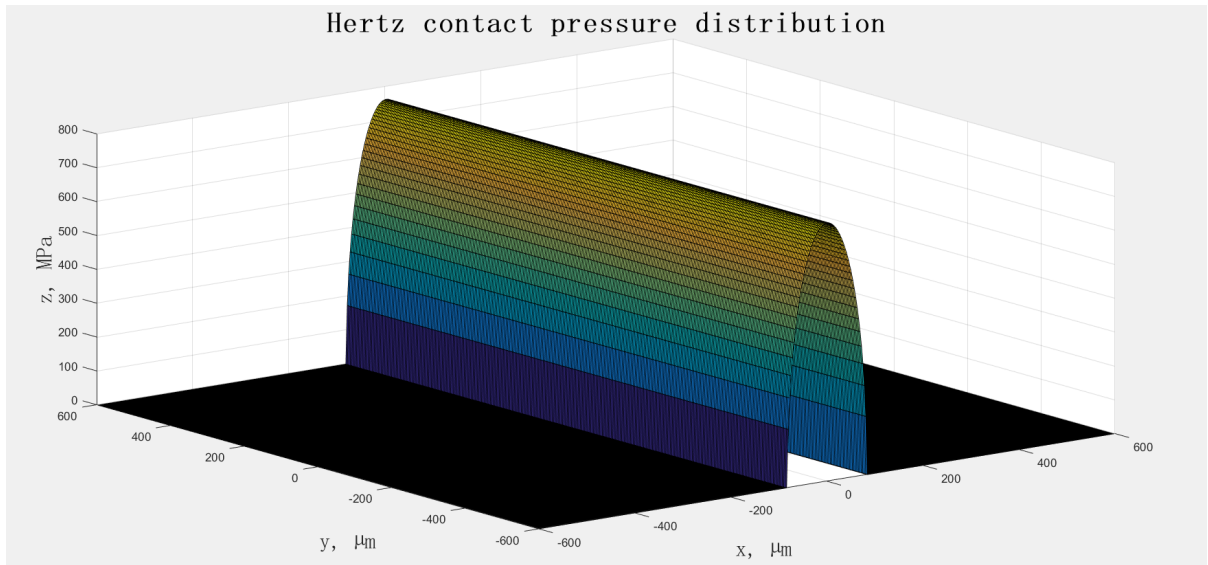


Figure 6: Hertz pressure distribution: cylinder.

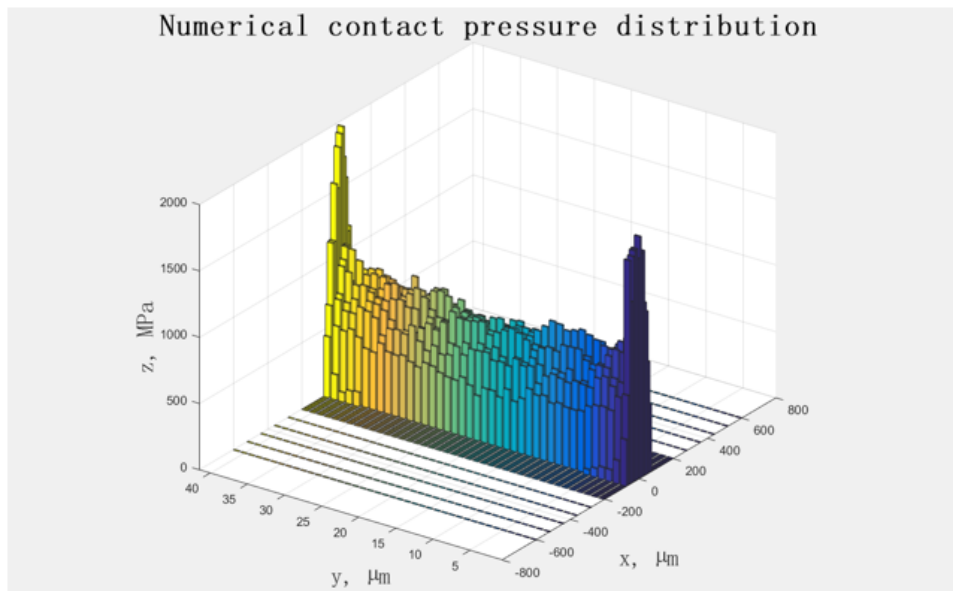


Figure 7: Numerical pressure distribution: cylinder.

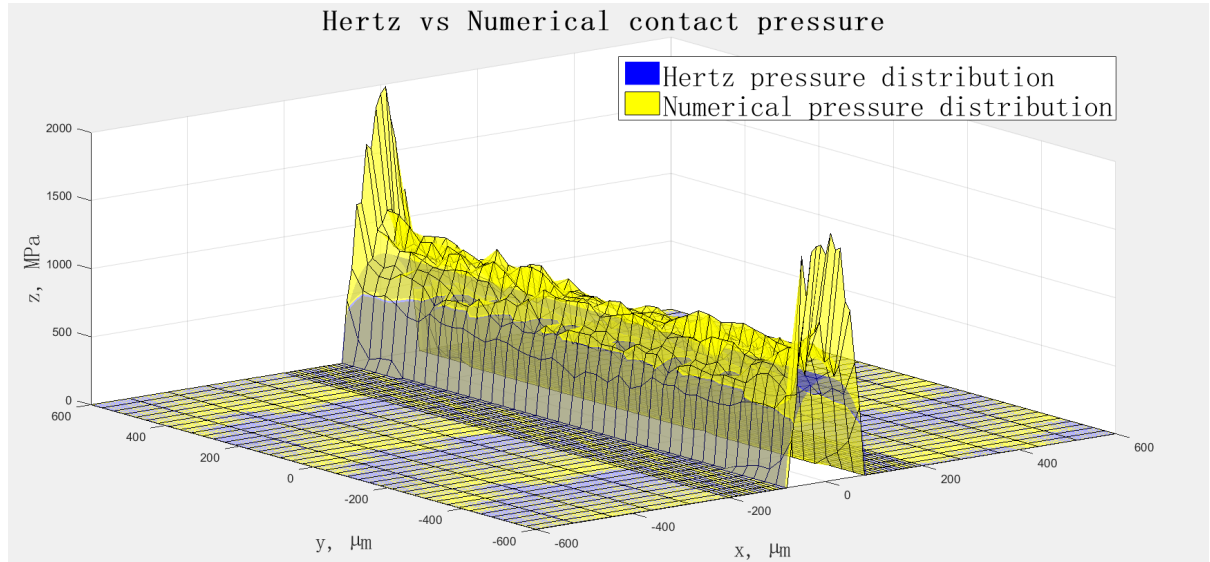


Figure 8: Pressure distribution comparison 3D: cylinder.

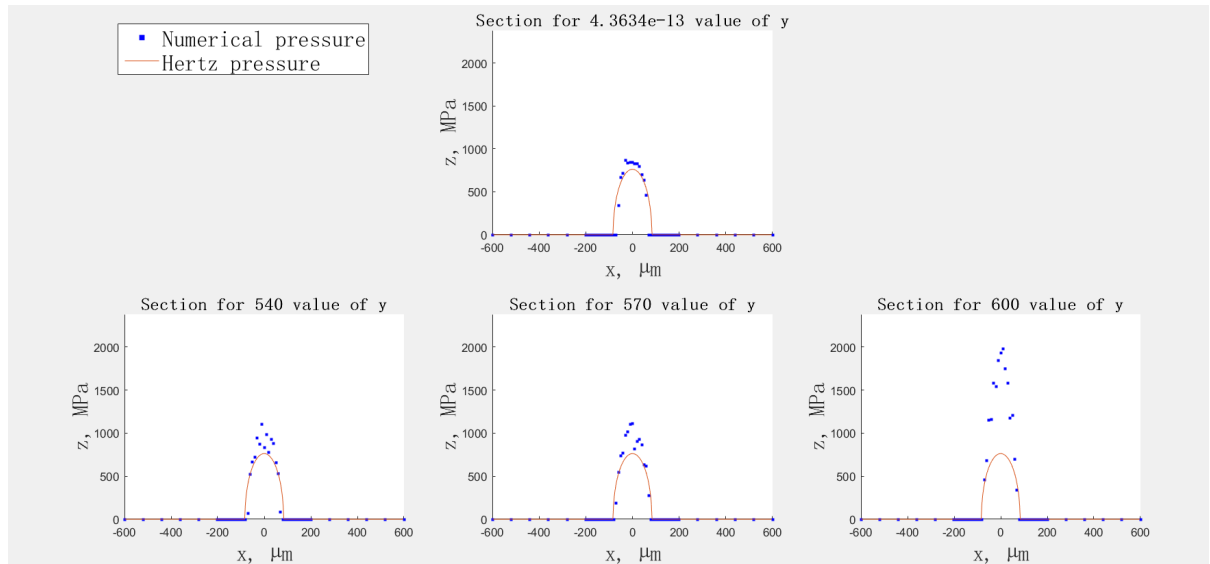


Figure 9: Pressure distribution comparison 2D: cylinder.

In the lower part of Figure 9 the edge effect is evidenced: the maximum pressure is more than three times the maximum pressure in the center of the cylinder.

2.2.4 System behavior for several loading conditions

Normal force vs dz

In Figure 10, the solution for vertical approach obtained with numerical method is compared with all the analytical solution that are mentioned before (2.2.2). Some of them do not refer exactly to the case 'cylinder on a surface' and consequently have been adapted. It is important to evidence that the numerical solution is located in the middle of the other curves.

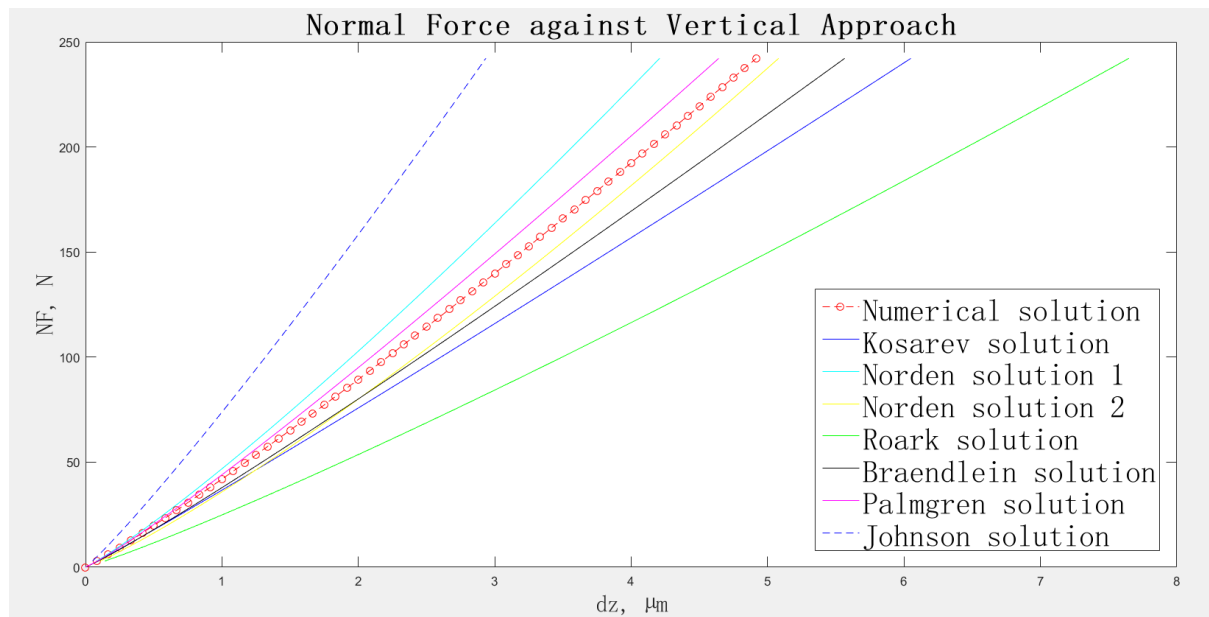


Figure 10: Normal force vs dz: cylinder.

The solution that Johnson proposed seems to be the most rigid, but it takes into account only the compression of the cylinder body and not specifically the contribution of the contact. Roark's formulas refer to a very specific case, "*Cylinder of length L large as compared with D ...*" [21], and this graph is the proof they can not be generalized: the behavior of models with different shape will be analyzed later on, in order to check if they work in alternative conditions.

Contact area vs normal force

Figure 11 confirms the results of 'specific case' section: the CA calculated with Hertz equation is higher than that obtained with numerical approach.

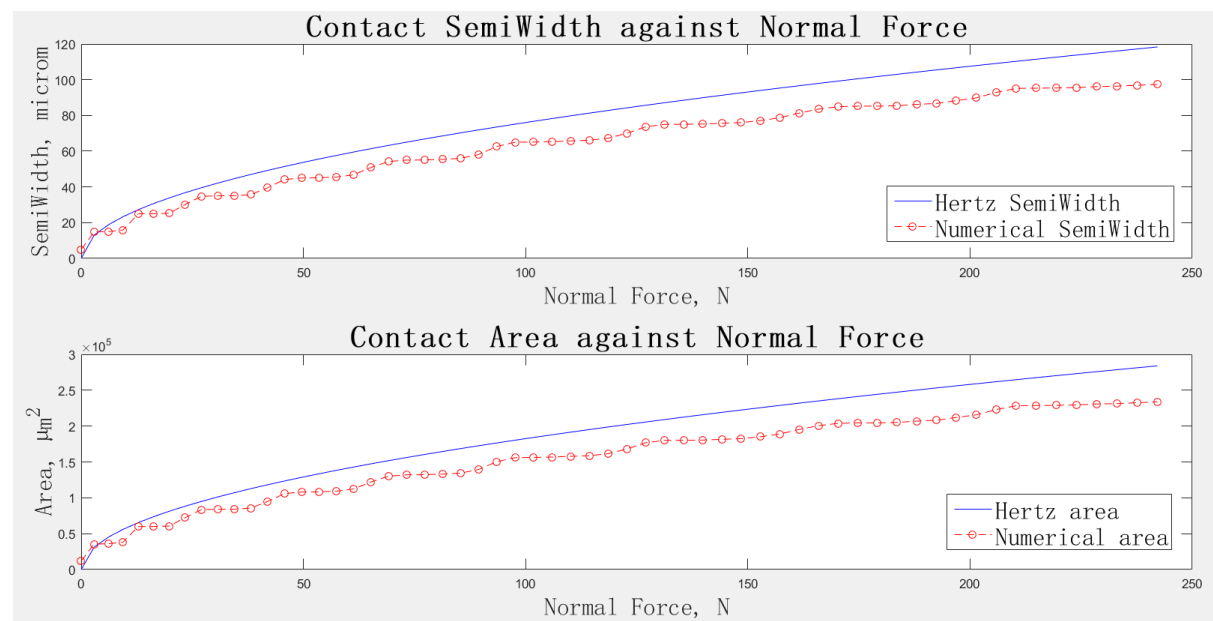


Figure 11: Contact area vs NF: cylinder.

Mean pressure vs normal force

The information on maximum pressure over the entire CA is not relevant because of edge effect. For what concerns mean pressure, the trend of the whole cylinder is still affected by the peaks at the borders (lower graph of Figure 12), instead the curves that refer to the central section are coincident (higher graph of Figure 12).

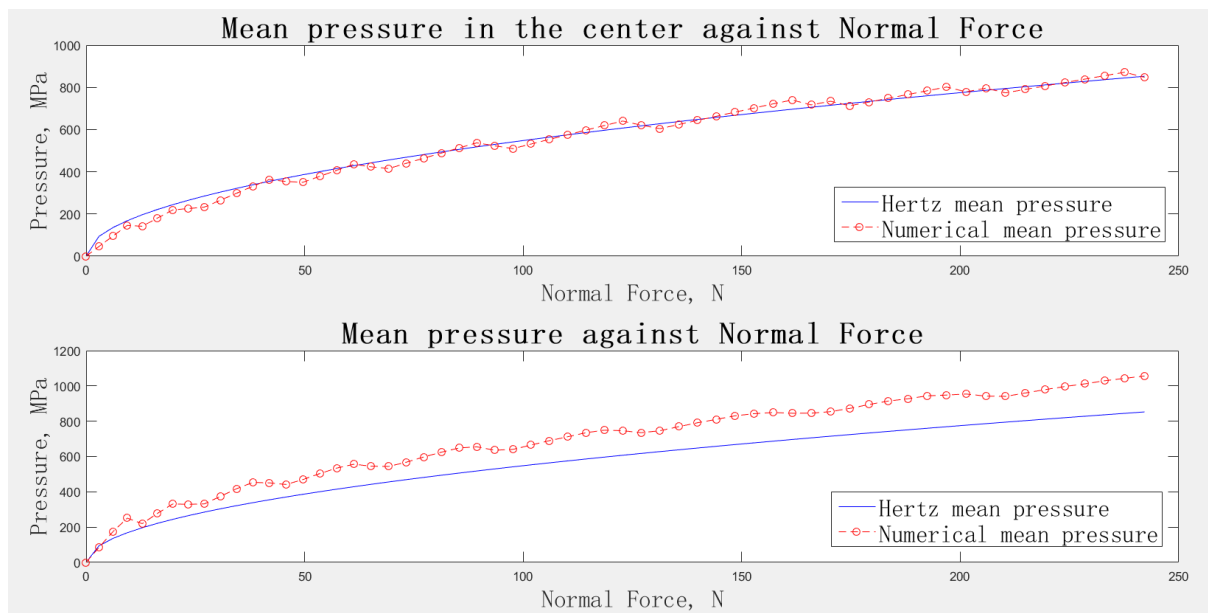


Figure 12: Mean pressure vs NF: cylinder.

2.2.5 Cylinder compression influence in normal approach

In his work [20], Norden underlined the necessity to make a distinction between the contribution of the contact compression and that of cylinder compression, in the calculation of the normal approach of a cylinder pressed against a surface. The multiple equations that are available and the anomalous trend of Johnson's solution in Figure 10 confirm the problems needs a deeper analysis.

The MATLAB program allows the computation of the displacement of each node of the contact area: with simple geometrical considerations it is possible to calculate the compression too.

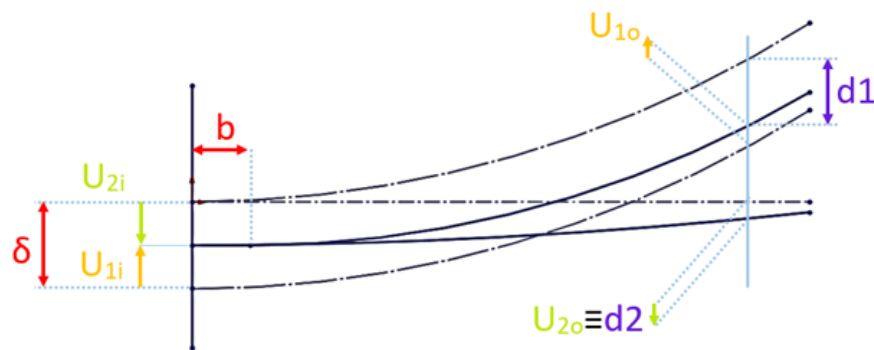


Figure 13: Bodies deformation.

In Figure 13, d_1 and d_2 represent the displacements that can be computed with the program in each node, δ the normal approach, u_{1i} and u_{2i} the compression of the two bodies inside the

contact, u_{1o} and u_{2o} the compression outside the contact. It is evident that $u_{1o} = \delta - d_1$ and $u_{2o} = d_2$. A representation of d_1 and d_2 is available in Figure 15 and Figure 16.

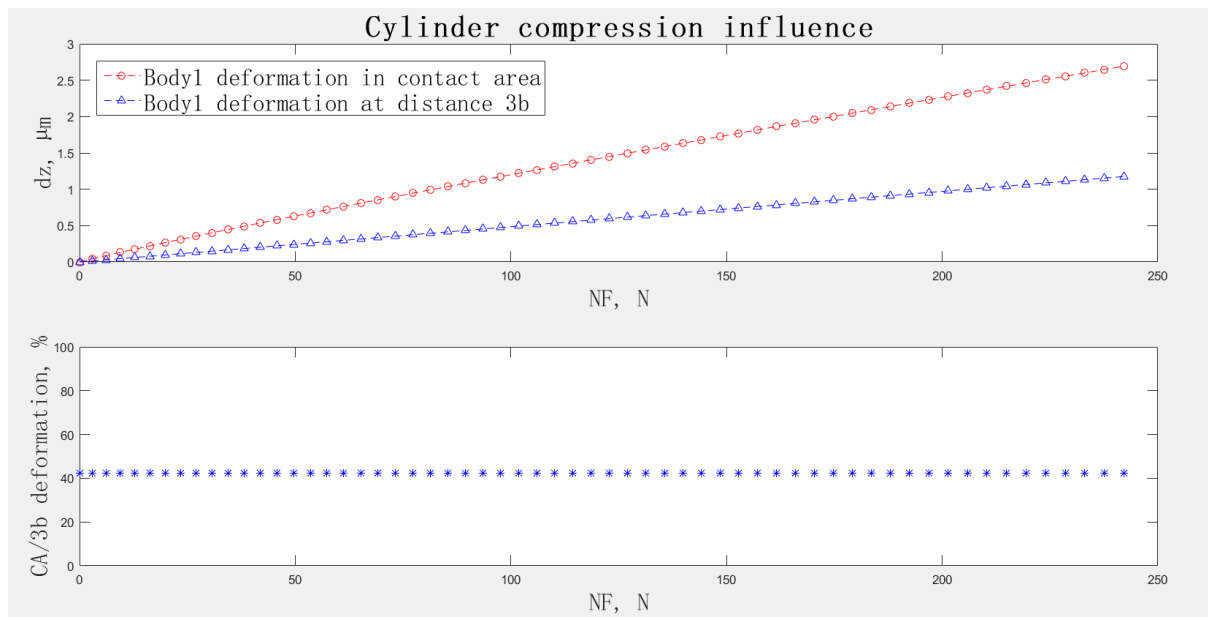


Figure 14: Cylinder compression influence in normal approach.

In order to see if the cylinder compression has an influence on the total approach, u_{1i} , that has both cylinder and contact compression components, is compared with u_{1o} , that is caused solely by the cylinder compression; u_{1o} is measured at a distance '3b' from the contact center.

Figure 14 has two very interesting information regarding the total deformation at the contact interface: first of all, the cylinder body compression has a remarkable influence, because in

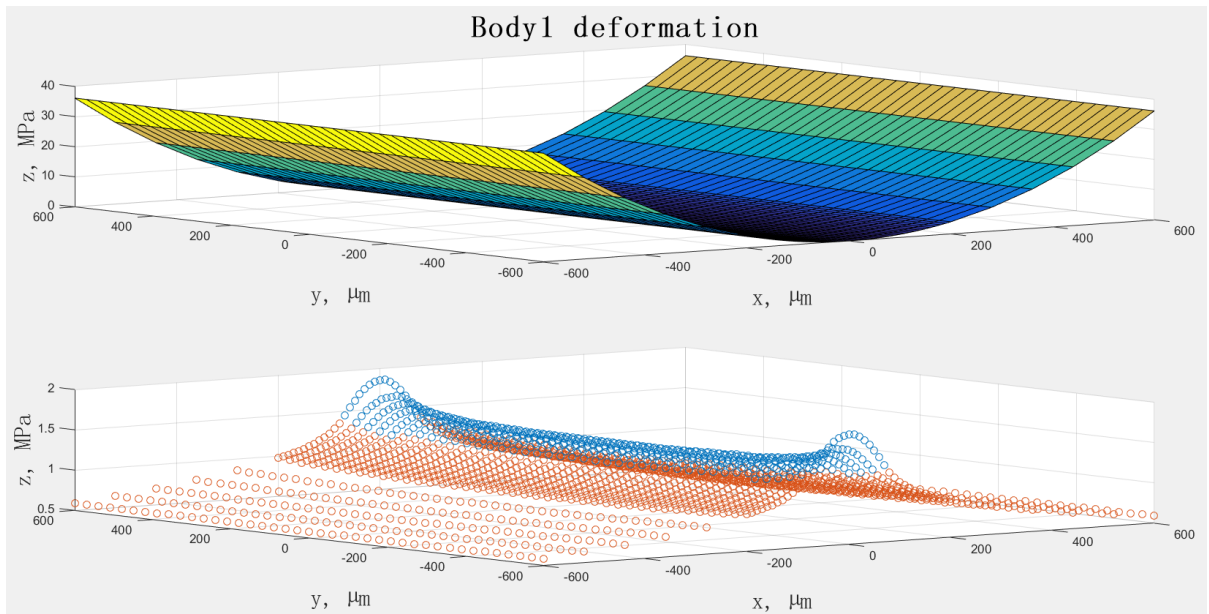


Figure 15: Cylinder: body1 displacements.

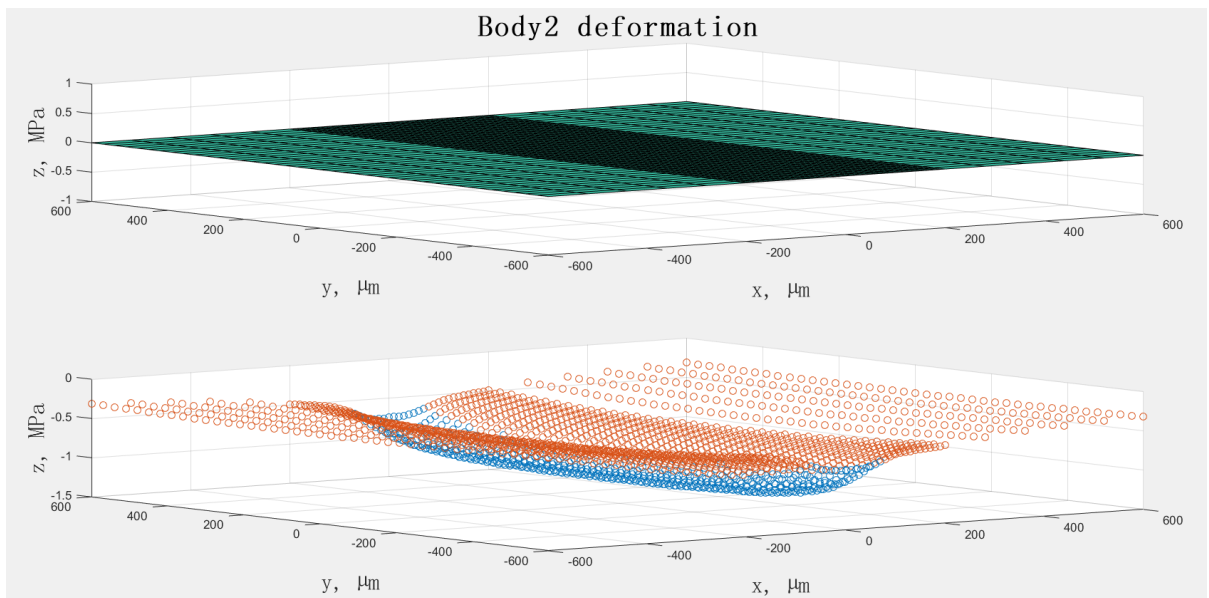


Figure 16: Cylinder: body2 displacements.

this case it represents more than 40% of the total displacement; secondly, the percentage does not depend on the load (NF), so the body and the contact compression contributions have the same dependence on the load, that is the same result Kosarev, Roark and Norden obtained in their equations.

In Hertz theory the contribution of the sphere compression is not even mentioned (see Appendix B.2.1), so it is interesting to understand if it was neglected. The same analysis of cylinder case is performed for the 'sphere on a plane' contact, with a sphere with the same diameter, in order to have a term of comparison (Figure 17). The sphere compression accounts for less than 8% that is why in Hertz theory this contribution is not taken into account.

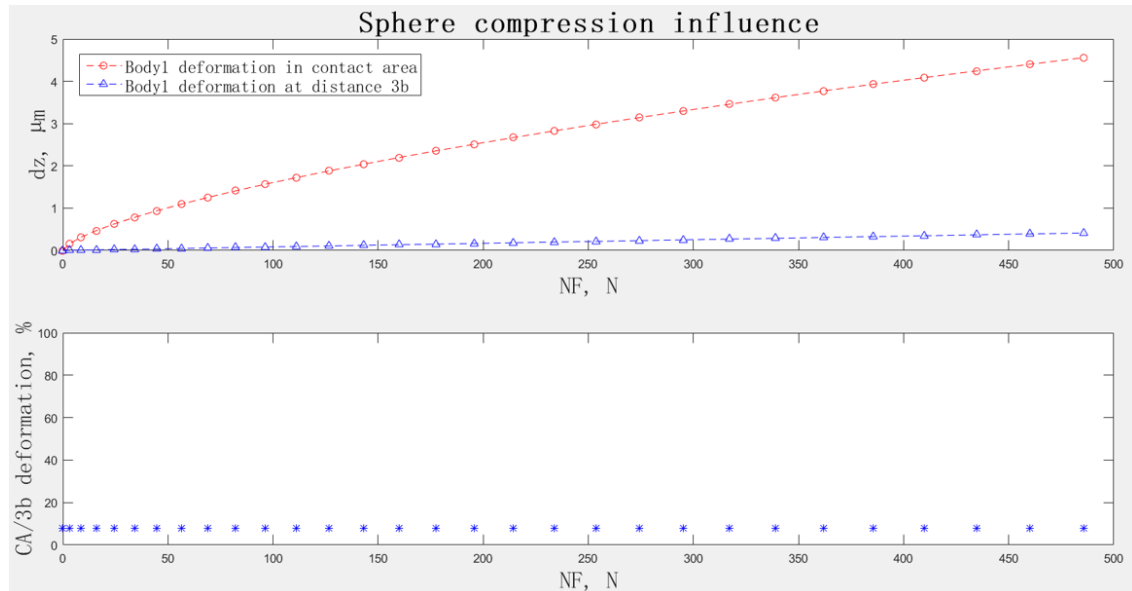


Figure 17: Sphere compression influence in normal approach.

TABLE I: CYLINDER COMPRESSION INFLUENCE IN NORMAL APPROACH: DIAMETERS AND LENGTHS

Model identifier	Diameter 'D'	Length 'L'
Cylinder 1	5000 μm	1200 μm
Cylinder 2	2500 μm	1200 μm
Cylinder 3	5000 μm	2400 μm
Cylinder 4	2500 μm	2400 μm

2.2.5.1 Diameter and length effect in cylinder compression

The versatility of the MATLAB program allows the analysis and comparison of several models; in particular, in this section, it is investigated how the diameter and the length of the cylinder can affect the compression influence in normal approach. For this purpose four different models were created and their characteristics are summarized in Table I.

Cylinder length effect

In Figure 18, it is possible to see what happens to the body compression influence when the length of the cylinder is doubled and the diameter is kept constant: the influence percentage is almost unchanged. To confirm this result, the same analysis is performed when the diameter is halved, Figure 19; the influence percentage is reduced but it is around 25% for both 'Cylinder 2' and 'Cylinder 3'. So the cylinder length does not affect the body compression influence.

Cylinder diameter effect

On the contrary, in Figure 20 it is illustrated how the body compression changes when the cylinder length is kept constant and the diameter is halved. The physics of the system is preserved because reducing cylinder diameter its stiffness increases, so the body compression is

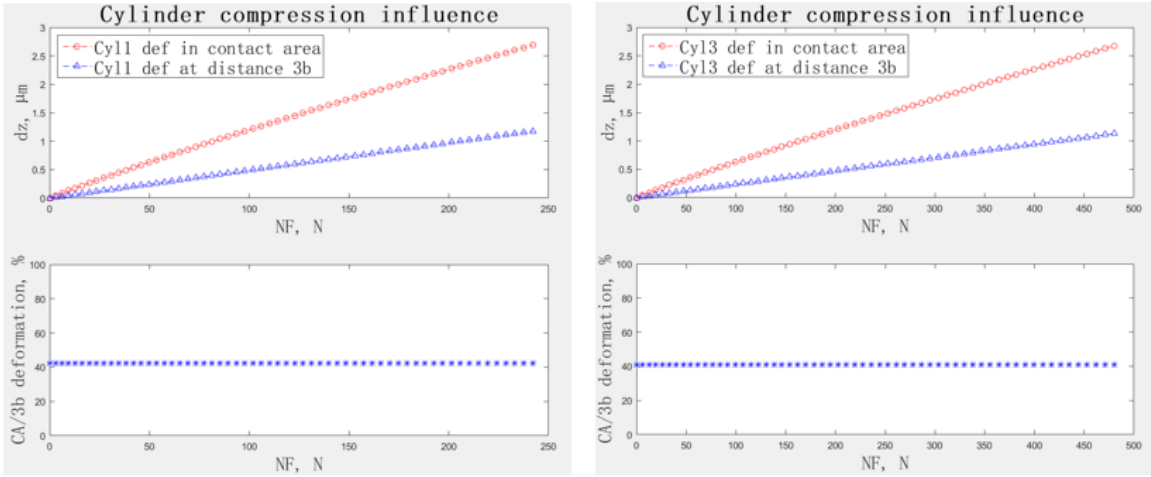


Figure 18: Cylinder compression influence in normal approach: length effect 1.

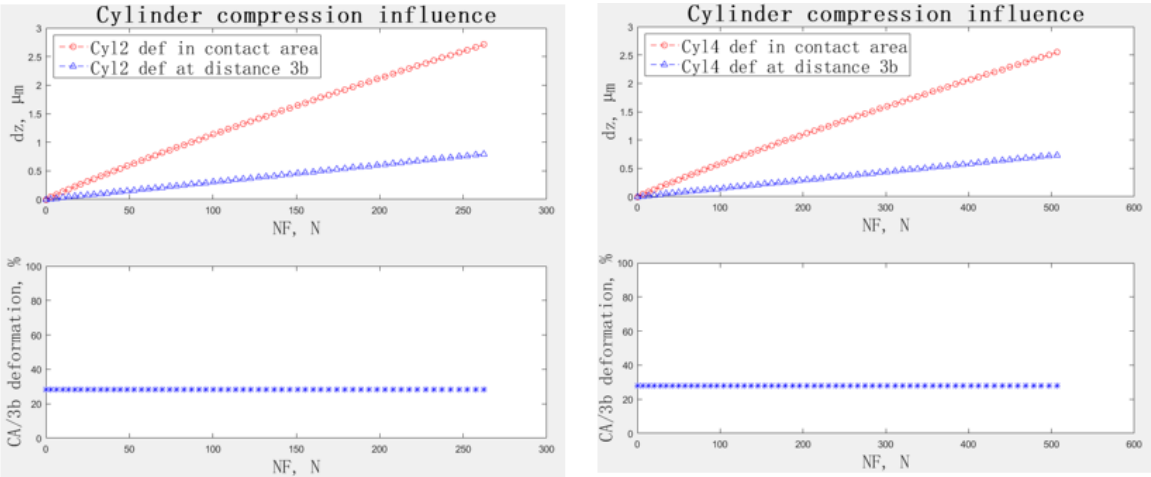


Figure 19: Cylinder compression influence in normal approach: length effect 2.

reduced. Then, it is possible to conclude that the cylinder diameter strongly affects the cylinder compression influence in normal approach.

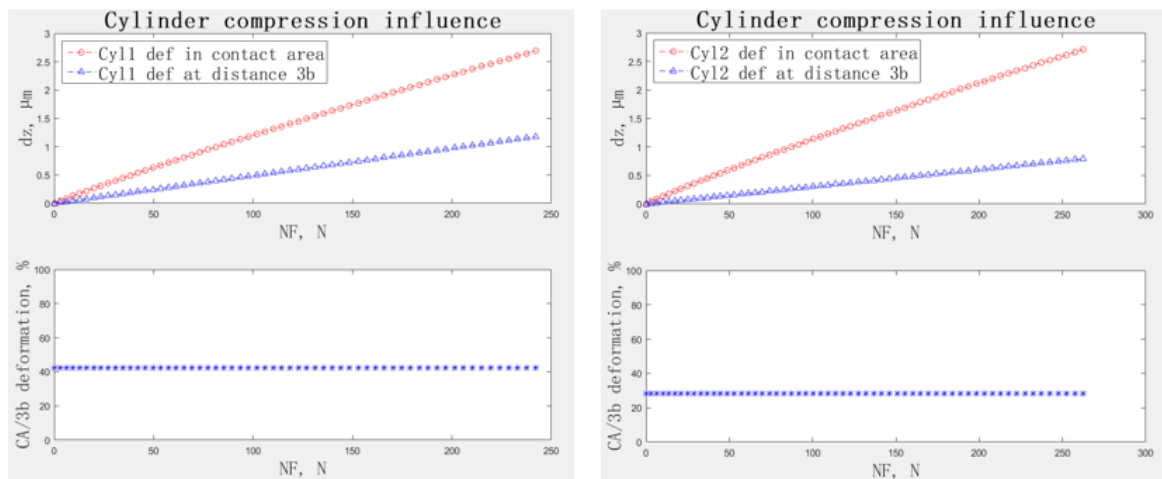


Figure 20: Sphere compression influence in normal approach: diameter effect.

2.2.6 Diameter and length influence in normal approach

The equations Brandlein and Palmgren proposed for the normal approach do not have any dependence on the cylinder diameter, instead in Kosarev, Roark and Norden solutions the cylinder diameter is taken into account but they show a linear proportionality with the ratio F/L , Force over Length. Thanks to the software adaptability it is possible to calculate and analyze what happens for several cylinder configurations and using mathematical instruments, a realistic law to link normal displacements and forces can be deduced. In Table II, the dif-

TABLE II: DIAMETER AND LENGTH INFLUENCE IN NORMAL APPROACH

Model identifier	Diameter 'D'	Length 'L'	Symbol
Cylinder 1	5000 μm	1200 μm	Δ
Cylinder 2	2500 μm	1200 μm	o
Cylinder 3	5000 μm	2400 μm	Δ
Cylinder 4	2500 μm	2400 μm	o
Cylinder 5	5000 μm	4800 μm	Δ
Cylinder 6	5000 μm	9600 μm	Δ
Cylinder 7	10000 μm	9600 μm	*
Cylinder 8	10000 μm	19200 μm	*

ferent characteristics of the models used in this study are summarized; in the last column it is illustrated the symbol used in the graphs for each model: it is equal for cylinders with the same diameters.

General comparison

Observing Figure 21, it is possible to note that the curves with the same cylinder length tend to cluster. Then, it is interesting to see what happens to the curves if they are plotted considering F/L instead of F in the abscissa: Figure 22; the curves are much closer to each other but not perfectly coincident, so the normal approach is not linearly proportional to the ratio F/L as expected from Brandlein and Palmgren solutions.

Cylinders with equal diameters comparison

Not even the curves that refer to cylinders with equal diameters are grouped (see Figure 23), indicating the diameter contribution must be considered and confirming what is stated in 2.2.5.

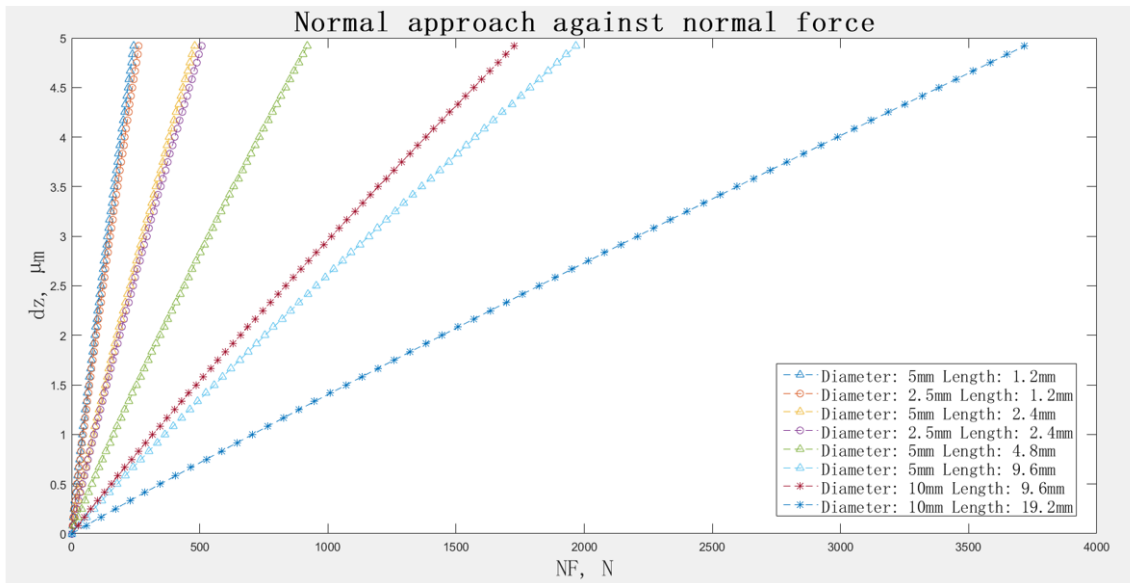
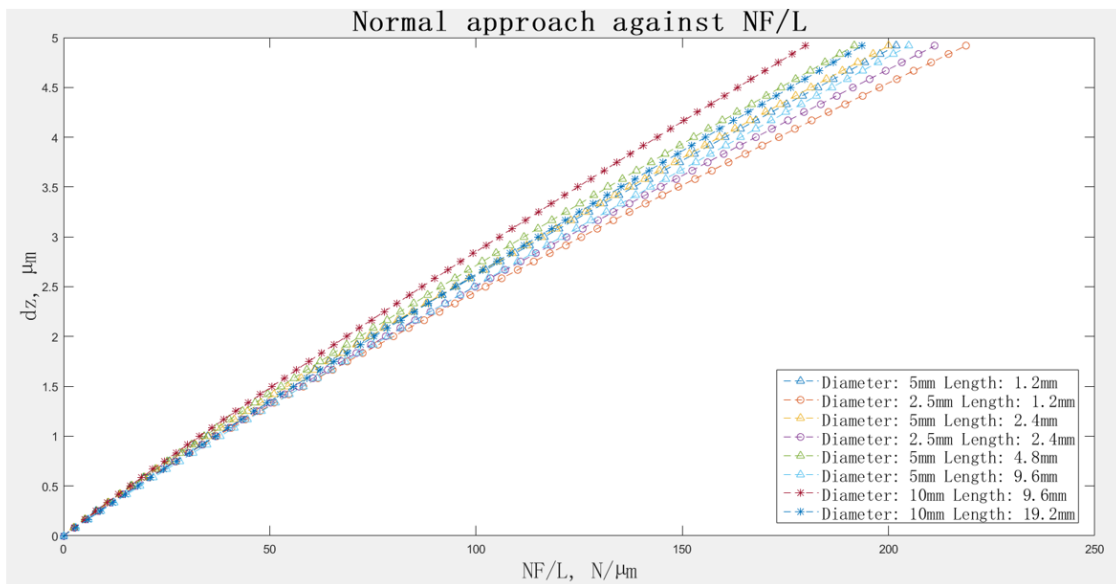


Figure 21: Dz vs normal force: cylinders comparison.

Figure 22: Dz vs NF/L : cylinders comparison.

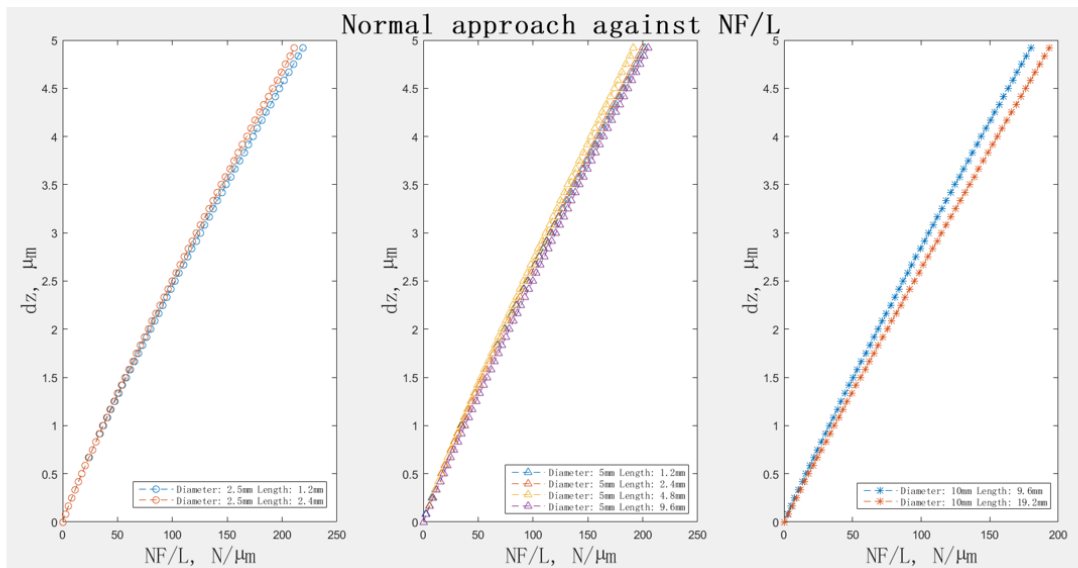


Figure 23: Dz vs NF/L: cylinders with equal diameter.

Normal approach: numerical and analytical solutions comparison

Since the models of Table II are available, it is interesting to compare the analytical and the numerical solutions in two extreme cases: the first is 'Cylinder 1', that is used also in 2.2.4 and that has the diameter much bigger than the length; the second is 'Cylinder 2' whose length is twice the diameter.

First of all, it is possible to see how the numerical solution is approaching Johnson's solution in 'Cylinder 8' case. It is consistent with everything that has been said so far because Johnson considers only the body compression contribution to the total displacement instead the numerical solution takes into account both contact and cylinder compression contributions and the latter is higher as the diameter increases (see 2.2.5).

Secondly, Roark's solution is closer to the other analytical solutions because his hypothesis of cylinder length much bigger than diameter is better satisfied even if not completely respected.

Finally, Brandlein and Palmgren curves are in both cases the closest to the numerical solution, so in the next section the same equation structure is used to find the relationship between normal displacements and forces.

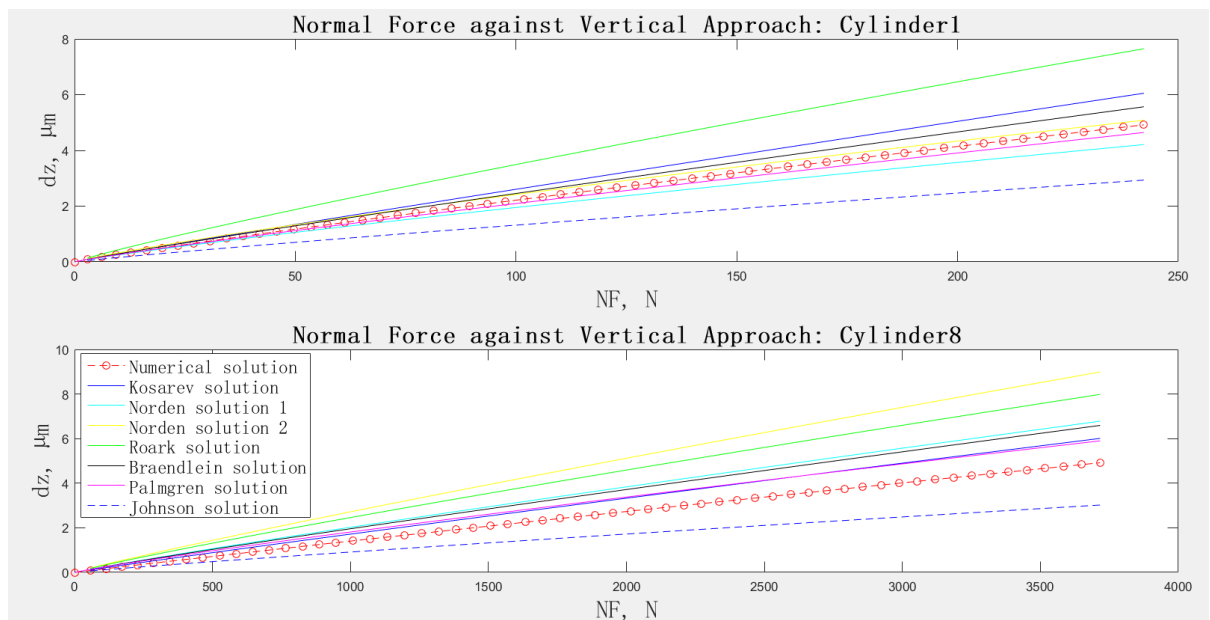


Figure 24: Normal force vs dz: cylinders 1 and 8 comparison.

2.2.6.1 Normal approach: numerical formulation

The data gathered with the simulations of all the models of Table II and the MATLAB function *'lsqcurvefit'* allow the formulation of a numerical expression for normal approach. As it is explained in the MATLAB Optimization Toolbox User's Guide, the function solves "*nonlinear curve-fitting problems in least-squares sense*" using the following formulation [25]:

$$\min_x \|F(x, xdata) - ydata\|_2^2 = \min_x \sum_i (F(x, xdata_i) - ydata_i)^2 \quad (2.10)$$

where

- xdata are the input values of the variables of the function F
- ydata are the values the function F assumes in xdata
- x are the coefficients of the variables of the function F that are sought

The function uses Trust-Region-Reflective algorithm [26].

The output of this analysis is summarized in the normal approach expression:

$$\delta = 10.21 \left(\frac{F^{0.917}}{L^{0.928}} \right) D^{0.099} \quad \text{with } [D] = [L] = \mu m \text{ and } [F] = N \quad (2.11)$$

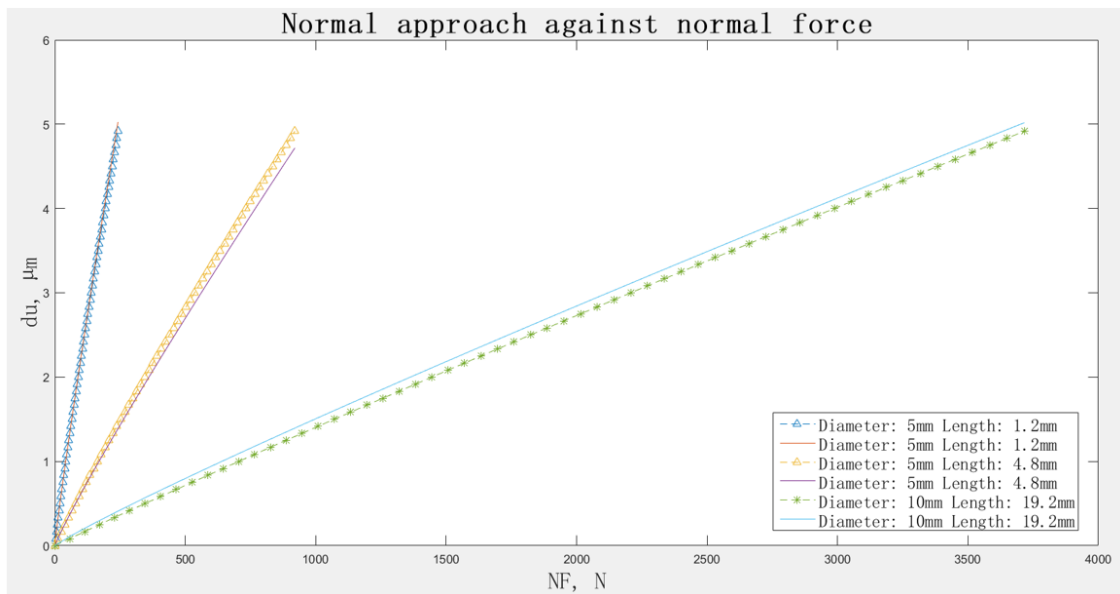
In Table III the exponents of F, L and D of Brendlein, Palmgren and numerical solutions are compared: in numerical formulation the diameter is taken into account and the length has an exponent slightly higher and very close to the one of the force.

In conclusion, in Figure 25 the normal approach numerical formulation is plotted in parallel

TABLE III: NORMAL APPROACH: EXPONENTS COMPARISON

Exponents	Brendlein	Palmgren	Numerical
F	0.925	0.900	0.917
L	0.850	0.800	0.928
D	0.000	0.000	0.099

with actual numerical results in three explicative cases, in order to visualize the output of curve-fitting process that is satisfactory.

Figure 25: dz vs normal force: numerical equation and results.

2.3 Tangential contact problem: analytical vs numerical solutions

The analytical solution to the tangential contact problem that Mindlin proposed for the 'sphere on sphere contact' is re-adapted by Johnson for the 'cylinder on a surface' case [22]. The equations that are taken into account concern elastic bodies in incipient sliding and they are based on the same hypothesis set by Mindlin. This allows the comparison of the results of numerical solution with that of analytical solution.

However, for the cylinder case, there are no analytical solutions that correlate the tangential displacements with the tangential load. This numerical relationship is fundamental for two aspects: in the linear part, it gives the tangential contact stiffness that can be used in any model that simulate dry friction contact; with the non-linear part, it helps in the construction of the hysteresis friction loop whose area is correlated with the energy dissipated in dry friction dampers.

Stick Area Semi-width

$$c = a \left(1 - \frac{T}{\mu N} \right)^{1/2} \quad (2.12)$$

where

- c is the radius of the stick area
- a is the contact area radius, calculated with Hertz formula
- T is the tangential force
- N is the normal force
- μ is the friction coefficient

Tangential traction distribution

$$\left\{ \begin{array}{ll} \tau = \frac{2\mu N}{\pi a} \left(1 - \left(\frac{x}{a}\right)^2\right)^{1/2} & \text{with } c \leq x \leq a \\ \tau = \frac{2\mu N}{\pi a^2} \left[(a^2 - x^2)^{1/2} - (c^2 - x^2)^{1/2} \right] & \text{with } x \leq c \end{array} \right. \quad (2.13)$$

where τ is the tangential traction in x coordinate.

2.3.1 Specific case: tangential displacement $du=2 \mu m$

As it is explained in Appendix A, the normal and the tangential contact problem are decoupled but the tangential solution takes as input the normal force distribution that comes from the normal contact problem solution. The value of the tangential displacement is selected large enough to produce the slip of some nodes of the contact area, but it does not produce the sliding of the entire body.

Stick/Slip areas

In Figure 26, the dark yellow shading represents the numerical stick area, the light yellow shading the numerical slip area; the red squares represent the nodes that are in slipping condition, the blue asterisks the nodes in adhesion. The numerical and the analytical areas are not perfectly coincident but it is important to remember that there is a residual error on contact area coming from normal solution and that the analytical solution is re-adapted for the 'cylinder on a surface' case. Another aspect that is interesting is the presence of some slipping nodes inside the adhesion area of Mindlin solution: the program is simulating what really happens in the contact because in the stick surface close to the borders there are some spots where the normal force is lower due to rugosity or to the body shape and in this spots the slip starts .

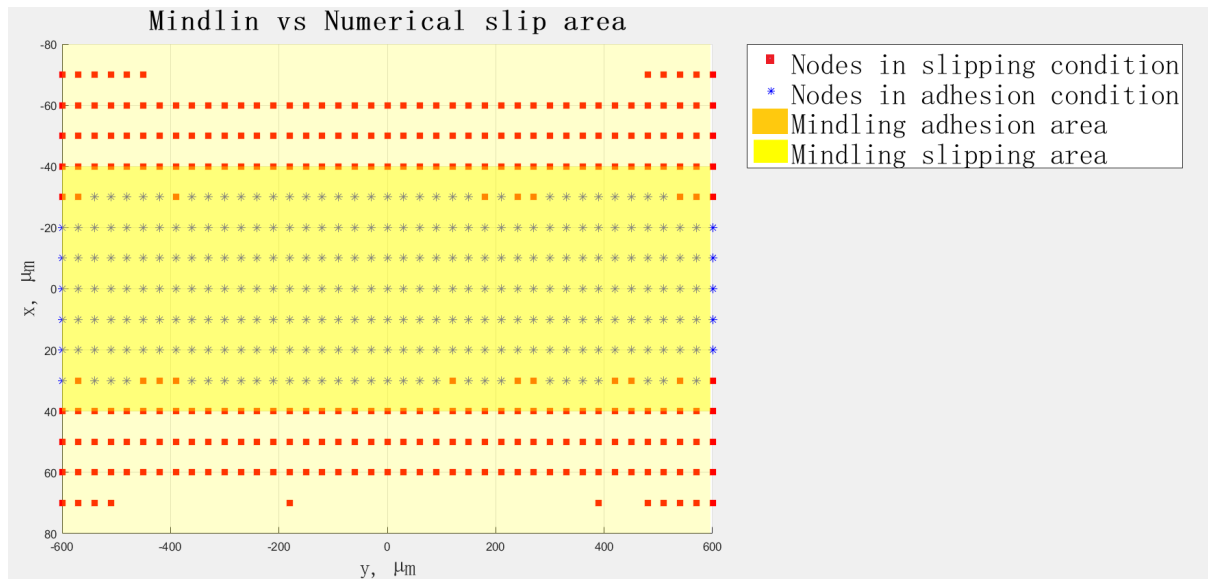


Figure 26: Stick/Slip areas: cylinder.

Tangential traction distribution

In Figure 27 and Figure 28 the distribution of tangential stress of numerical and analytical solution are compared in 3D and in 2D respectively.

Despite the small differences in the stick/slip areas, the two solutions appear to be coincident. Again, the biggest difference is evidenced close to the edges where the MATLAB program can predict the behavior of the system in presence of notch effect whereas the solution proposed by Mindlin is limited to the 2D distribution. The three images at the bottom of Figure 28 show how fast the tangential force increases close to the border.

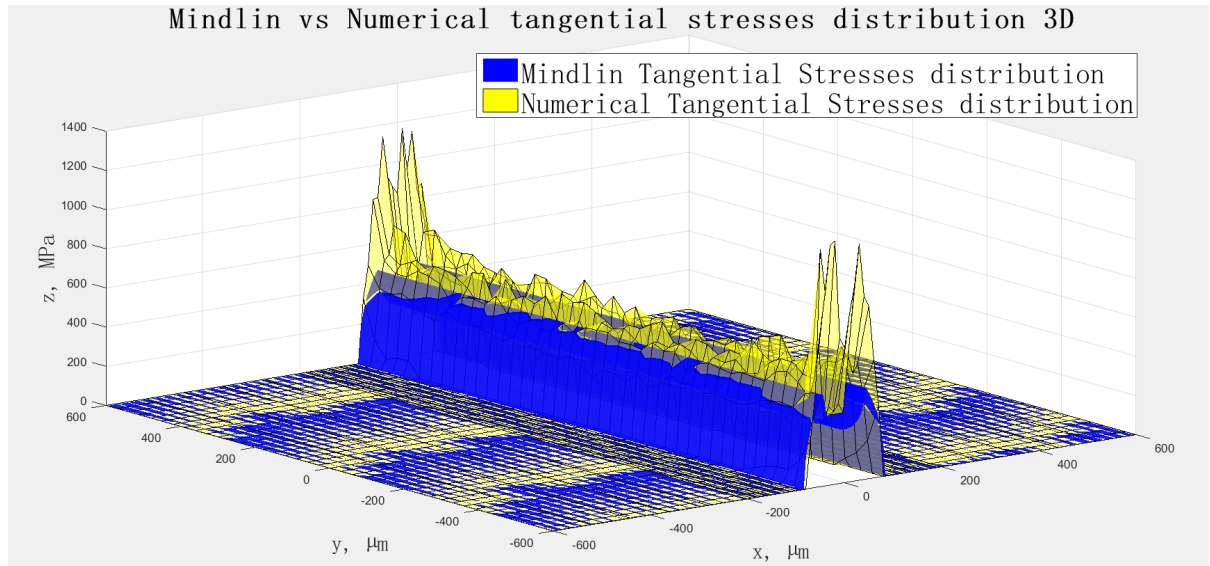


Figure 27: Tangential traction comparison 3D: cylinder.

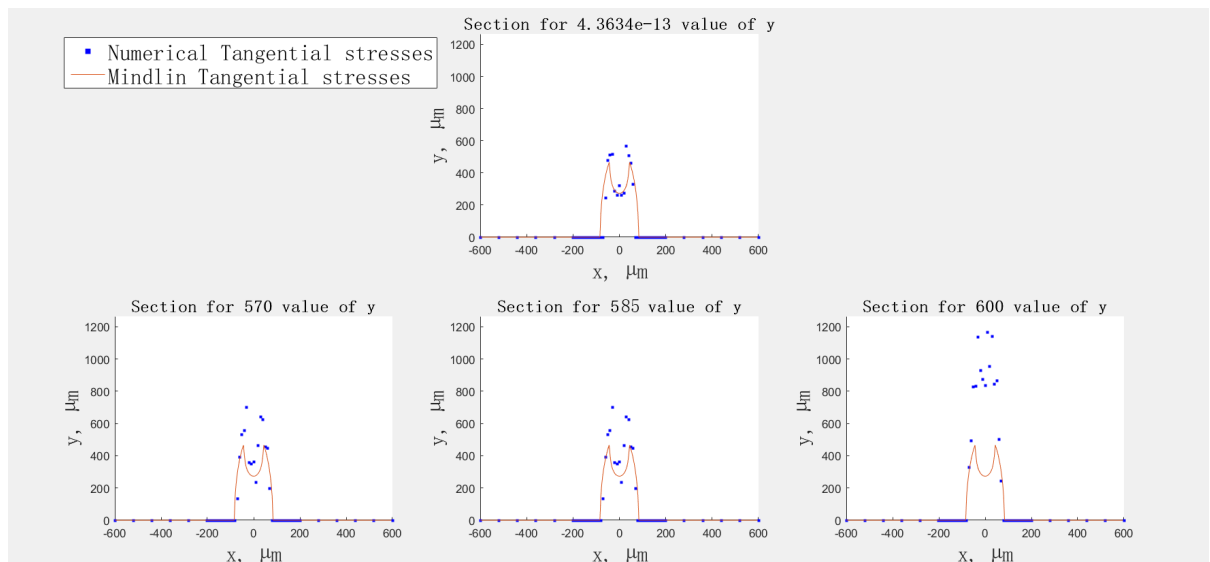


Figure 28: Tangential traction comparison 2D: cylinder.

2.3.2 Tangential displacement against tangential force

The tangential solutions that are represented in this paragraph are obtained in two opposite conditions:

- 'Constant Normal Displacement case' $dz = 5\mu m$
- 'Constant Normal Force case' $NF = 120N$

In CNF case, the limit tangential force is equal for all the tests and consequently it can be used to compare the capability of the different models to dissipate energy and mitigate vibrations in the same conditions.

CND case permits a more detailed description of the elastic part of the curves; in fact, the same analysis that is performed in 2.2.6 for normal approach is repeated here for tangential displacement as a function of tangential force. The difference here is that there are no analytical solutions that can be used as benchmark but the results obtained so far in Appendices A and B and in the first part of Chapter 2 are the proof the approach is reliable.

The models used for the analysis are the same of 2.2.6, but their characteristics are reported again in Table IV so they are easily accessible.

General comparison

To have a broad view of the system behavior, the numerical curves of the 8 models for CND case are shown all together in Figure 29. As expected they do not have the same limit tangential force. There is a strong variability among the curves, but the lengths seem to be more incisive because the trends of Cylinders with different diameters but with the same length such as 1 and 2, or 3 and 4, tend to cluster.

TABLE IV: DIAMETER AND LENGTH INFLUENCE IN TANGENTIAL APPROACH

Model identifier	Diameter 'D'	Length 'L'	Symbol
Cylinder 1	5000 μm	1200 μm	Δ
Cylinder 2	2500 μm	1200 μm	o
Cylinder 3	5000 μm	2400 μm	Δ
Cylinder 4	2500 μm	2400 μm	o
Cylinder 5	5000 μm	4800 μm	Δ
Cylinder 6	5000 μm	9600 μm	Δ
Cylinder 7	10000 μm	9600 μm	*
Cylinder 8	10000 μm	19200 μm	*

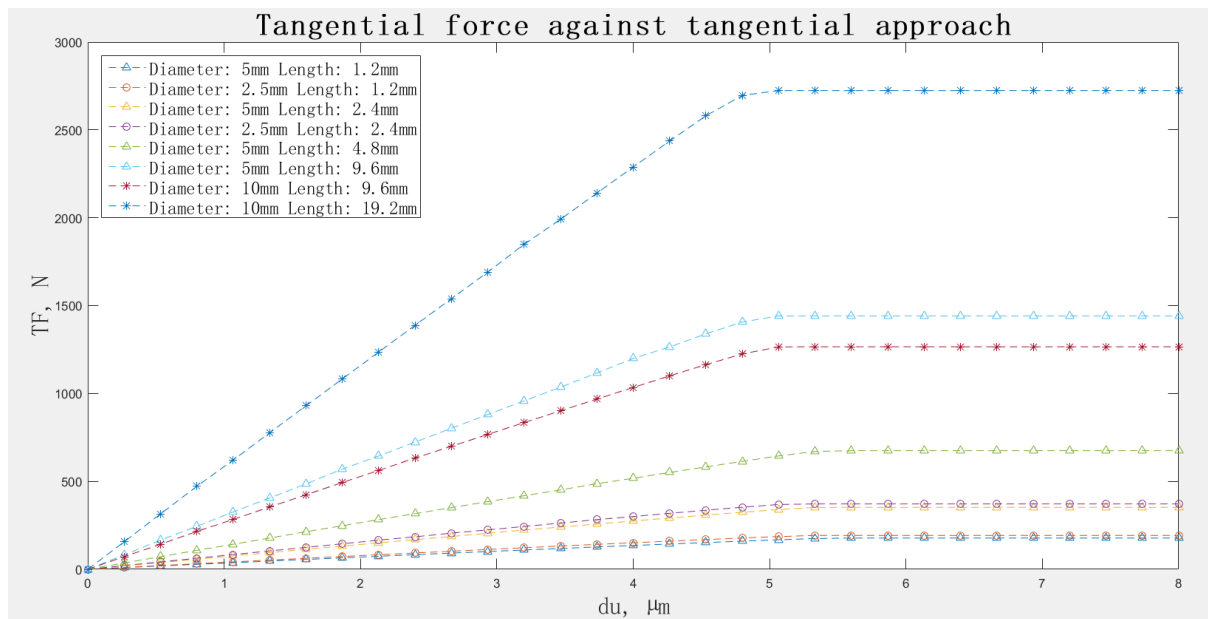


Figure 29: Tangential force vs tangential displacement: cylinders comparison CND case.

TF/L vs du comparison

Following the example of the normal approach, the first idea is to see what happens to the solutions when the TF is divided by the respective cylinder length. The curves are much closer than before but they are still not coincident; the possible causes could be found in a diameter influence or in the fact that the displacement is not linearly proportional to the ratio TF/L.

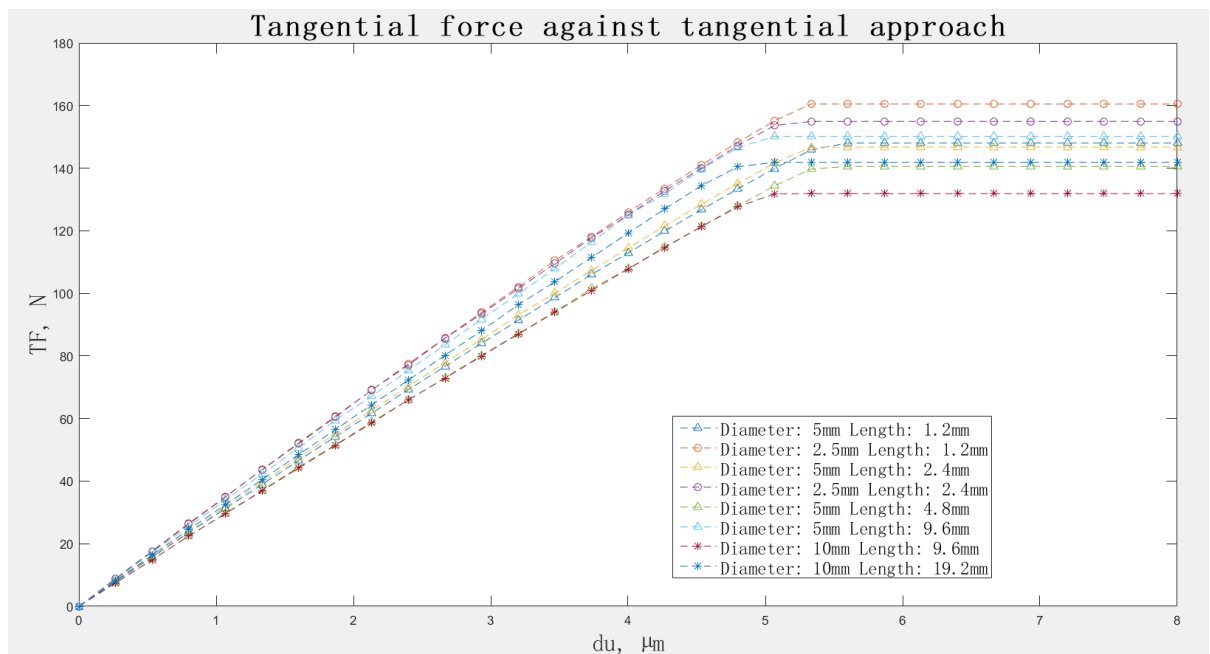


Figure 30: TF/L vs normal displacement: cylinders comparison.

Cylinders with equal diameters comparison

To isolate the various contributions, the curves of the cylinders with different diameters are

represented in separated plots. The result is that there is still a remarkable separation between them (see Figure 31) and the gap is wider as the diameter increases; the cylinder diameter contribution to the tangential displacement can not be neglected.

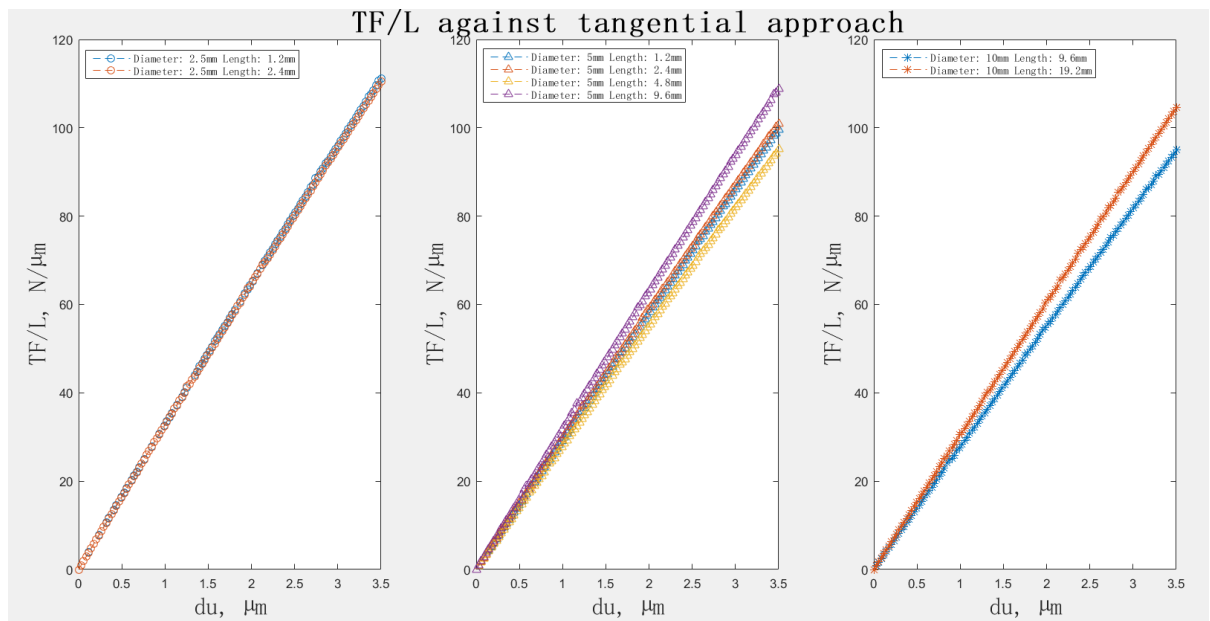


Figure 31: TF/L vs normal displacement: cylinders with equal diameters comparison.

2.3.2.1 Tangential approach: numerical formulation

Using all the results that are available so far, it is possible to extrapolate a formulation for the tangential approach similar to the one obtained for the normal approach. The most difficult part is to understand what parameters can affect the tangential approach because no analytical

TABLE V: NORMAL AND TANGENTIAL APPROACH: EXPONENTS COMPARISON

Exponents	Normal approach	Tangential approach
F	0.917	1.010
L	0.928	1.052
D	0.099	0.144

solutions are available. However, it has been proven that the length and the diameter have a strong influence, so it is correct to guess that the tangential approach has the same structure of the normal approach.

The numerical formulation obtained for the tangential approach is the following:

$$\delta = 14.337 \left(\frac{F^{1.010}}{L^{1.052}} \right) D^{0.144} \quad \text{with } [D] = [L] = \mu m \text{ and } [F] = N \quad (2.14)$$

The unit of measurement of δ is μm : it is fundamental the use of the correct UoM to get meaningful results. In Table V, the coefficient of normal and tangential approach expressions are compared and it is evident that for all the parameters the influence they have is slightly increased.

Finally, the curves of the actual numerical results are set side by side with that calculate with the equation derived (Figure 32). The equation is able to simulate perfectly the behavior of the numerical system when the diameter length is small, instead as it increases a small gap between numerical and equation solutions appears.

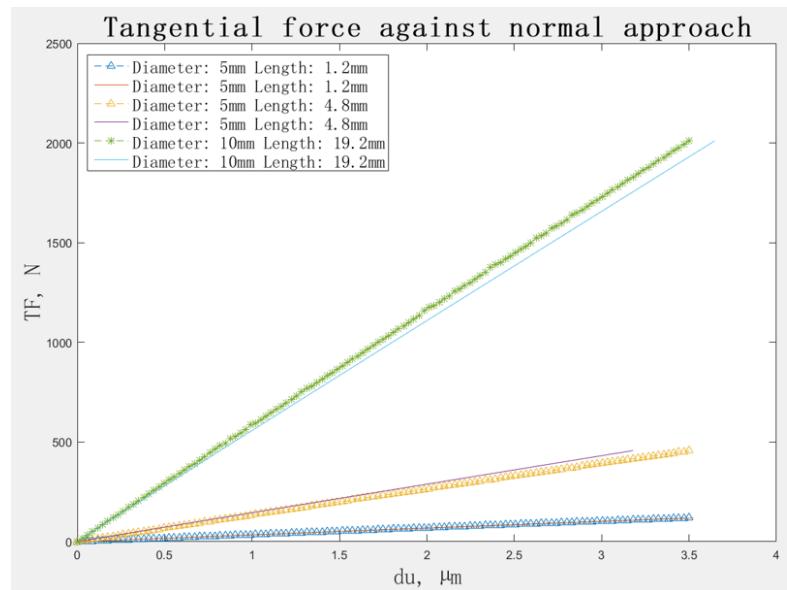


Figure 32: Tangential force vs du : numerical equation and results.

2.3.2.2 Frictional hysteresis loop

The curve that relates tangential force and displacements can be used as *virgin curve* to derive the frictional hysteresis loop using Masing's Rule [27]. Masing developed this model to describe the elasto-plastic behavior of the material but there are a lot of papers where his result is extended to different fields, even to the study of friction [28] [29].

The Masing rule is formulated as follows:

$$F = \begin{cases} f(x) & (x \geq 0) \\ -f(-x) & (x < 0) \end{cases} \quad (2.15)$$

$$\tilde{F} = \begin{cases} F_r + 2f\left(\frac{x-x_r}{2}\right) & \left(\frac{x-x_r}{2} \geq 0\right) \\ F_r - 2f\left(-\frac{x-x_r}{2}\right) & \left(\frac{x-x_r}{2} < 0\right) \end{cases} \quad (2.16)$$

where

- F is the *virgin curve* function
- \tilde{F} is the function of the hysteresis loop
- F_r is the tangential force value of a point of the the virgin curve that is arbitrary selected as motion reversal location
- x_r is the tangential displacement value that correspond to F_r

In Figure 33, the tangential solutions for different cylinder models in CNF case are presented. All these curves can be used as virgin curve for Masing's rule. The importance of this study is evidenced in Figure 34: the hysteresis loops of cylinder 1 and 2 are represented using the same color and symbol code of Figure 33. The two cylinders are loaded with the same normal force and they undergo the same tangential displacements but they produce two hysteresis loop with very different area. It is fundamental to remark that the loading conditions are extremely variable when the damper is actually operating, however the loading history can be recorded and the equations derived here can describe what happens in a particular state.

In conclusion, it is interesting to report an important result that Den Hartog derived in his paper [30]: even if apparently the maximum area for the frictional hysteresis loop can be obtained for infinite value of the tangential stiffness, the damping capacity in that condition is almost null.

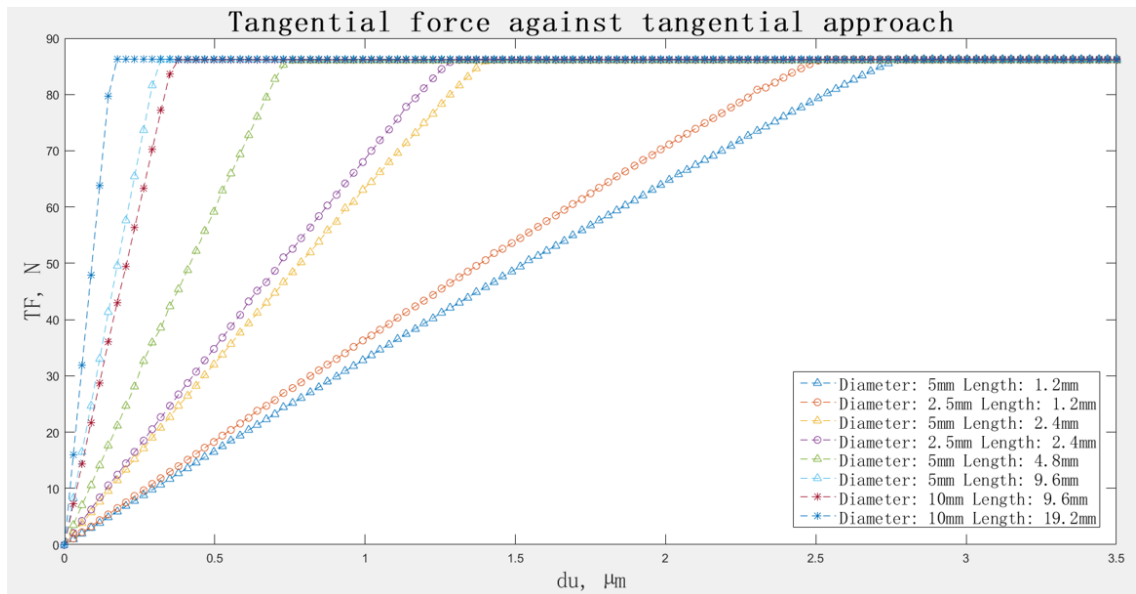


Figure 33: Tangential force vs tangential displacement: cylinders comparison CNF case.

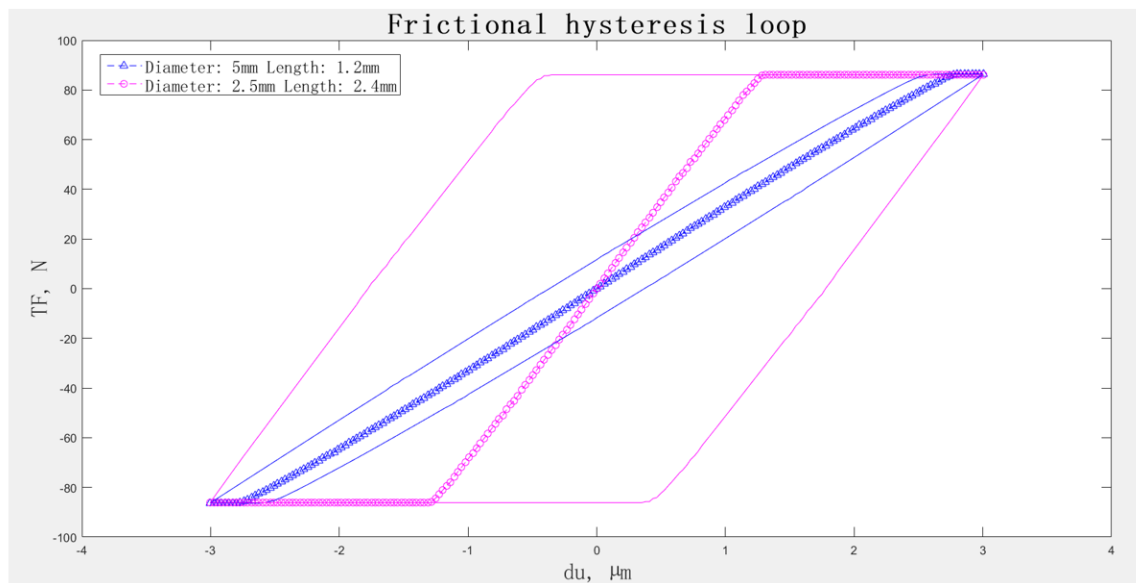


Figure 34: Frictional hysteresis loop comparison: cylinders 1 and 4.

CHAPTER 3

PLANE ON PLANE CONTACT

This chapter deals with the contact between a plane and a planar surface of a possible dry friction damper that is represented in Figure 35. There are no analytical solution neither for the normal contact problem nor for the tangential one, that is why a numerical approach is fundamental. The MATLAB program has another advantage, that is related to the computational time: this kind of contact problem requires a lot of computational power and processing time, but decoupling the normal and the tangential problems (in Appendix B it is proven that it is not an issue) it is possible to get the solutions in few hours.

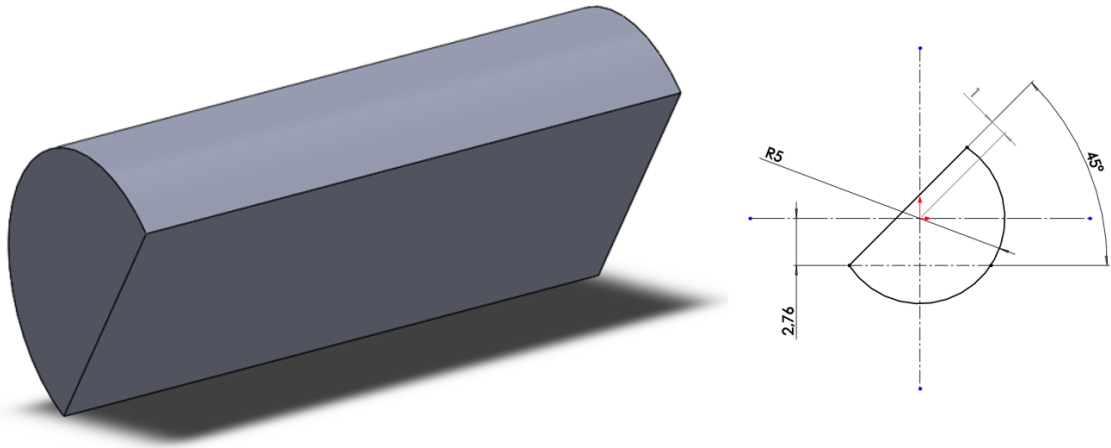


Figure 35: Damper 45°.

The focus here is shifted in particular on the behavior of the tangential force-displacement curves when the normal force has an offset from the cylinder axis, so not all the damper surface is in contact and the pressure distribution is variable.

3.1 Bodies design and mesh generation

The bodies required for the simulation are a damper and a plane. In order to have a large surface for the displacements of distant nodes (see Appendix A), a cut is performed in the damper that makes it symmetric with respect to a plane that contains its axis (Figure 36); this leads to an increase in damper vertical stiffness but it does not affect the tangential stiffness that is investigated in this chapter. This large surface is useful also in the analysis of the system when an eccentric force is applied because non-uniform displacements can be utilized. Again, ANSYS apdl modeling environment is used and the 'hard points projection techniques' (see Appendix B.1.2) is preferred.

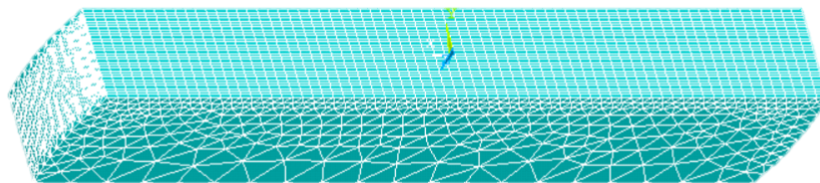


Figure 36: Damper model: plane-plane contact.

The model radius is selected considering an example of damper that is actually used for experiments [31]:

- $DR = 5,000 \mu\text{m}$
- $DW = 1,200 \mu\text{m}$

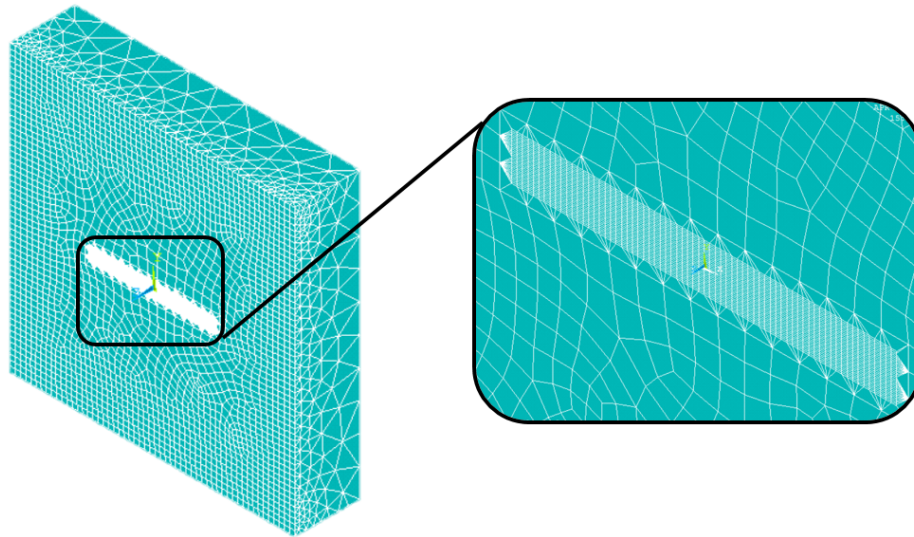


Figure 37: Damper model: plane-plane contact.

3.2 Normal contact problem

Since no analytic solutions are available, in this part the physics of the numerical solution is checked. To begin with, in Figure 38 the distribution of normal pressure in contact area is represented; the pressure is higher at the contact surface borders where the 'edge effect' is

predominant and it gradually decreases moving inwards respecting exactly what was expected. For this specific case, a value of 500 N is used as normal force target: it is higher compared to the one used for cylinder and sphere but it generates much smaller pressure. It is because the load is distributed in a wider area that is completely exploited.

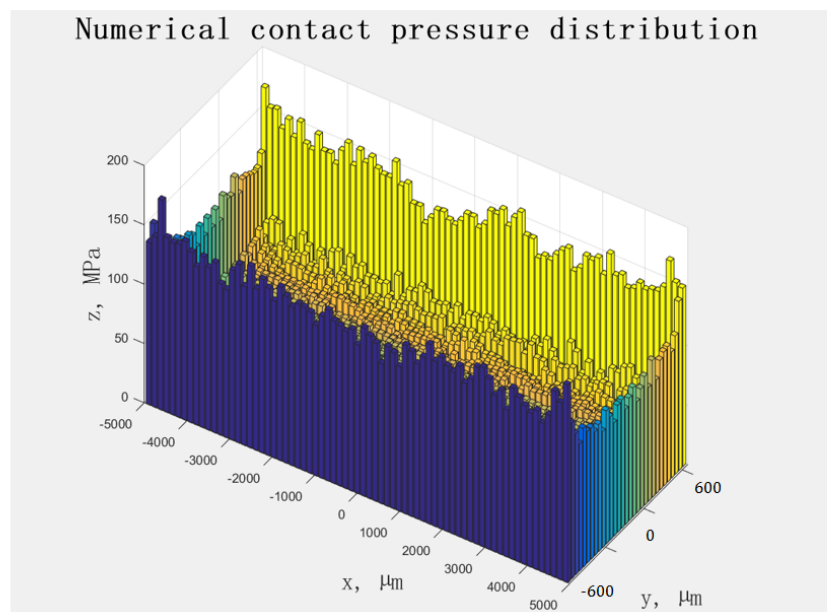


Figure 38: Numerical pressure distribution: plane.

Figure 39 and Figure 40 show dz , mean and max pressure curves for several loading conditions. They have a linear trend that is connected to the elastic compression of the two bodies: the slope of the dz -NF curve is the Young's modulus.

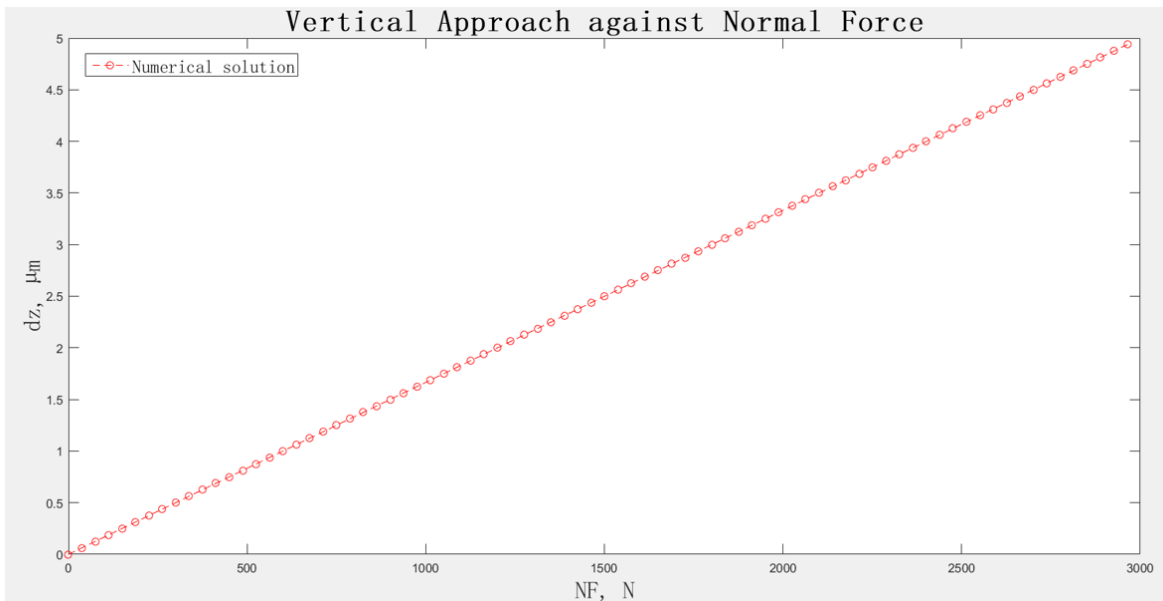


Figure 39: Dz vs normal force: plane.

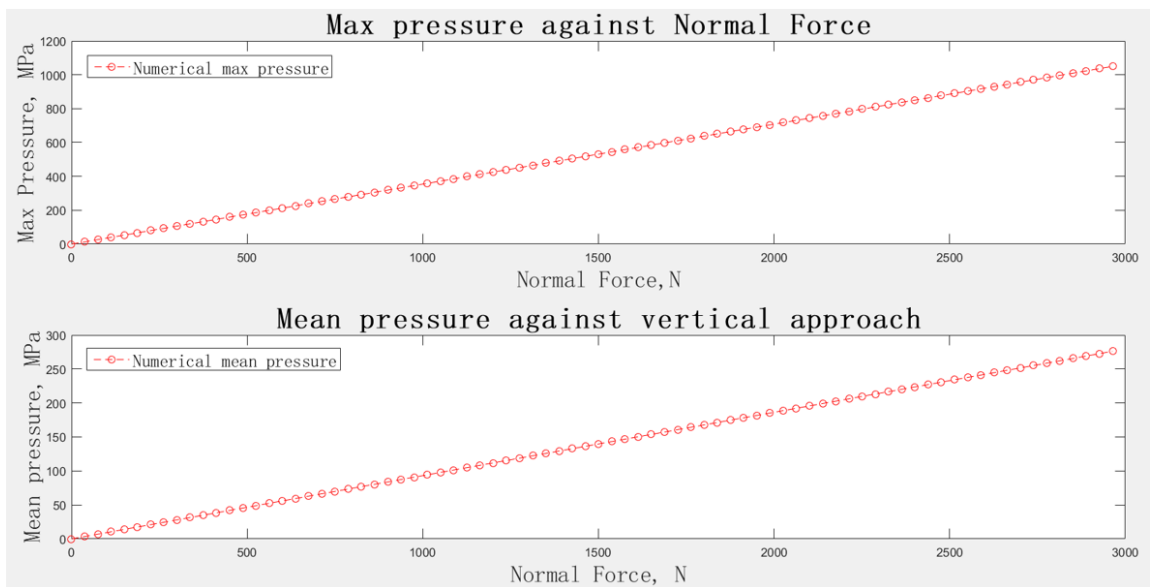


Figure 40: Mean pressure vs dz: plane.

3.3 Tangential contact problem

No analytical solutions are present even for the plane on plane tangential contact problem. The body is subjected to the same pressure distribution of the previous paragraph, that $N_F=500$ N generates, and then a tangential displacement $du=3.6 \mu m$ is added. The result is the tangential forces distribution of Figure 41 and the slip of Figure 43. It is extremely interesting to see that the zones that are mainly interested by slip are the borders, where the tangential force is higher, and the center of the contact area, where the pressure has the lowest value. A more detailed description of the nodes in slip or adhesion is shown in Figure 42.

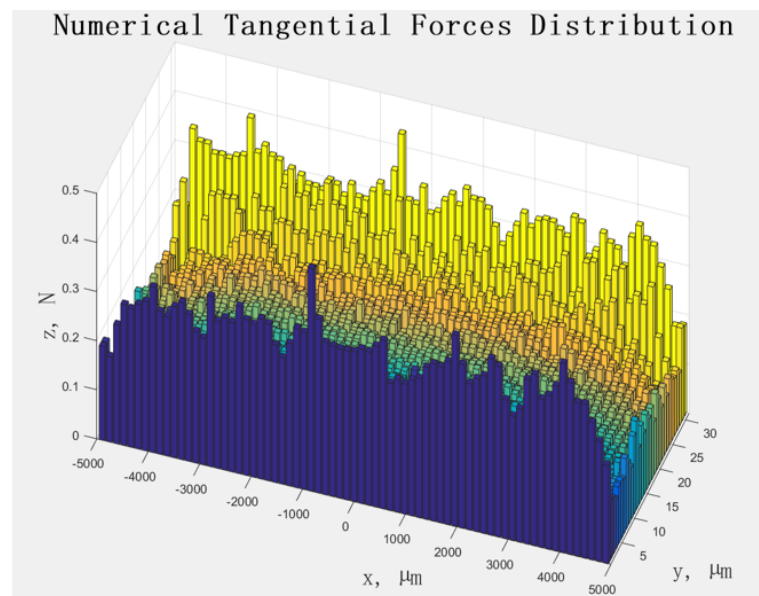


Figure 41: Tangential traction distribution: plane.

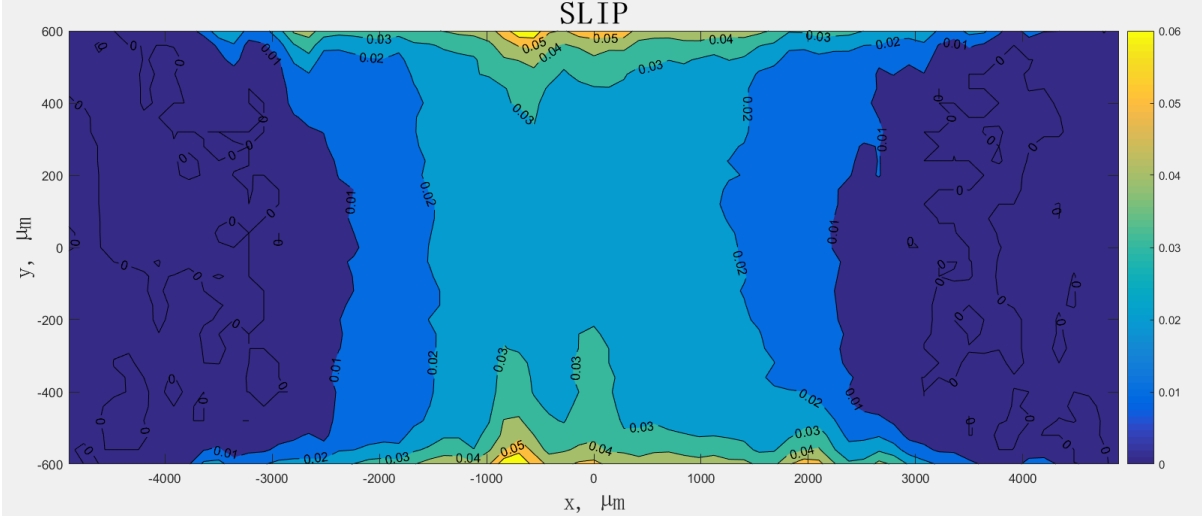


Figure 42: Slip distribution: plane.

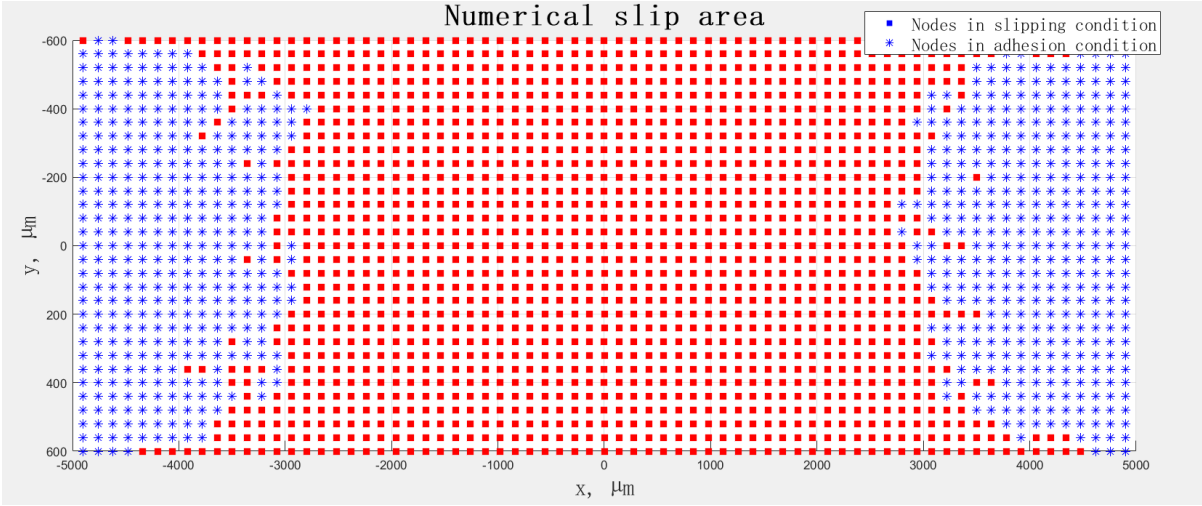


Figure 43: Stick/Slip nodes: plane.

3.3.1 Tangential displacement against tangential force

The normal pressure is not always uniformly distributed on the contact surface and the cause is illustrated in Figure 44. In 'case a' there are no tangential forces acting in the center of gravity so the normal force at the base, NF_b , is in the center; in 'case b' the presence of the tangential forces shifts the NF_b base point on the right so the pressure distribution is not symmetric with respect to the center anymore.

The pressure distribution has a strong impact on the tangential force-displacement curve because it is used as input for the solution of the tangential contact problem (through the Amonton's law). Consequently, it affects the frictional hysteresis loop and that is why it is studied in this part.

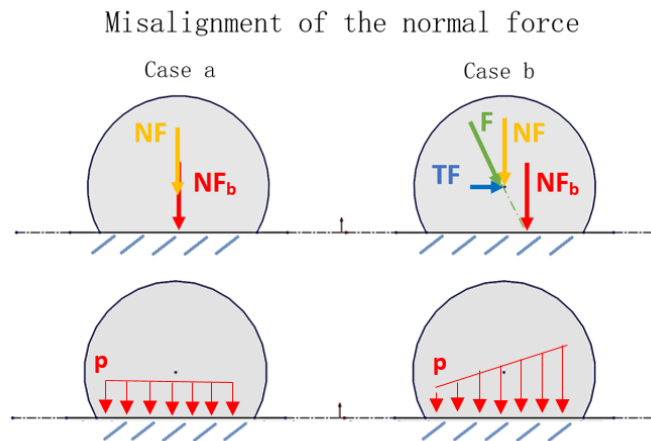


Figure 44: Tangential displacement against tangential force: NF misalignment.

The analysis is divided into two parts, as it is illustrated in Figure 45 and Figure 46.

In the first part, the behavior of the tangential force-displacement curve is investigated considering a constant normal force and three values of eccentricity, and all the pressure distributions that are generated exploit the entire contact area; in the second part, five more values of eccentricity are selected, however in these cases only a portion of the contact area is interested by the pressure distribution and consequently the remaining part is always in slip condition. In order to obtain the eccentricity, a non-uniform distribution of vertical displacements is imposed on the surface that is not involved in the contact: an iterative algorithm checks that the normal force and the eccentricity generated are correct.

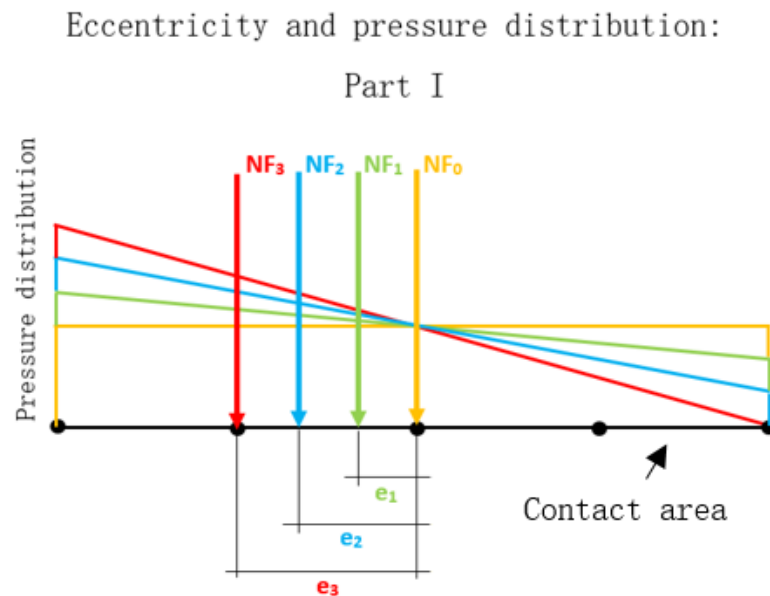


Figure 45: Eccentricity and pressure distribution: part I.

Eccentricity and pressure distribution:

Part II

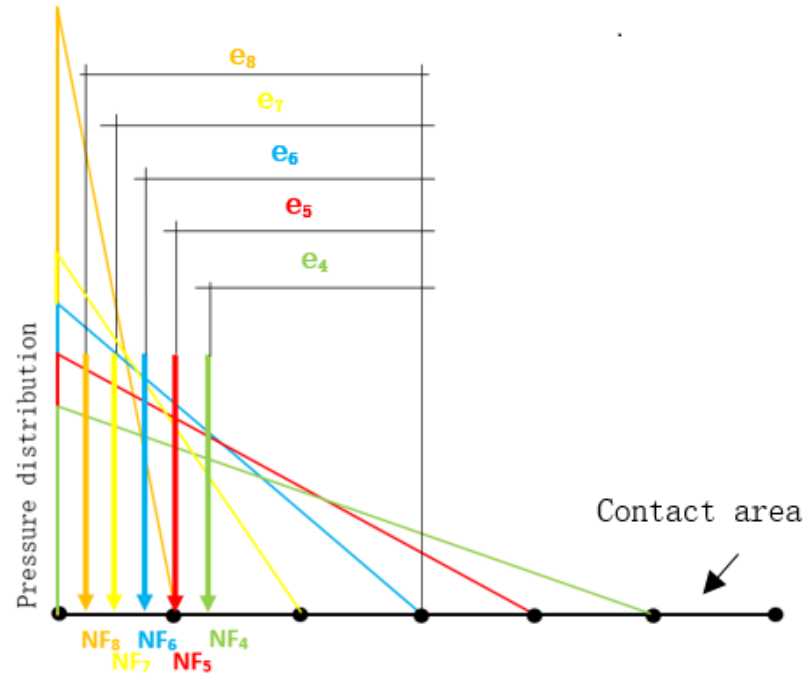


Figure 46: Eccentricity and pressure distribution: part II.

Part I: contact area complete involment

In Figure 47, the tangential force-displacement curves corresponding to the first three values of eccentricity are compared with that of the case where the pressure is uniformly distributed on the surface. They present the same slope in the elastic part, when all the nodes are in stick condition, then they have a different behavior. First of all, the value of du when some nodes start to slip, that coincides with the point where the curves changes slope, is lower for higher

eccentricity and it is justified by the fact that there are nodes with pressure that is more and more low. Secondly, the value of du when all the nodes are in slip condition is higher as the eccentricity increases.

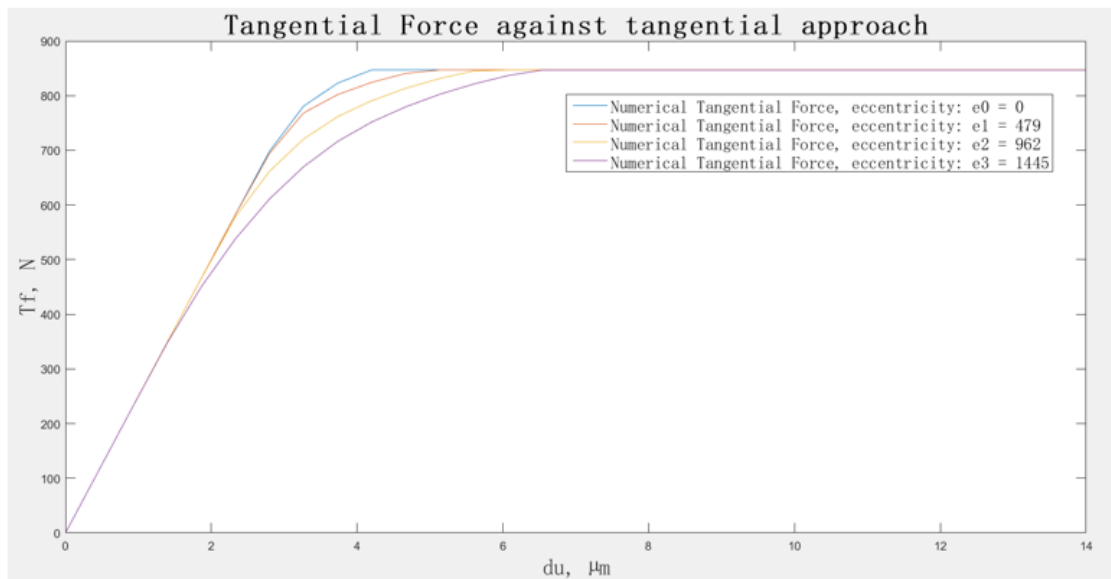
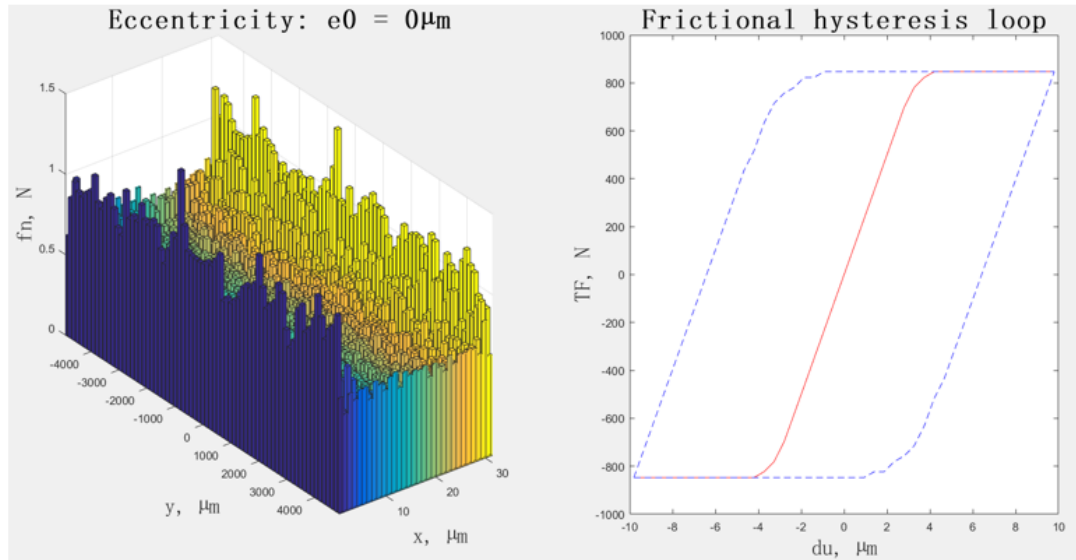
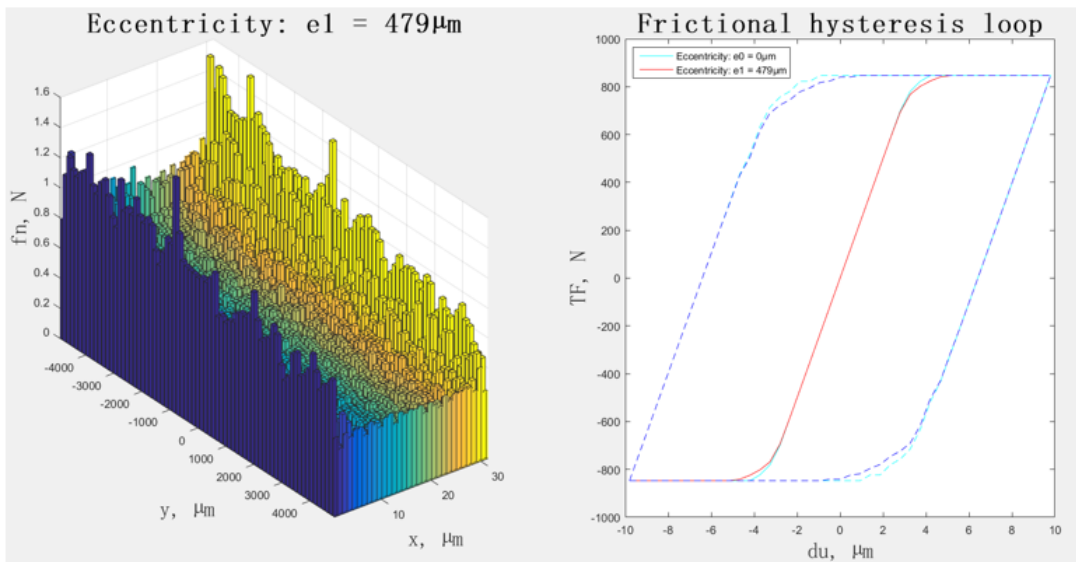


Figure 47: Tangential force vs tangential displacement: eccentricity comparison part I.

In Figure 48, it is shown the frictional hysteresis loop that is generated with a uniform distribution of normal force that is represented on the left (the oscillations that are present in the force distribution graph are the consequence of either 'edge effect' or numerical inaccuracy). It is used in Figure 49, Figure 50 and Figure 51, where it is represented always with azure, as benchmark for the loops area.

Figure 48: Tangential force vs tangential displacement: e_0 .Figure 49: Tangential force vs tangential displacement: e_1 .

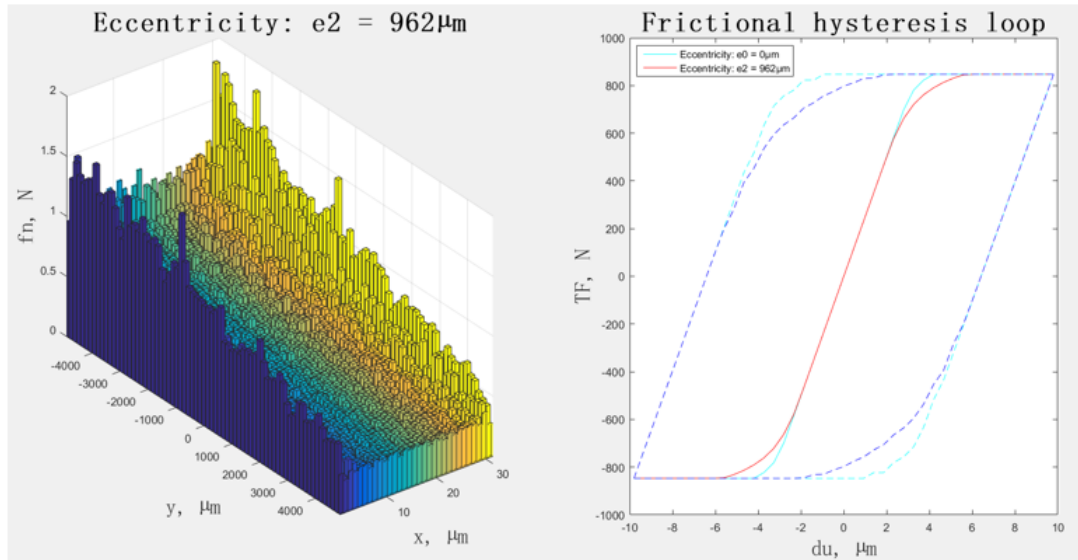


Figure 50: Tangential force vs tangential displacement: e_2 .

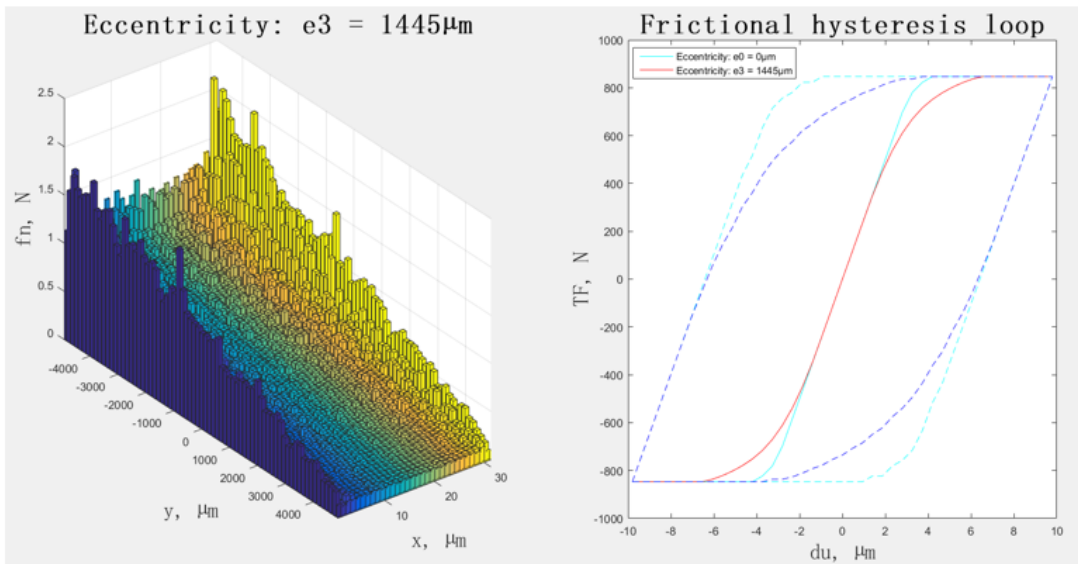


Figure 51: Tangential force vs tangential displacement: e_3 .

It is evident that the area of the loops is reduced as the eccentricity increases but this reduction is not significant for damper's applications.

Part II: contact area partial involvement

When the force distribution involves only a portion of the contact area the situation changes completely. In Figure 52, the dotted azure line refers to the case with zero eccentricity. On the one hand, the curves do not have a common trend even in the elastic part, meaning that the contact elasticity changes in each case. On the other hand, there is not a linear dependence between the slope of the curves and the eccentricity because the lines in the figure are overlapped.

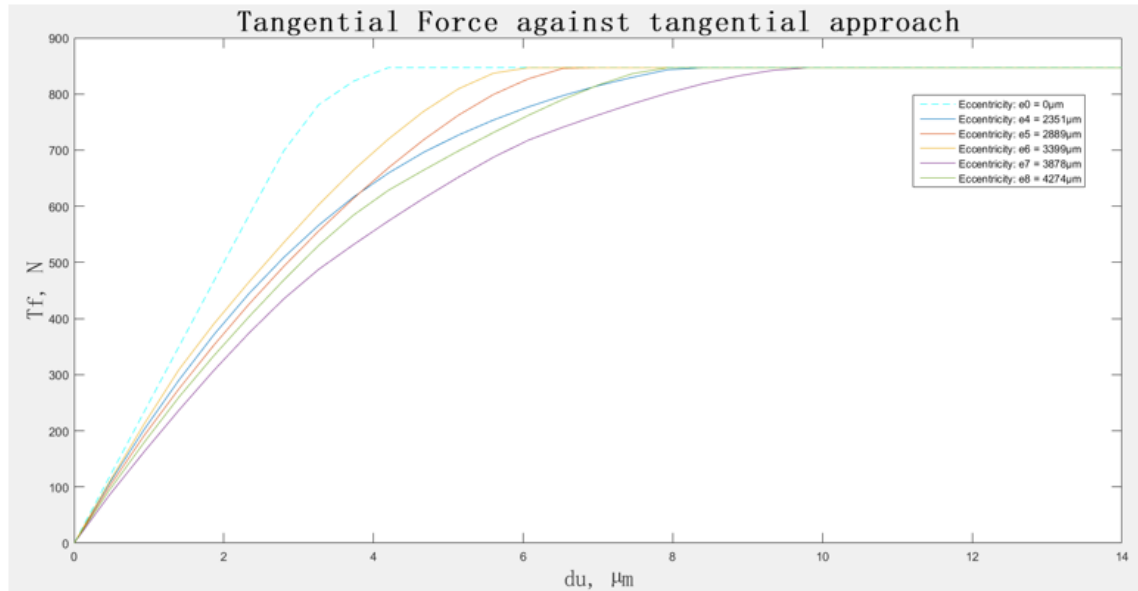


Figure 52: Tangential force vs tangential displacement: eccentricity comparison part II.

In the following figures, the frictional hysteresis loops corresponding to each eccentricity are compared. This time the area reduction of the loops is notable and in particular for $e7$ it is halved. The area do not represent exactly the energy that is dissipated but it gives an idea of the energy dissipation reduction compared to the zero eccentricity case.

As it was explained before, the loading conditions of the dampers are so variable that it is very hard to predict what is the system status using only some equations. It is essential the support of an instrument like the MATLAB program that was developed that can rapidly simulate the behavior of the bodies in contact.

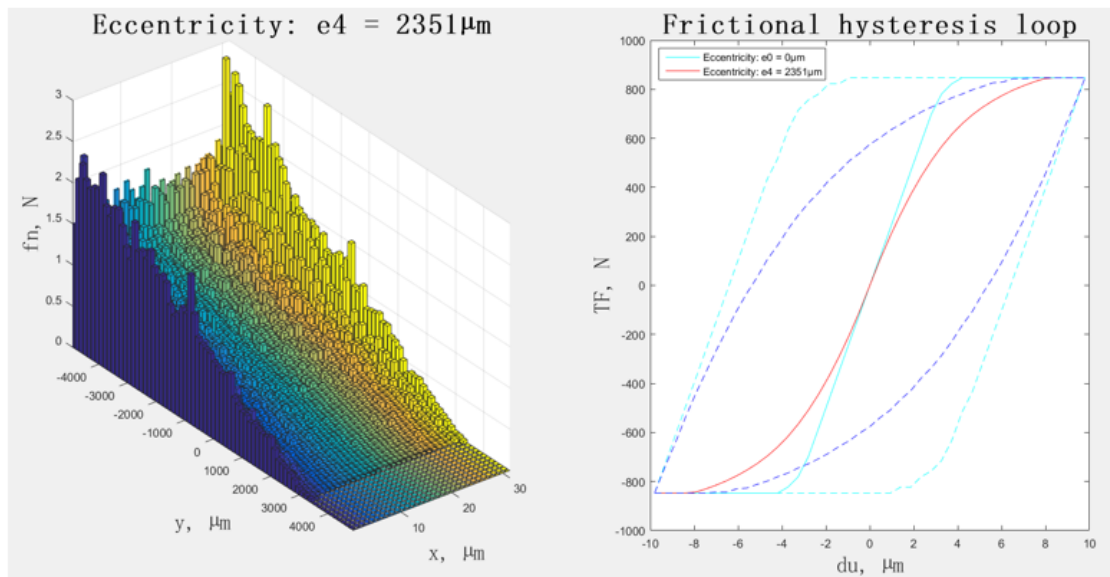


Figure 53: Tangential force vs tangential displacement: $e4$.

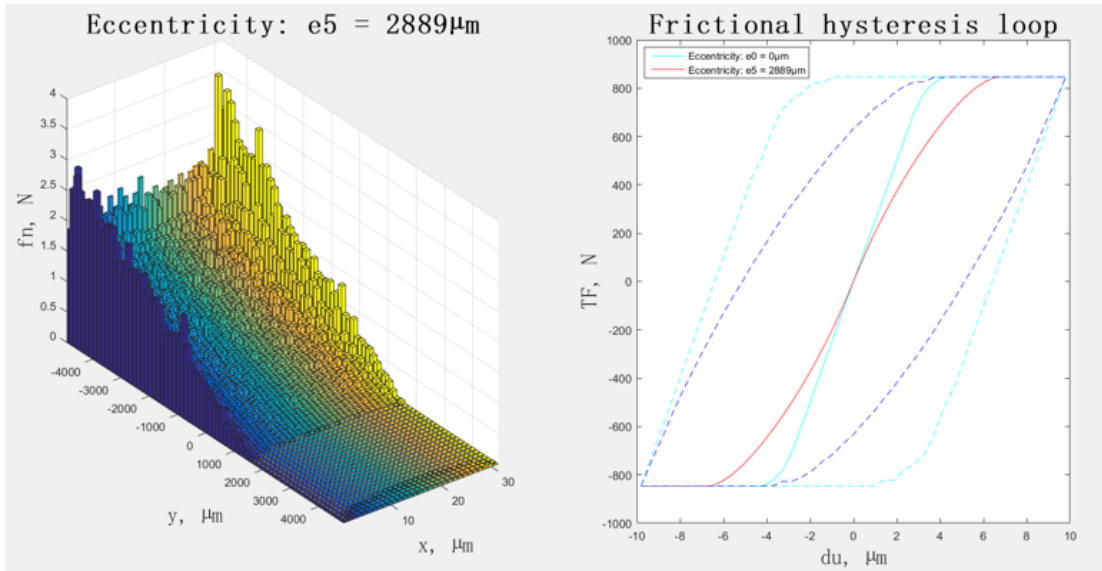


Figure 54: Tangential force vs tangential displacement: e5.

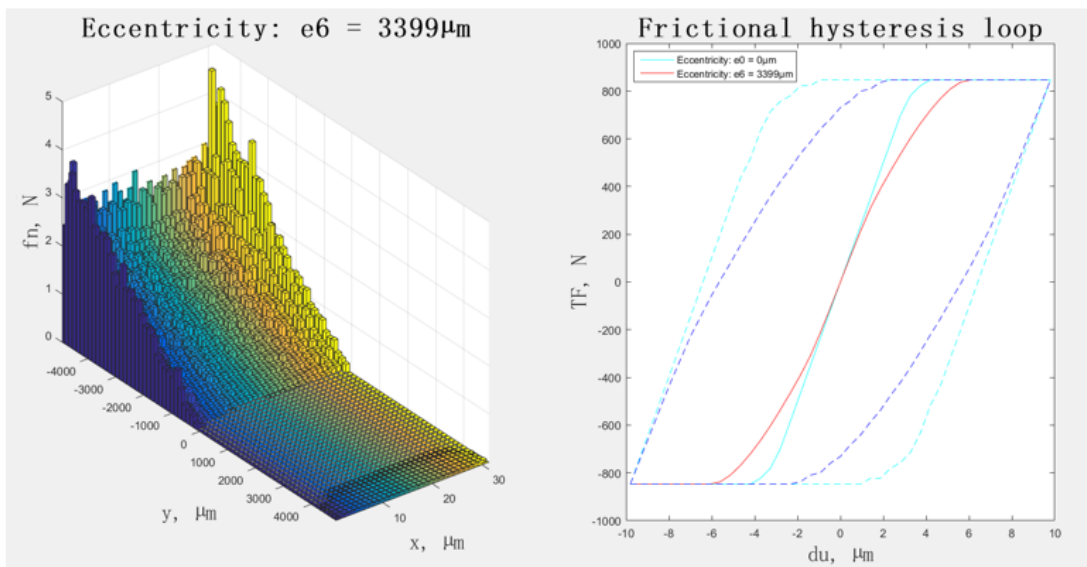


Figure 55: Tangential force vs tangential displacement: e6.

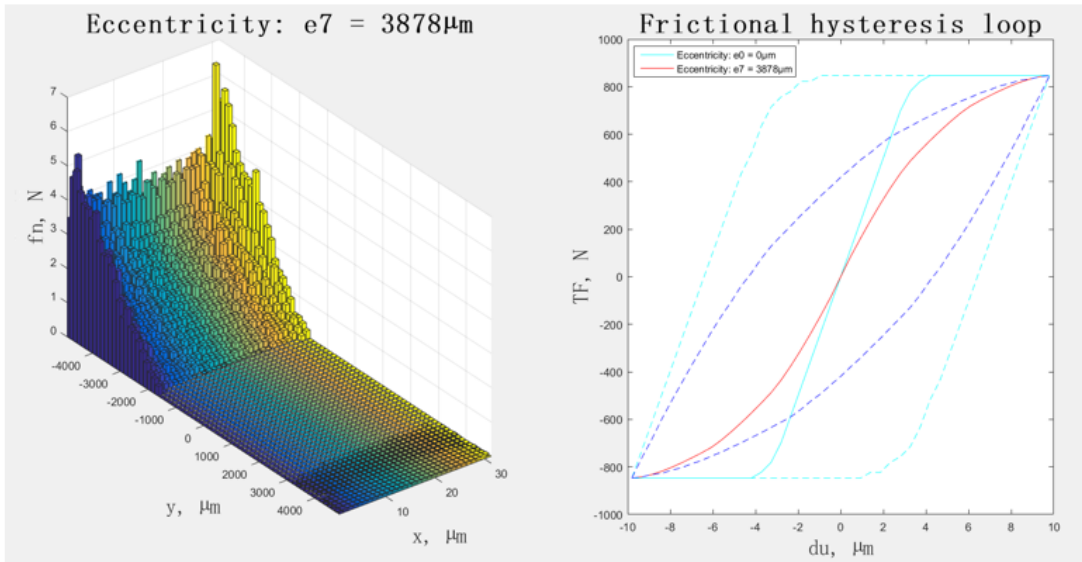


Figure 56: Tangential force vs tangential displacement: e7.

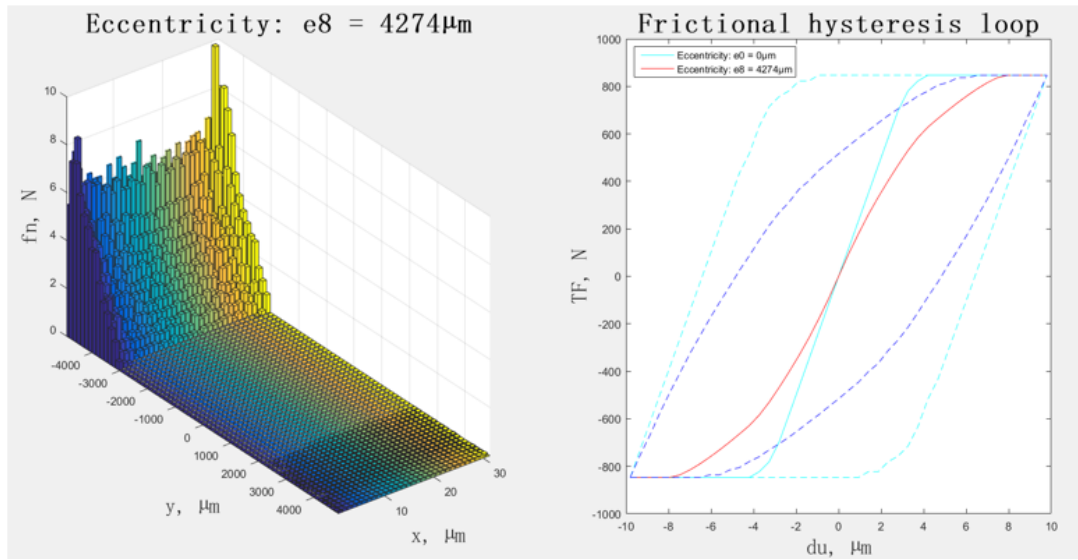


Figure 57: Tangential force vs tangential displacement: e8.

CHAPTER 4

CONCLUSION

The MATLAB program developed for this thesis is an essential tool for the simulation of the dry friction contact between bodies of arbitrary shape. The damping capacity of these systems can be determined with moderate costs in terms of computational time and power. This is very helpful in the design of the dampers utilized in turbomachinery where a high level of customization is required.

The equation derived in 2.3.2 to define the relationship between tangential forces and displacements, and consequently the tangential contact stiffness k_t , is unique and has yet to be described by other researchers. It is important to remember that the value of k_t and the friction coefficient μ are *"sufficient to model the friction interface with high accuracy"* according to Ewins [11]. In future works, the same analysis can be extended to a wider range of models where the influence of factors other than the diameter and length can be investigated.

For what concerns the planar contact, in 3.3.1, the examination of the frictional hysteresis loop for diverse normal pressure distributions revealed that their areas change mainly when the potential contact area is not entirely involved in the contact. The importance of the MATLAB program is confirmed by the fact it is not possible to determine a clear trend in the loop areas for different values of the eccentricity of the normal force so each case needs to be studied separately.

APPENDICES

Appendix A

A NUMERICAL METHOD FOR CONTACT PROBLEM SOLUTION

In Appendix A, it is illustrated the numerical method that is used to solve the normal and the tangential contact problems of elastic bodies. This method represents the core of the programs developed to perform the simulations. It is based on the assumption that the normal and the tangential solutions do not affect each other. There are several experiments [22] [32] that confirm this hypothesis, so mutual influence can be considered irrelevant.

A.1 Normal contact problem solution

In Figure 58, it is reported the procedure that is followed to calculate the vertical displacements u_z and the normal forces f_z in each node of the contact area. It is an iterative process.

A.1.1 PHASE 1 - Stiffness matrices

The essential information regarding the components involved in the simulation are their stiffness matrices. It is possible to get them in different ways, but in this work a commercial software, ANSYS apdl, was used. It allows the modeling and the meshing of the bodies. Further details regarding this phase are in Appendix B.

Appendix A (continued)

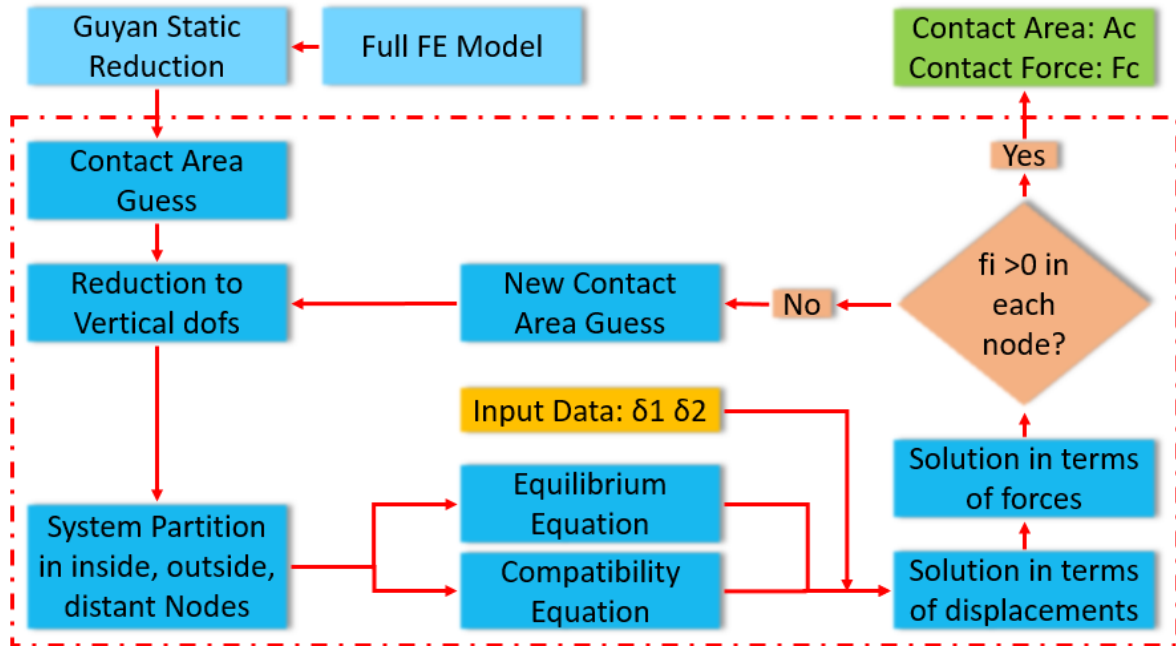


Figure 58: Iterative procedure for normal contact problem.

A.1.2 PHASE 2 - Guyan reduction of stiffness matrices

The matrices obtained so far are too large to be used for computation. Then, a (static) reduction is performed using Guyan method [33]. Starting from the stiffness equation,

$$[K_n]\{x_n\} = \{f_n\} \quad (\text{A.1})$$

Appendix A (continued)

the useful nodes, 'u', are identified and isolated

$$\begin{bmatrix} [K_{uu}] & [K_{ud}] \\ [K_{du}] & [K_{dd}] \end{bmatrix} \begin{Bmatrix} x_u \\ x_d \end{Bmatrix} = \begin{Bmatrix} f_u \\ f_d \end{Bmatrix} \quad (\text{A.2})$$

Making the assumption that the forces in the useless nodes 'd' are null,

$$[K_{du}]\{x_u\} + [K_{dd}]\{x_d\} = \{0\} \quad (\text{A.3})$$

it is possible to get the displacements at this nodes

$$\{x_d\} = -[K_{dd}]^{-1}[K_{du}]\{x_u\} \quad (\text{A.4})$$

The first equation becomes

$$[K_{uu}]\{x_u\} + [K_{ud}][K_{dd}]^{-1}[K_{du}]\{x_u\} = \{f_u\} \quad (\text{A.5})$$

and consequently the transformation matrix

$$[T_s] = \begin{bmatrix} [I] \\ [t_s] \end{bmatrix} = \begin{bmatrix} [I] \\ -[K_{dd}]^{-1}[K_{du}] \end{bmatrix} \quad (\text{A.6})$$

Appendix A (continued)

After this static reduction, the stiffness matrix is the following

$$[K_u^G] = [T_s]^T [K_n] [T_s] \quad (\text{A.7})$$

Among the useful nodes there are

1. the nodes belonging to the potential contact area, 'c' nodes,
2. the nodes belonging to the surface which is more distant from the contact area, 'd' nodes

It is considered a 'potential' contact area because the actual contact area can not be predetermined; its dimension is estimated considering in the analytical solution a force that produce 2000MPa of maximum local pressure.

The force and the displacements are applied to the distant nodes, 'd' nodes, during the simulations.

A.1.3 PHASE 3 - Vertical degree of freedom

At this point, it is possible to further reduce the dimension of the system taking into account only the vertical (z) degree of freedom. The system

$$\begin{bmatrix} K_{zz} & K_{zx} \\ K_{xz} & K_{xx} \end{bmatrix} \begin{Bmatrix} u_z \\ u_x \end{Bmatrix} = \begin{Bmatrix} f_z \\ f_x \end{Bmatrix} \quad (\text{A.8})$$

can be writtten in the form

$$\begin{cases} u_x = K_{xx}^{-1}(f_x - K_{xz}u_z) \\ K_{zz}u_z = f_z - K_{zx}u_x \end{cases} \quad (\text{A.9})$$

Appendix A (continued)

and in particular the second equation becomes

$$(K_{zz} - K_{zx}K_{xx}^{-1}K_{xz})u_z = f_z - K_{zx}K_{xx}^{-1}f_x \quad (\text{A.10})$$

or

$$\widetilde{K}_{zz}u_z = f_z^* \quad \text{with} \quad \begin{cases} \widetilde{K}_{zz} = (K_{zz} - K_{zx}K_{xx}^{-1}K_{xz}) \\ f_z^* = f_z - K_{zx}K_{xx}^{-1}f_x \end{cases} \quad (\text{A.11})$$

The hypothesis that the tangential and the normal contact problems are independent can be interpreted considering the force f_x null in the normal case. It means that $f_z^* = f_z$.

A.1.4 PHASE 4 - Contact area hypothesis

The solution process is iterative because it is not possible to predetermine which nodes belong to the contact area. To begin with, it is assumed that all the nodes of the potential contact area are actually taking part to the contact. In the following iterations it will not be necessary anymore to make assumptions regarding the contact area, but every time the nodes with a negative normal force will be excluded from the latter.

A.1.5 PHASE 5 - Nodes outside contact area reduction

The matrix equation is reduced again, excluding the nodes 'o' outside the contact area. First of all, it is necessary to reorder the matrices to separate the nodes 'i' inside the contact

Appendix A (continued)

area, the nodes 'o' outside the contact area and the distant nodes 'δ'.

From now on, all the stiffness matrices \tilde{K} will be indicated as K for simplicity.

$$K_{zz}u_z = \begin{bmatrix} K_{zii} & K_{zio} & K_{zi\delta} \\ K_{zoi} & K_{zoo} & K_{z\delta\delta} \\ K_{z\delta i} & K_{z\delta o} & K_{z\delta\delta} \end{bmatrix} \begin{Bmatrix} u_{zi} \\ u_{zo} \\ u_{z\delta} \end{Bmatrix} = \begin{Bmatrix} f_{zi} \\ f_{zo} \\ f_{z\delta} \end{Bmatrix} \quad (\text{A.12})$$

Considering null the forces outside the contact

$$u_{zo} = -K_{zoo}^{-1}(K_{zoi}u_{zi} + K_{z\delta o}u_{z\delta}) \quad (\text{A.13})$$

Following the same reduction procedure of phase 3, the nodes 'o' outside the contact area are reduced and the stiffness equation becomes

$$\begin{bmatrix} K_{zii} & K_{zi\delta} \\ K_{z\delta i} & K_{z\delta\delta} \end{bmatrix} \begin{Bmatrix} u_{zi} \\ u_{z\delta} \end{Bmatrix} = \begin{Bmatrix} f_{zi} \\ f_{z\delta} \end{Bmatrix} \quad (\text{A.14})$$

with

$$\begin{cases} K_{zii_{new}} = K_{zii} - K_{zio}K_{zoo}^{-1}K_{zoi} \\ K_{zi\delta_{new}} = K_{zi\delta} - K_{zio}K_{zoo}^{-1}K_{z\delta o} \end{cases} \quad (\text{A.15})$$

A.1.6 The minimization of Potential Energy Equation

In order to proceed, it is necessary to express the compatibility equation of the problem and it can be deduced from the minimization of the potential energy equation.

Appendix A (continued)

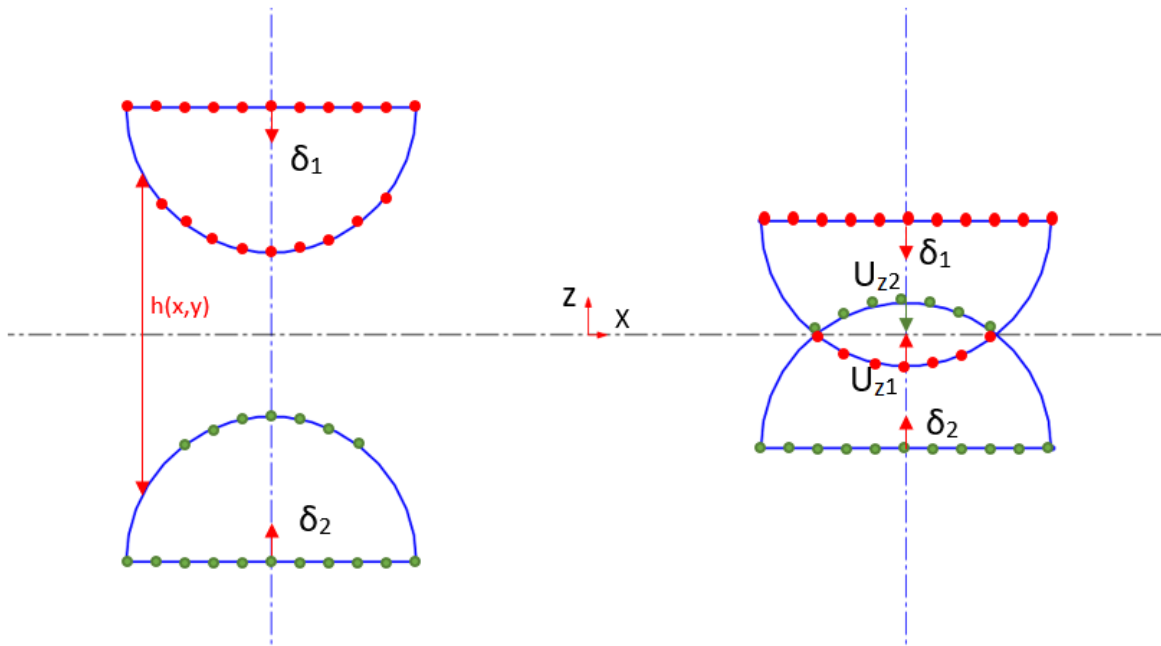


Figure 59: Potential energy equation: elements display.

The potential energy equation for the two bodies in contact is

$$E = \frac{1}{2} \left(\int_S p(\mathbf{u}_{z1} - \mathbf{u}_{z2}) + \int_S p(h - \delta_1 - \delta_2) \right) \quad (\text{A.16})$$

where

- δ (approach) is the sum of the rigid movements of the two bodies; in the simulations it corresponds to the movement of the distant nodes
- $h(x,y)$ is the initial distance between the nodes of the two bodies
- p is the pressure over the contact area

Appendix A (continued)

- S is the surface over which p acts

The function has its minimum when

$$h - \delta_1 - \delta_2 + \mathbf{u}_{z1} - \mathbf{u}_{z2} \geq 0 \quad (\text{A.17})$$

and in particular

1. >0 for nodes outside contact area
2. $=0$ for nodes inside contact area

A.1.7 PHASE 6 - Contact area nodes normal displacements

Starting from equilibrium equation and compatibility equation, it is possible to define eventually the displacements at the nodes belonging to the contact area.

Equilibrium equation

$$f_{zi1} + f_{zi2} = 0 \quad (\text{A.18})$$

where

$$\begin{cases} f_{zi1} = K_{zii1}u_{zi1} + K_{zi\delta1}u_{z\delta1} \\ f_{zi2} = K_{zii2}u_{zi2} + K_{zi\delta2}u_{z\delta2} \end{cases} \quad (\text{A.19})$$

leads to

$$K_{zii1}u_{zi1} + K_{zi\delta1}u_{z\delta1} + K_{zii2}u_{zi2} + K_{zi\delta2}u_{z\delta2} = 0 \quad (\text{A.20})$$

Compatibility equation

$$u_{zi2} = h(x, y) + u_{zi1} - (\delta_1 + \delta_2) \quad (\text{A.21})$$

Appendix A (continued)

The final expression for vertical displacements is

$$(K_{zii1} + K_{zii1})u_{zi1} = -(K_{zi\delta1}u_{z\delta1} + K_{zi\delta2}u_{z\delta2}) - K_{zii2}(h(x, y) - (\delta_1 + \delta_2)) \quad (\text{A.22})$$

A.1.8 PHASE 7 - Normal forces and contact area modification

Knowing the vertical displacements in each point of the contact area, the normal forces can be computed

$$f_{zi1} = K_{zii1}u_{zi1} + K_{zi\delta1}u_{z\delta1} \quad (\text{A.23})$$

If there are any nodes where the normal force is less than or equal to zero, these nodes are shifted in the nodes outside the contact area and the procedure is repeated, starting from PHASE 5, until convergence.

A.2 Tangential contact problem solution

The solution of the tangential contact problem is based on Amontons' law of friction[34]. It states that *"the lateral friction force generated by two bodies in contact is directly proportional to the normal applied load"*; the constant of proportionality is the friction coefficient and it is constant, it depends on the materials of the two bodies, but it is independent of the contact area, the sliding velocity and the surface roughness.

$$\frac{|f_x(x, y)|}{p(x, y)} = \frac{|T|}{N} = \mu \quad (\text{A.24})$$

Appendix A (continued)

Ollerton and Hains experimental studies[35] that were conducted exploiting photo-elasticity properties of epoxy resins, confirm this theory.

In the following picture, it is reported the procedure that is followed to calculate the tangential displacements u_x and the tangential forces f_x in each node of the contact area. In this case, the contact area is fixed and it is the one calculated in the solution of the normal contact problem[14]. However this is again an iterative process where the number of nodes in slip or stick condition is unknown.

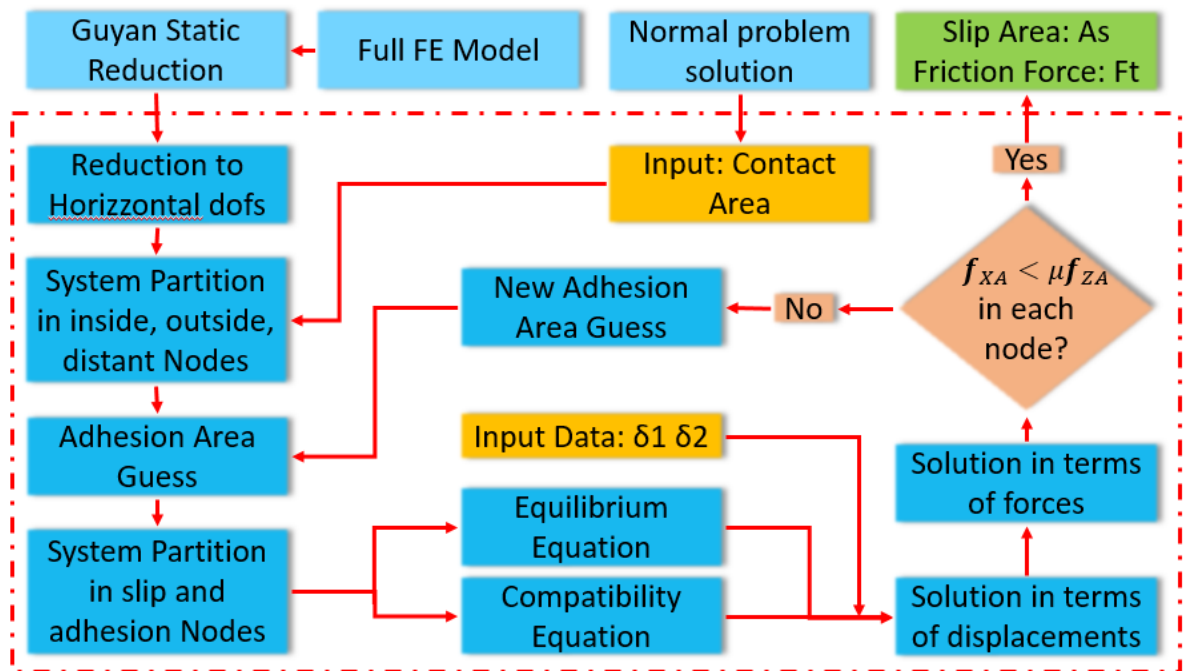


Figure 60: Iterative procedure for tangential contact problem.

Appendix A (continued)

PHASE 1 and **PHASE 2** are the same of normal contact problem solution so they will not be repeated.

A.2.1 PHASE 3 - Vertical degree of freedom

In this phase, it is necessary to reduce the dimension of the system taking into account only the tangential (x) degree of freedom. The other degree of freedom, (y) direction, is not mentioned because the relative movement of the bodies happens only in (x) direction. The matrix system

$$\begin{bmatrix} K_{zz} & K_{zx} \\ K_{xz} & K_{xx} \end{bmatrix} \begin{Bmatrix} u_z \\ u_x \end{Bmatrix} = \begin{Bmatrix} f_z \\ f_x \end{Bmatrix} \quad (\text{A.25})$$

can be written in the form

$$\begin{cases} u_z = K_{zz}^{-1}(f_z - K_{zx}u_x) \\ K_{xx}u_x = f_x - K_{xz}u_z \end{cases} \quad (\text{A.26})$$

and in particular the second equation becomes

$$(K_{xx} - K_{xz}K_{zz}^{-1}K_{zx})u_x = f_x - K_{xz}K_{zz}^{-1}f_z \quad (\text{A.27})$$

or

$$\widetilde{K}_x u_x = f_x^* \quad \text{with} \quad \begin{cases} \widetilde{K}_x = (K_{xx} - K_{xz}K_{zz}^{-1}K_{zx}) \\ f_x^* = f_x - K_{xz}K_{zz}^{-1}f_z \end{cases} \quad (\text{A.28})$$

The hypothesis that the tangential and the normal contact problems are independent can be interpreted considering the force f_x null in the normal case. It means that $f_x^* = f_x$.

Appendix A (continued)

A.2.2 PHASE 4 - Nodes outside contact area reduction

The matrix equation is further reduced, excluding the nodes 'o' outside the contact area.

From now on, all the stiffness matrices \tilde{K} will be indicated as K for simplicity.

$$K_{xx}u_x = \begin{bmatrix} K_{xii} & K_{xio} & K_{xi\delta} \\ K_{xoi} & K_{xoo} & K_{xo\delta} \\ K_{x\delta i} & K_{xo\delta} & K_{x\delta\delta} \end{bmatrix} \begin{Bmatrix} u_{xi} \\ u_{xo} \\ u_{x\delta} \end{Bmatrix} = \begin{Bmatrix} f_{xi} \\ f_{xo} \\ f_{x\delta} \end{Bmatrix} \quad (\text{A.29})$$

Considering null the forces outside the contact

$$u_{xo} = -K_{xoo}^{-1}(K_{xoi}u_{xi} + K_{xo\delta}u_{x\delta}) \quad (\text{A.30})$$

Following the same reduction procedure of phase 3, the nodes 'o' outside the contact area are reduced and the stiffness equation becomes

$$\begin{bmatrix} K_{xii} & K_{xi\delta} \\ K_{x\delta i} & K_{x\delta\delta} \end{bmatrix} \begin{Bmatrix} u_{xi} \\ u_{x\delta} \end{Bmatrix} = \begin{Bmatrix} f_{xi} \\ f_{x\delta} \end{Bmatrix} \quad (\text{A.31})$$

Again, the values of the matrices K_{xii} and $K_{xi\delta}$ have changed with respect to the previous ones but all the passages are not reported because they are exactly the same of normal problem.

A.2.3 PHASE 5 - Stick area hypothesis

When a tangential force is applied to one of the two bodies, in some points the local tangential force $f_x(x, y)$ could reach the maximum established by the Amontons' law of friction

Appendix A (continued)

$f_x(x, y) = \mu p(x, y)$; in this case this point begins to slide.

The solution process is iterative because it is not possible to predetermine which nodes, belonging to the contact area, are in stick or in slip condition. To begin with, it is assumed that all the nodes of the potential contact area are in stick condition. In the following iterations it will not be necessary anymore to make assumptions regarding the stick/slip state, but every time the nodes with $f_x(x, y) \geq \mu p(x, y)$ will be moved from stick to slip group.

A.2.4 PHASE 6 - Nodes in slip condition reduction

It is now interesting to investigate more carefully what happens inside the contact area so only the first equation of the previous system is considered

$$K_{xii}u_{xi} + K_{xi\delta}u_{x\delta} = f_{xi} \quad (\text{A.32})$$

The nodes 'i' inside the contact area are further parted in 's' slip and 'a' adhesion nodes (the term adhesion is used in place of stick to avoid the use of the same subscript)

$$\begin{bmatrix} K_{xaa} & K_{xas} \\ K_{xsa} & K_{xss} \end{bmatrix} \begin{Bmatrix} u_{xa} \\ u_{xs} \end{Bmatrix} + \begin{bmatrix} K_{x\delta a} \\ K_{x\delta s} \end{bmatrix} u_{x\delta} = \begin{Bmatrix} f_{xa} \\ f_{xs} \end{Bmatrix} \quad (\text{A.33})$$

Considering the Amontons' law, $f_x(x, y) = \mu p(x, y)$, the second expression becomes

$$u_{xs} = K_{xss}^{-1}(\mu f_{xs} - K_{xsa}u_{xa} - K_{x\delta s}u_{x\delta}) \quad (\text{A.34})$$

Appendix A (continued)

Using this expression of u_{xs} in the first equation, it gives

$$K_{xa}u_{xa} + K_{x\delta}u_{x\delta} = f_{xa} \quad (\text{A.35})$$

with

$$\begin{cases} K_{xa} = K_{xaa} - K_{xas}K_{xss}^{-1}K_{xsa} \\ K_{x\delta} = K_{x\delta a} - K_{xas}K_{xss}^{-1}K_{x\delta s} \\ f_{xa} = f_{xia} - \mu K_{xas}K_{xss}^{-1}f_{zs} \end{cases} \quad (\text{A.36})$$

A.2.5 PHASE 7 - Tangential displacements

The *Equilibrium Equation* is essential to compute the tangential displacements of each node

$$f_{xa1} + f_{xa2} = 0 \quad (\text{A.37})$$

with

$$\begin{cases} f_{xa1} = K_{xa1}u_{xa1} + K_{x\delta 1}u_{x\delta 1} \\ f_{xa2} = K_{xa2}u_{xa2} + K_{x\delta 2}u_{x\delta 2} \end{cases} \quad (\text{A.38})$$

it becomes

$$K_{xa1}u_{xa1} + K_{x\delta 1}u_{x\delta 1} + K_{xa2}u_{xa2} + K_{x\delta 2}u_{x\delta 2} = 0 \quad (\text{A.39})$$

For couples of nodes in stick condition $u_{xa1} = u_{xa2}$ so it is possible to get the expression to calculate u_{xa1}

$$(K_{xa1} + K_{xa2})u_{xa1} + K_{x\delta 1}u_{x\delta 1} + K_{x\delta 2}u_{x\delta 2} = 0 \quad (\text{A.40})$$

Appendix A (continued)

A.2.6 PHASE 8 - Tangential forces and stick area modification

Given the tangential displacements, the tangential forces can be computed

$$f_{xa1} = K_{xa1}u_{xa1} + K_{x\delta1}u_{x\delta1} \quad (\text{A.41})$$

If there are any nodes where the tangential force is $f_x(x, y) \geq \mu p(x, y)$, these nodes are shifted in group of nodes in slip condition and the procedure is repeated, starting from PHASE 5, until convergence.

Appendix B

A MATLAB PROGRAM FOR CONTACT PROBLEMS: VALIDATION WITH 3D SPHERE CASE

The procedure that was described in Appendix A is implemented in a MATLAB program that is denominated '*Contact 3D*'. The program takes as input the stiffness matrices of the bodies in contact, that are extracted from the ANSYS 'apdl' modeling environment, and it gives as output the normal and the tangential forces and displacements at the contact surface of the two bodies.

The most interesting result is the curve that represents the correlation between the rigid tangential displacements applied to one of the two bodies and the friction forces that are generated; this curve is called '*virgin loading curve*' and it is essential to create the frictional hysteresis loop following Masing's rule [36] [27]. The area of this loop is proportional to the energy that is dissipated with the relative movement of the two bodies.

First of all, it is necessary to compare the results obtained against the analytical solutions proposed in the literature in order to validate the program reliability; for this purpose, the case of the sphere was selected to perform the analysis because Hertz and Mindlin solutions are available.

Appendix B (continued)

B.1 Bodies design and mesh generation

In order to simulate the contact, two bodies are required. In the following analysis it is used half of a sphere and a plane. ANSYS apdl commercial software is used to build the models and to create the mesh. The code developed in ANSYS language is parametrized using as inputs the half sphere radius and the contact area dimensions. The following values were selected:

- $SR = 10,000 \mu\text{m}$ Sphere radius
- $CAL = 600 \mu\text{m}$ Contact Area Length

The main objective of this part is to create a perfect coincidence between the position in the X-Y Cartesian plane of the contact area nodes of the half sphere and of the plane. Two solutions were implemented but only one respected the initial objective and consequently it was adopted for all the subsequent models.

B.1.1 Volume cutting technique

Using this technique, the two bodies are modeled using the same dimensions but their mesh are not linked to each other. In order to obtain a correspondence in the position in the X-Y Cartesian plane of the contact area nodes of the half sphere and of the plane, a cut is performed in both bodies volumes in order to isolate the contact area. It is then meshed using MESH200 element type and 'mapped' meshing method in order to obtain regular square elements. Afterwards, the volumes are meshed using SOLID185 element type. This solution does not allow the perfect coincidence in the position of contact area nodes in X-Y plane because the sphere surface is not planar.

Appendix B (continued)

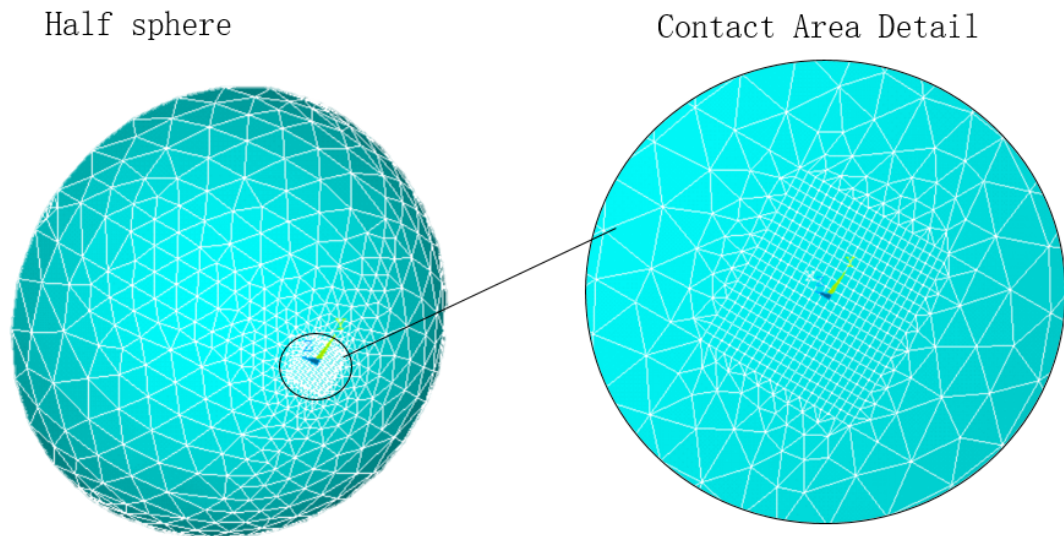


Figure 61: Half sphere model: volume cutting technique.

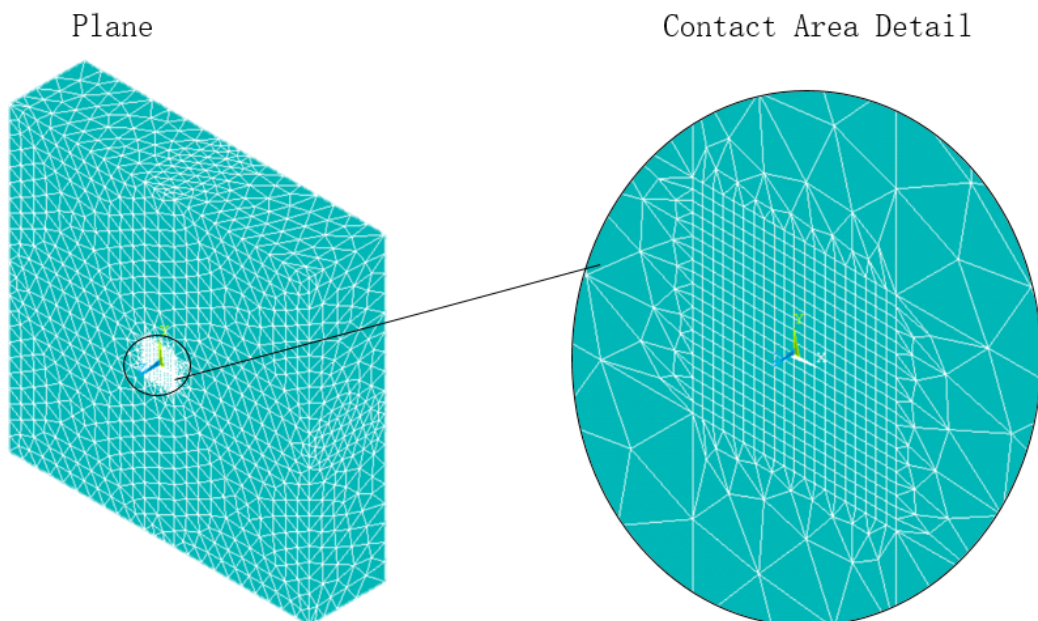


Figure 62: Plane model: volume cutting technique.

Appendix B (continued)

B.1.2 Hard points projection technique

Using this technique, the first body is modeled and the mesh is generated according to the design requirements (number of nodes / elements in the contact area). Then, the second body is built using the same dimensions of the first body but this time the mesh is created projecting the contact area nodes of the mesh of the first body. This projection is possible thanks to the use of hard points that are keypoints that can be linked to a surface. Again, MESH200 element type is used to mesh the contact surface and SOLID185 for the volume.

This solution allows a perfect coincidence in the position of the contact area nodes of the sphere and of the plane in the X-Y Cartesian plane and it does not have any limitations in model size or number of nodes in the mesh. But hard points can not be projected on any border.

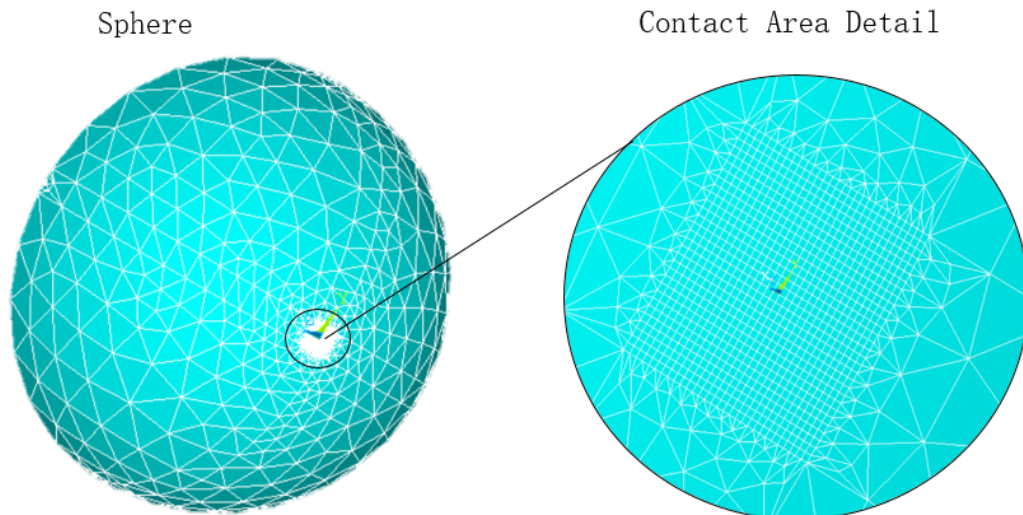


Figure 63: Half sphere model: hard points projection technique.

Appendix B (continued)

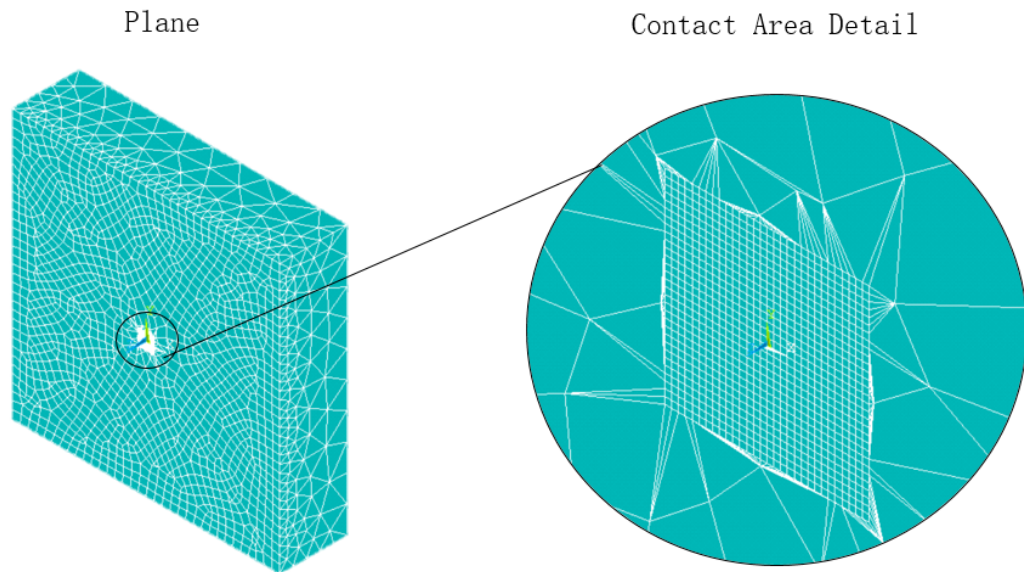


Figure 64: Plane model: hard points projection technique.

B.2 Normal contact problem: analytical vs numerical solutions

The analytical solution for the normal contact problem is provided by Hertz theory that was developed in 1881.

The results are presented in two parts: in the first part, it is illustrated what happens at the contact when two different normal forces are applied; in the second part it is presented the behavior of the system for several loading conditions.

B.2.1 Hertz contact model

The theory Hertz developed for two elastic bodies in contact is the most used and widely accepted, even if it was developed more than one hundred years ago[13]. He used Boussinesq solution of the elastic halfspace loaded by a concentrated force [37] and his observation of

Appendix B (continued)

elliptical Newtons rings formed placing a glass sphere upon a lens[38].

The condition of the contact he analyzed are

- Geometrical:
 - the contact point of the two surfaces is non singular (it must be regular at least at the second derivative)
 - the two bodies in contact have a common tangent plane (their first derivative exists)
- Material
 - elastic, isotropic
 - no friction
- Hypothesis
 - small contact surface (length and width small compared to curvature radii of bodies in contact)

The results he obtained for sphere on sphere contact are now summarized.

Contact Area

$$a = \sqrt[3]{\frac{3}{2} \frac{F}{2(\alpha_x + \alpha_y + \beta_x + \beta_y)} \left(\frac{1 - \nu_1^2}{E_1} + \frac{1 - \nu_2^2}{E_2} \right)} \quad (\text{B.1})$$

where

- a is the contact area radius
- F is the force that compress the bodies one against the other

Appendix B (continued)

- E_1 and E_2 are the elasticities of the two bodies
- ν_1 and ν_2 are the Poisson's coefficients of the two bodies
- $\alpha_x = \alpha_y = \frac{1}{2R_1}$ $\beta_x = \beta_y = \frac{1}{2R_2}$ represents the curvatures of the two spheres (R_1 and R_2 are spheres radii)

Pressure distribution

$$p = \frac{3}{2} \frac{F}{\pi a^2} \sqrt{1 - \frac{X^2}{a^2} - \frac{Y^2}{a^2}} \quad X, Y \leq a \quad (\text{B.2})$$

with

$$p_{mean} = \frac{F}{\pi a^2} \quad (\text{B.3})$$

$$p_{max} = \frac{3}{2} \frac{F}{\pi a^2} \quad (\text{B.4})$$

Normal approach

$$\delta = (\alpha_x + \alpha_y + \beta_x + \beta_y) \left(\sqrt[3]{\frac{3}{2} \frac{F}{2(\alpha_x + \alpha_y + \beta_x + \beta_y)} \left(\frac{1 - \nu_1^2}{E_1} + \frac{1 - \nu_2^2}{E_2} \right)} \right)^2 \quad (\text{B.5})$$

B.2.2 Specific cases: low and high normal force

At this point, it is possible to compare the analytical and the numerical solution. In order to confirm the software is working properly, two different cases are considered, one with high NF and one with low NF; the higher force generates a pressure with maximum value close but below 2000N that represents a high value for yield strength in tempered steels [39]. The same values of normal forces are used for the tangential problem.

The components material is steel. In the tables below, some steel properties are illustrated [40].

Appendix B (continued)

TABLE VI: STEEL POISSON'S RATIOS

Steel	Poisson's ratio $-\nu-$
Stainless Steel 18-8	0.305
Steel, Mild	0.302
Steel, Cast	0.265
Steel, Cold-rolled	0.287
Steel, High Carbon	0.295

TABLE VII: STEEL YOUNG'S MODULI

Steel	Young's modulus $-E-$
Stainless Steel 302	180 GPa
Stainless Steel 303	193 GPa
Stainless Steel 304	190 GPa
Steel EN1A	210 GPa
Steel ASTM-A36	200 GPa

Some of this information were extracted from "*Engineeringtoolbox.com*" website [41].

Since the simulations performed do not refer to a specific type of steel, average values are selected:

- $\nu_1 = \nu_2 = 0.3$
- $E_1 = E_2 = 200GPa$

B.2.2.1 Low Normal Force

The selected LNF is 50 N. This should be the less accurate of the two simulations because the nodes involved in the contact, belonging to the contact area, are fewer.

Appendix B (continued)

Contact area

In Figure 65 the contact area obtained with hertz theory is represented with yellow shading, instead the red squares represent the nodes inside the CA and the blue asterisks the nodes outside the CA. The results are perfectly coincident and if there are few blue asterisks inside the contact area is due to numerical errors (the mesh is not dense enough).

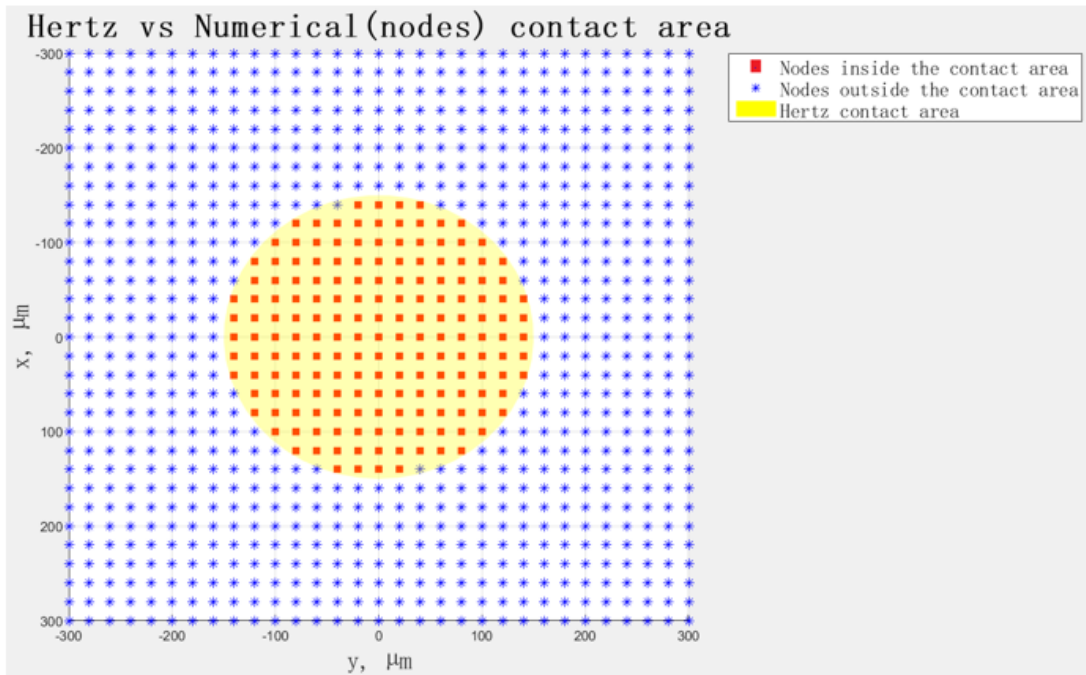


Figure 65: Contact area comparison: sphere LNF.

Normal pressure distribution

In the following figures, the results for pressure distributions are presented.

Appendix B (continued)

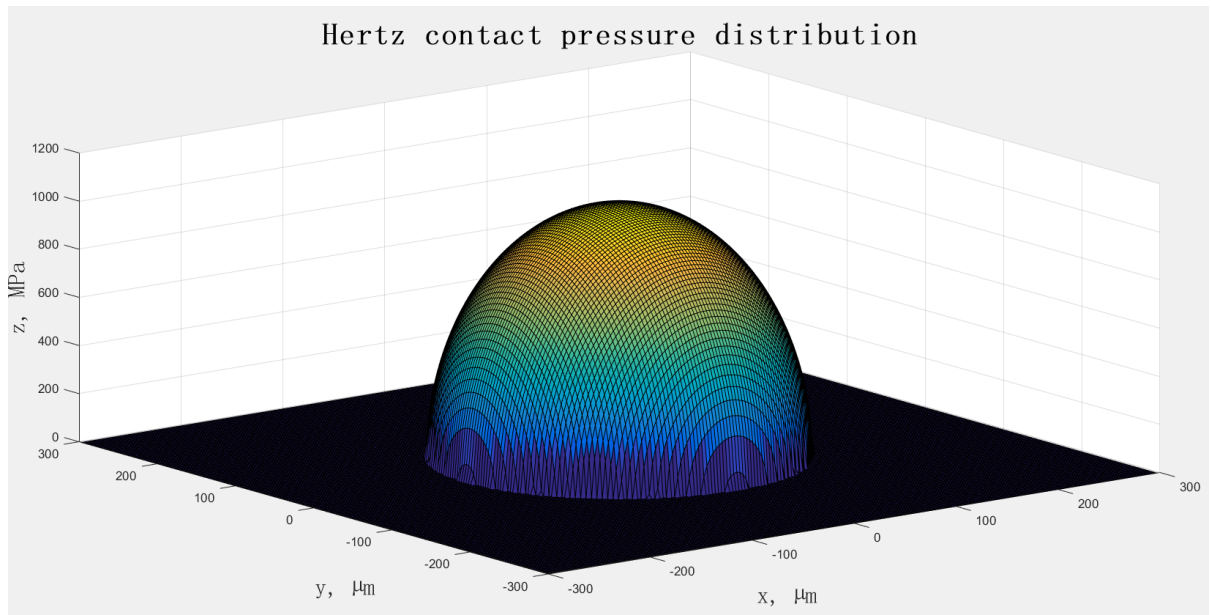


Figure 66: Hertz pressure distribution: sphere LNF.

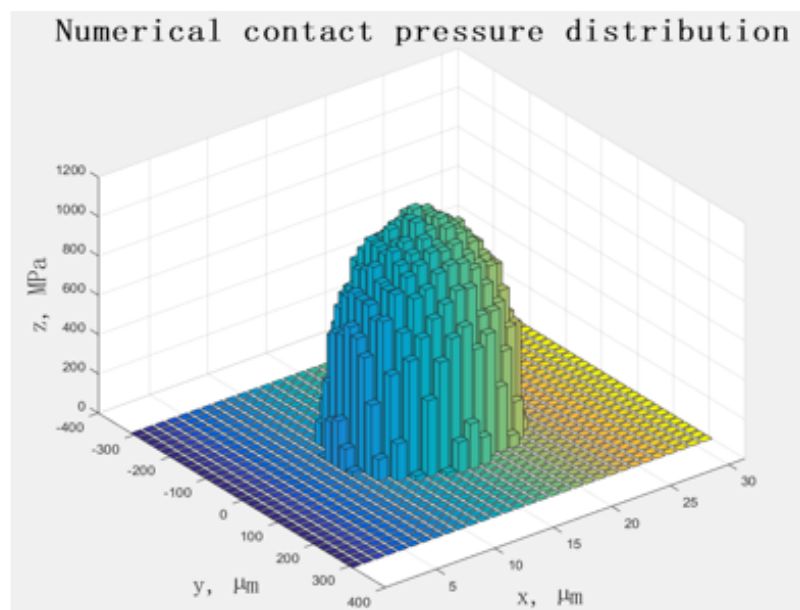
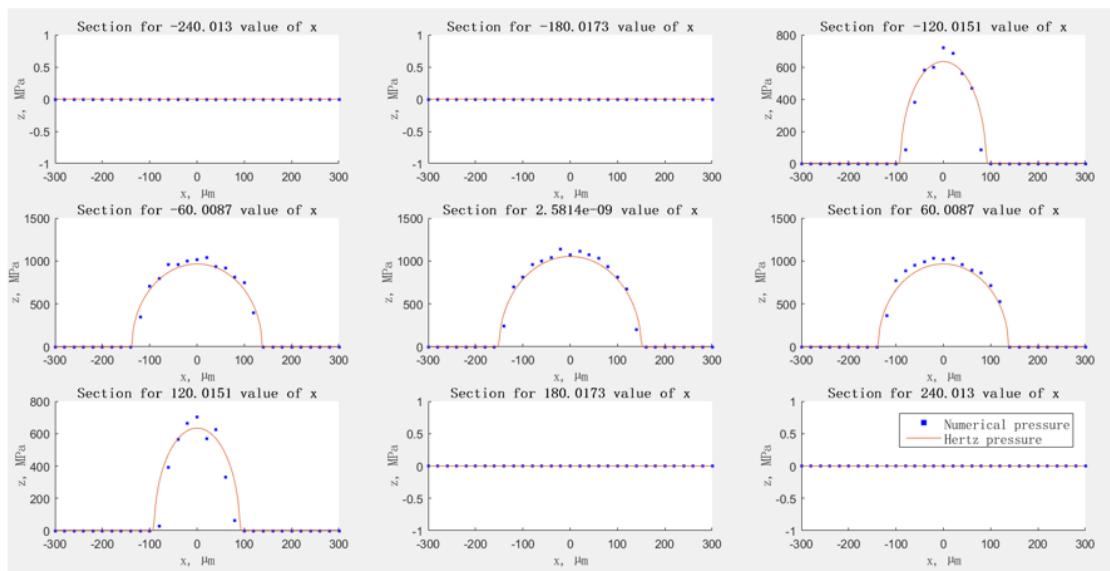
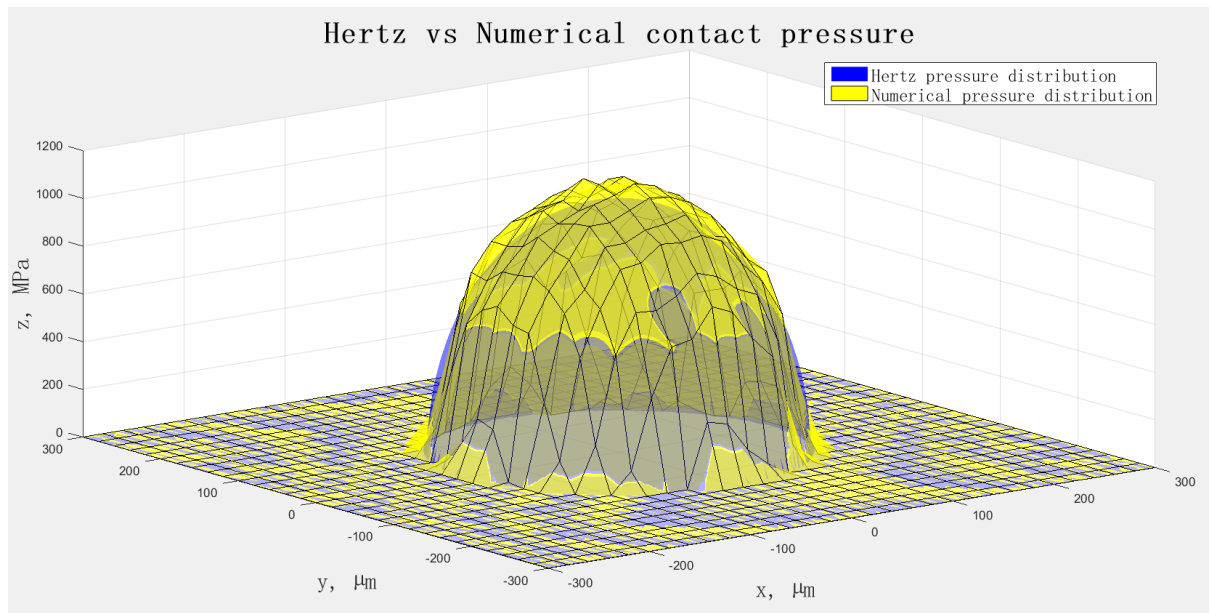


Figure 67: Numerical pressure distribution: sphere LNF.

Appendix B (continued)



Appendix B (continued)

The numerical and the analytical solutions are very close. Their shape is similar (both of them have a peak in the middle of the sphere and the pressure gradually decrease getting closer to the border) and the point by point values have an acceptable difference.

B.2.2.2 High Normal Force

The selected HNF is 200 N. The same results obtained for LNF are presented for high normal force. They should be more accurate than LNF because more nodes are involved in the contact.

Contact area

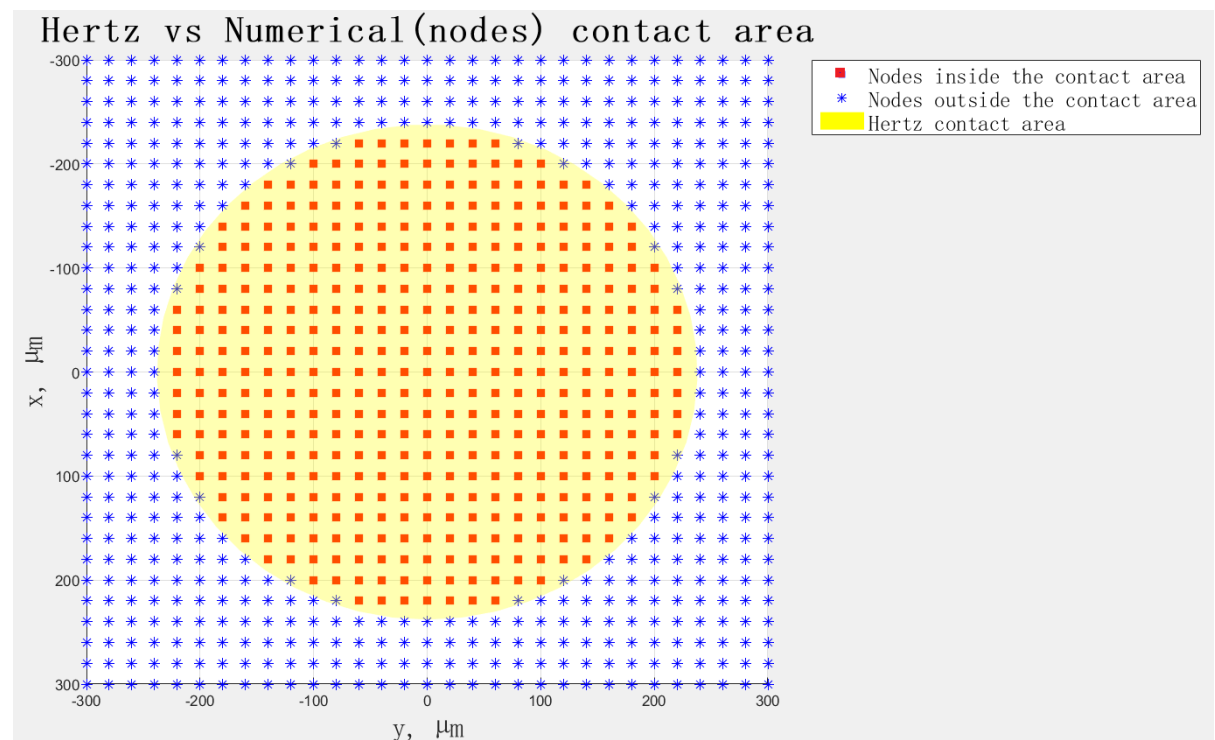


Figure 70: Contact area comparison: sphere HNF.

Appendix B (continued)

The contact area is wider, but the two solutions are still coincident.

Normal pressure distribution

Again, the numerical and the analytical solutions are coincident. The maximum pressure has increased as expected because normal force is higher, but the shape of the pressure distribution is the same. The numerical pressure seems to be slightly higher than Hertz pressure.

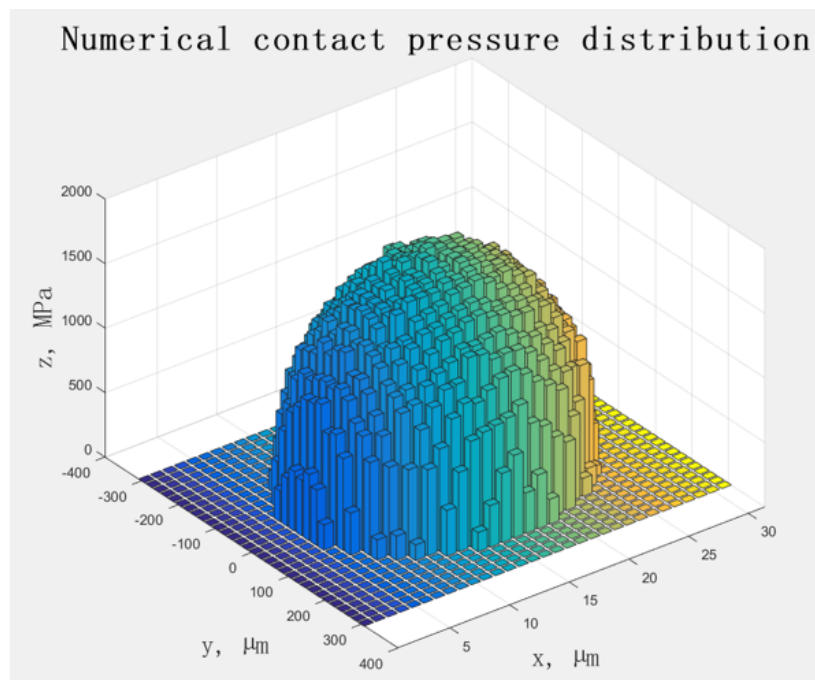


Figure 71: Numerical pressure distribution: sphere HNF.

Appendix B (continued)

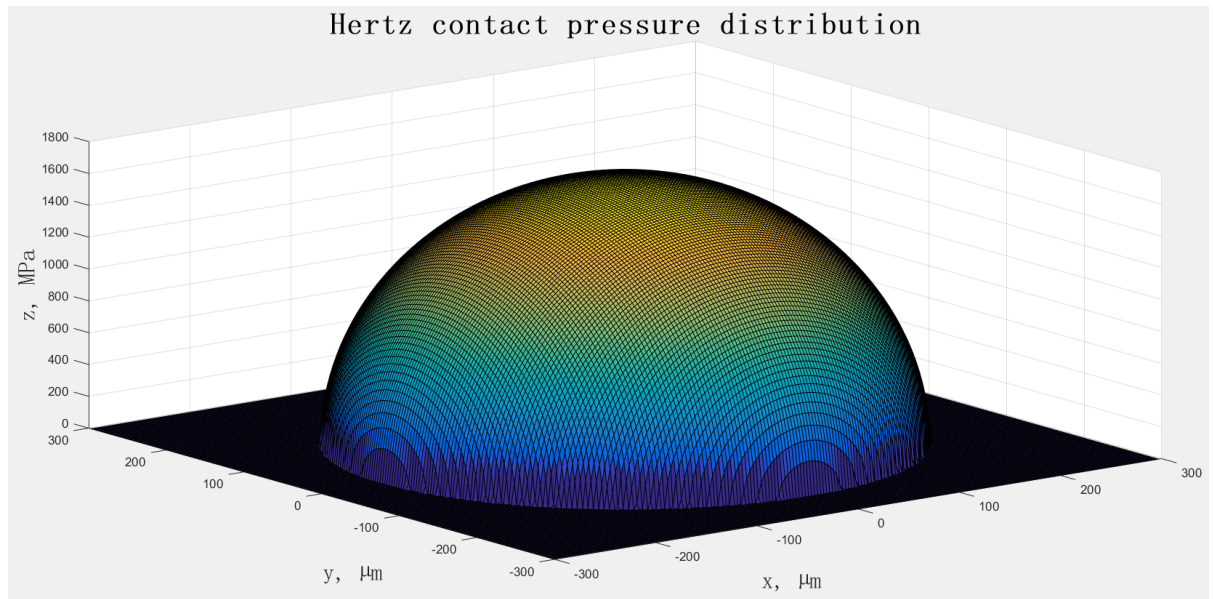


Figure 72: Hertz pressure distribution: sphere HNF.

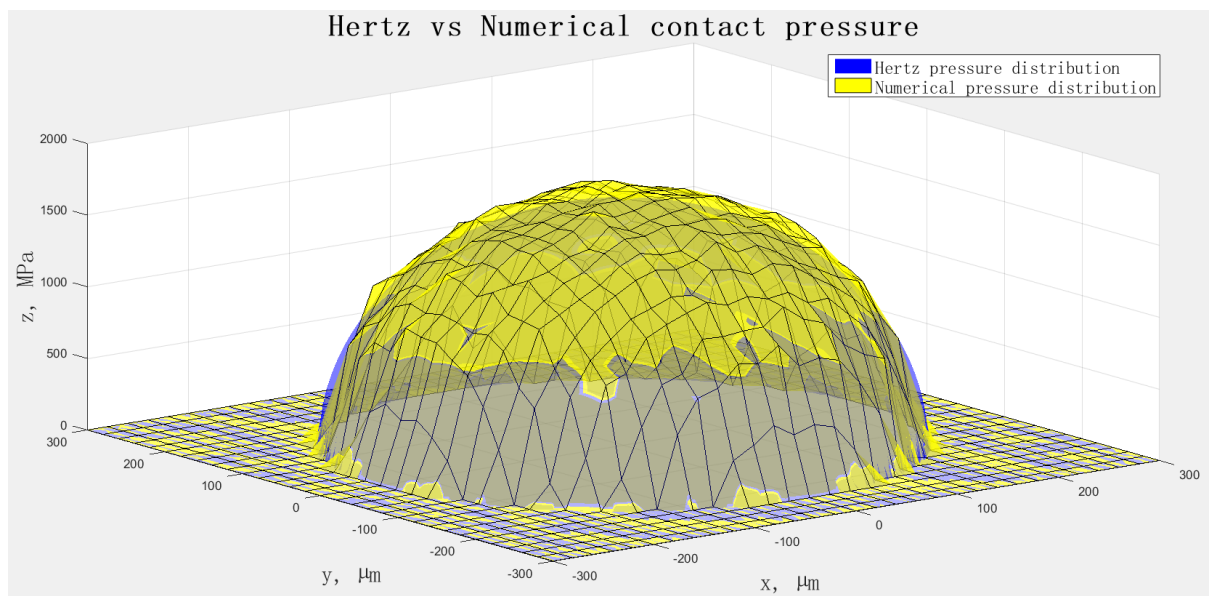


Figure 73: Pressure distribution 3D: sphere HNF.

Appendix B (continued)

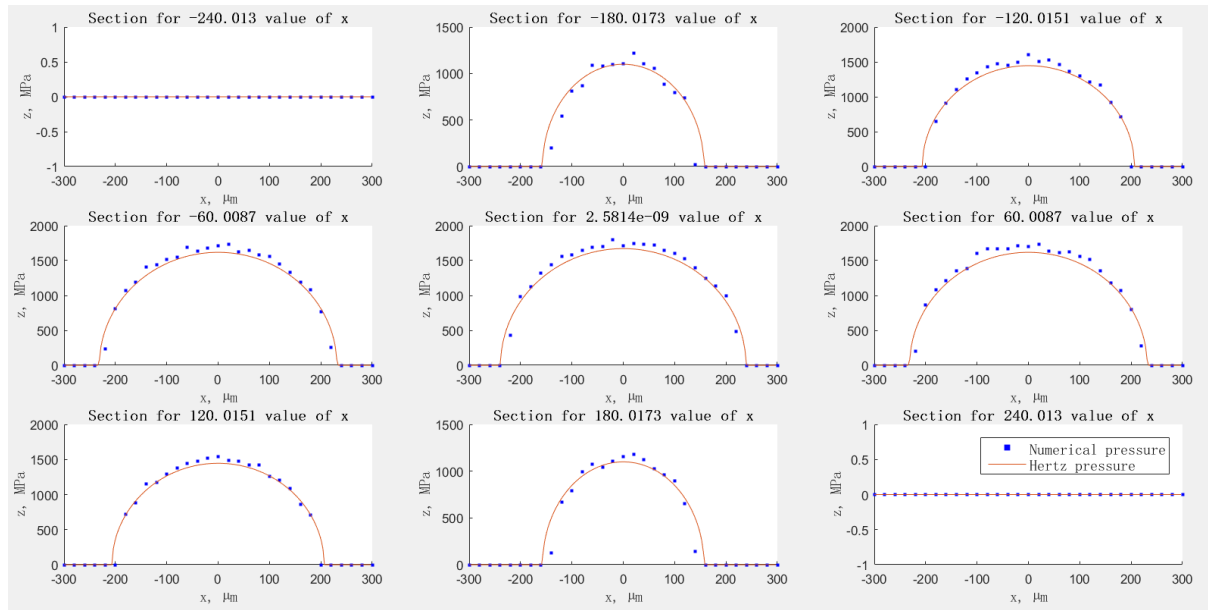


Figure 74: Pressure distribution 2D: sphere HNF.

B.2.3 System behavior for several loading conditions

For a broader prospective on program capabilities, the results of several simulations in a NF range of 0-450 N are presented. In the following figures, two trends are displaced for numerical solution. The purpose is to investigate what boundary conditions are more suitable for nodes outside contact area: in the vertical direction the displacements are imposed (they represent the input of the problem), in x and y directions the nodes can be fixed or flexible (Figure 75). The BCs should not influence the solution, because the 'distant' nodes are very far from the contact area; but the flexible alternative is the closest to the reality because the sphere could be deformed in the loading process.

Appendix B (continued)

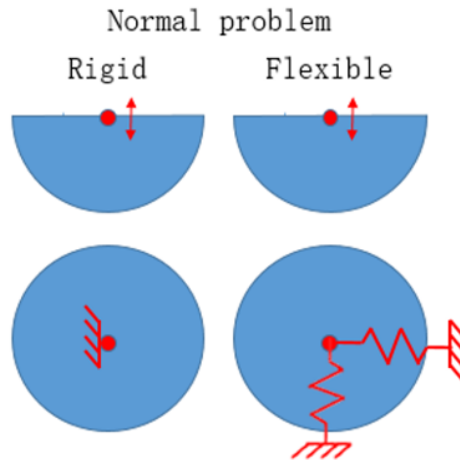


Figure 75: Boundary conditions: normal problem.

Dz vs normal force

In Figure 76, it is represented the behavior of NF for different vertical displacements 'dz'. As expected, the BCs have no influence and all the solutions are coincident.

Contact area vs normal force

In Figure 77, it is possible to see what happens to the contact area for different loading conditions. The CA of Hertz solution is slightly higher than the numerical one and the gap between the two solutions increases when the NF is higher; but the radius has not the same trend and that is because the error is associated to the shape of the contact area, which is a circle and it is approximated with a sum of squares.

Max and mean pressure vs normal force

In Figure 78, the trends for the pressure are shown. They are correct and the small error is a consequence of the difference in contact area.

Appendix B (continued)

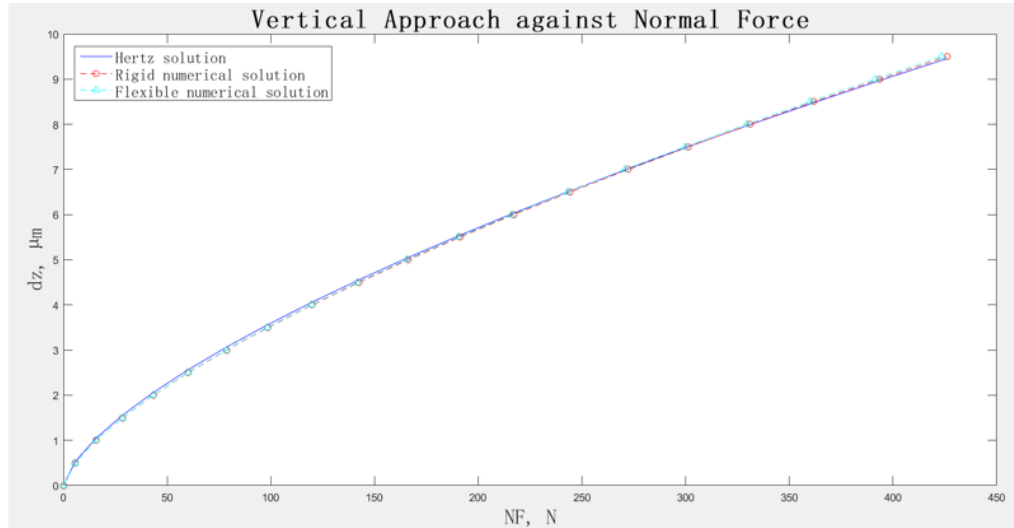


Figure 76: Dz vs normal force: sphere.

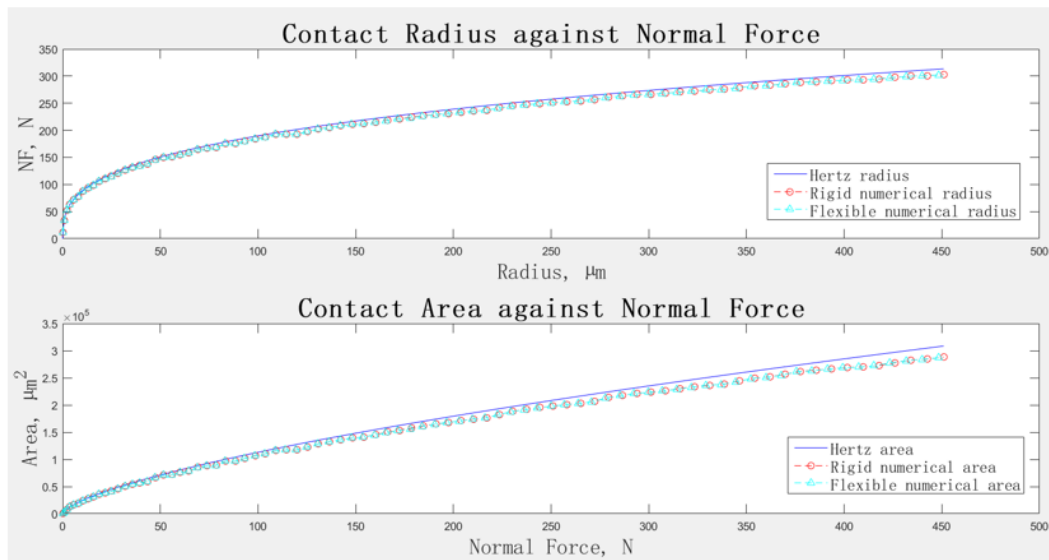


Figure 77: Contact area vs normal force: sphere.

Appendix B (continued)

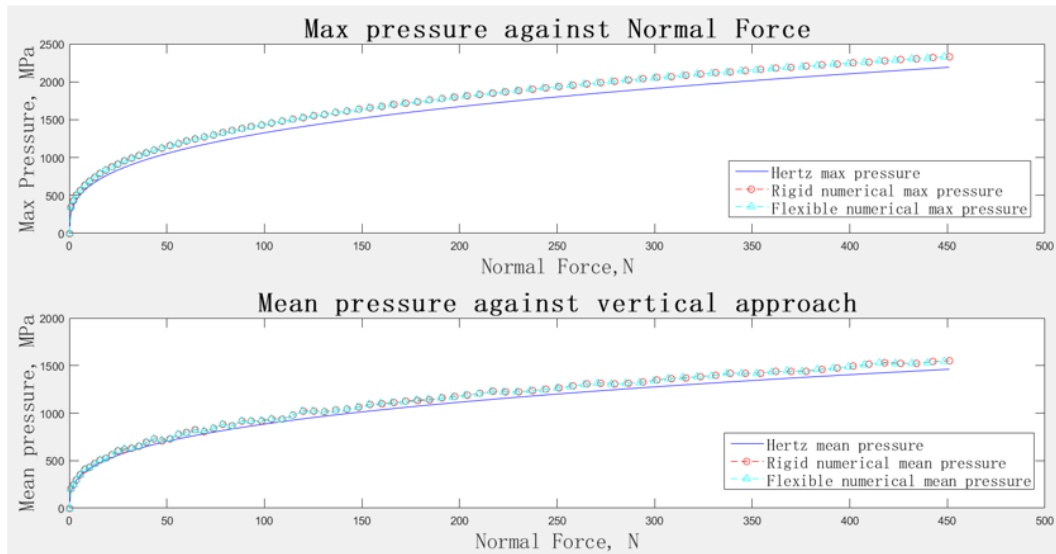


Figure 78: Max and mean pressure vs normal force: sphere.

B.3 Tangential problem: analytical vs numerical solutions

It was Mindlin, in 1953, who first solved the problem of two bodies in contact loaded with a tangential force [14].

The results are organized in two sections: in the first section, starting from the solution of HNF, two different tangential displacements are used for the simulation, one that marks the division between adhesion and contact area and one that leads the body close to sliding condition; in the second section, the trends of several tangential displacements are displayed.

B.3.1 Mindlin model for spheres in contact under tangential force

Mindlin conducted many studies regarding elastic bodies in contact [14] [15] [16] and he developed a model to predict the tangential stress distribution when a tangential force is applied.

Appendix B (continued)

His theory starts from Hertz model and it is based on the following assumptions:

- the contact happens between two identical spheres;
- the contact area and the normal pressure distribution caused by the normal force (Hertz results) do not change when the tangential force is applied;
- there is no relative velocity between the two bodies in contact, the slip occurs at the contact interface;
- there is a "rigid body" tangential displacement at the contact surface;
- the shear stress distribution τ is parallel to the displacement on every point of the contact surface and it is axially symmetric in magnitude;
- the tangential stress on the annulus of slip has the same direction of the tangential loading and magnitude of $\tau = \mu p$, with p normal pressure and μ friction coefficient.

The results he obtained are presented.

Stick area radius

$$c = a \sqrt[3]{1 - \frac{T}{\mu N}} \quad (\text{B.6})$$

where

- c is the radius of the stick area
- a is the contact area radius, calculated with Hertz formula
- T is the tangential force
- N is the normal force

Appendix B (continued)

- μ is the friction coefficient

Tangential traction distribution

$$\left\{ \begin{array}{ll} \tau = \frac{3\mu N}{2\pi a^3} \sqrt{a^2 - \rho^2} & \text{with } c \leq \rho \leq a \\ \tau = \frac{3\mu N}{2\pi a^3} \left[\sqrt{a^2 - \rho^2} - \sqrt{c^2 - \rho^2} \right] & \text{with } \rho \leq c \end{array} \right. \quad (\text{B.7})$$

Tangential displacement

$$\delta = \frac{3(2 - \nu)\mu N}{16Ga} \left[1 - \left(\frac{c}{a} \right)^2 \right] \quad (\text{B.8})$$

where

- ν is the Poisson's coefficient
- G is the shear modulus

It is important to note that the above mentioned is the displacement of distant points with respect to the uniform displacement of the adhered portion and not the absolute one.

B.3.2 Specific cases: small and large tangential displacements

In order to check if the numerical solution for the tangential contact problem is correct, it is necessary to compare it with the analytical solution of Mindlin. Two cases are taken into account that should represent two extremes, one with tangential displacement $'du' = 3\mu m$ and the other with $'du' = 5.8\mu m$. The first one should evidence a net separation between stick and slip portion of contact area, instead the second one should lead the bodies very close to the sliding condition.

Appendix B (continued)

B.3.2.1 Small tangential displacement

Stick/Slip areas

In Figure 79, the yellow shading represents the stick area of Mindlin solution and the violet shading the slip area; the red squares represents the nodes in slipping condition of numerical solution and the blue asterisks the nodes in stick. The two solutions are coincident and if there are few differences it is because the mesh is not dense enough.

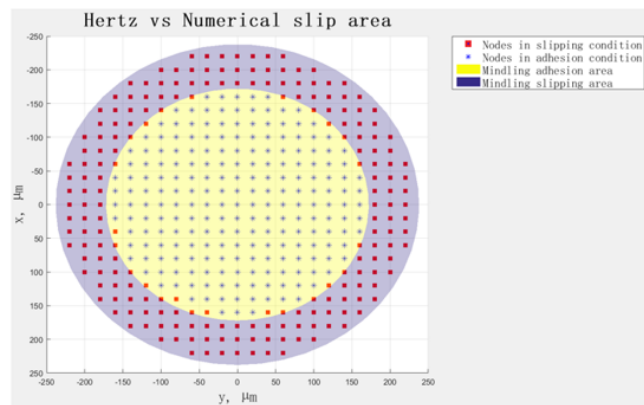


Figure 79: Stick/Slip areas: sphere STD.

Tangential traction distribution

Figure 80 reports the punctual forces generated in each node of the contact area and Figure 81 the distribution computed with Mindlin solution. The two solutions are compared in 3D in Figure 82 and in 2D in Figure 83. Their magnitude and shape are coincident.

Appendix B (continued)

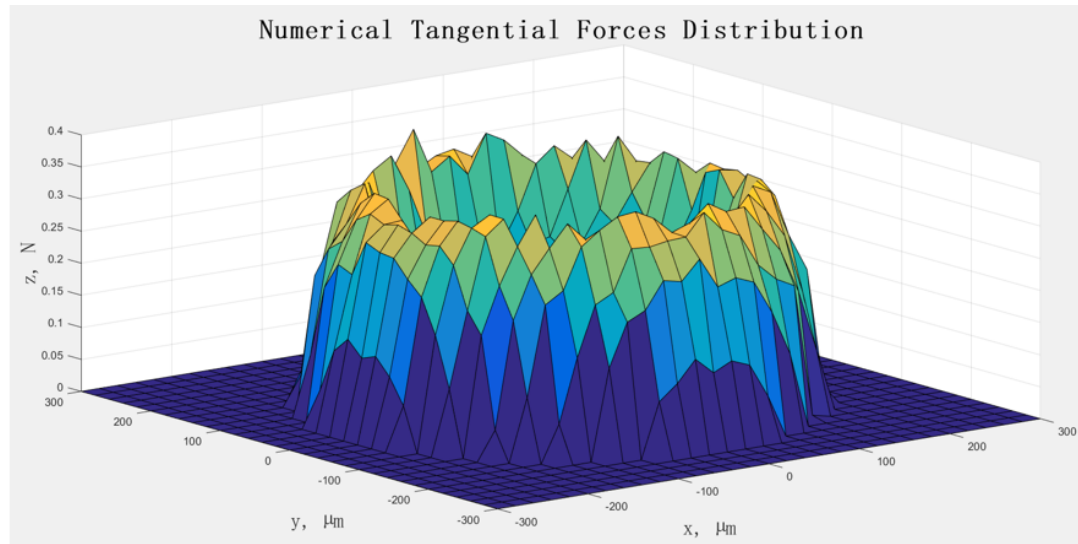


Figure 80: Numerical tangential force: sphere STD.

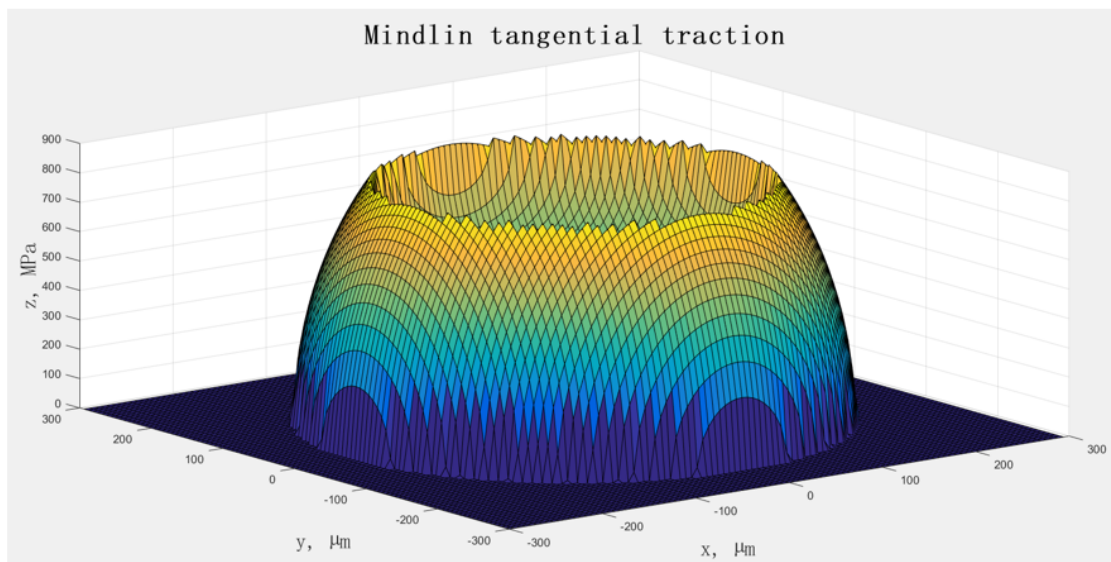


Figure 81: Mindlin tangential traction: sphere STD.

Appendix B (continued)

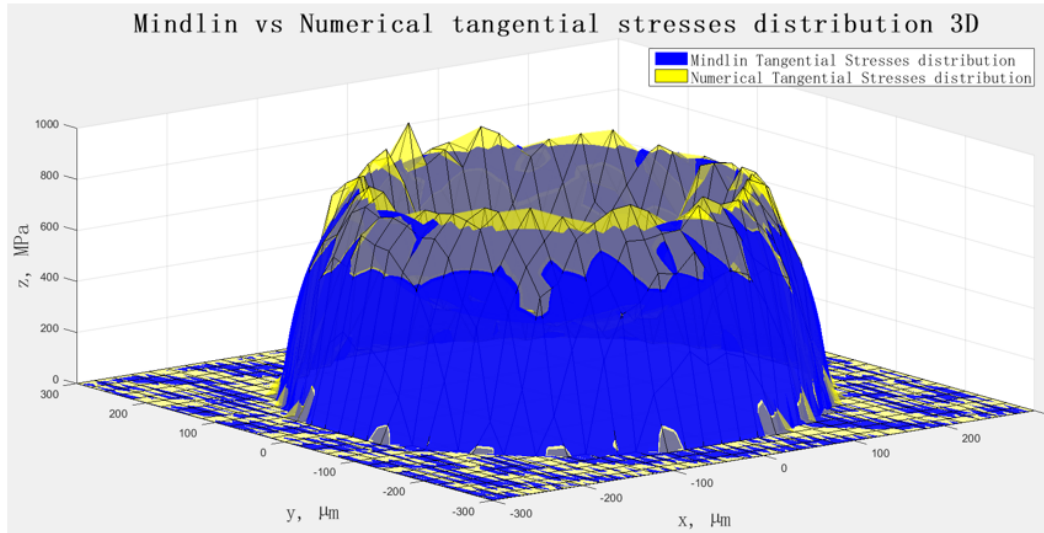


Figure 82: Tangential traction comparison 3D: sphere STD.

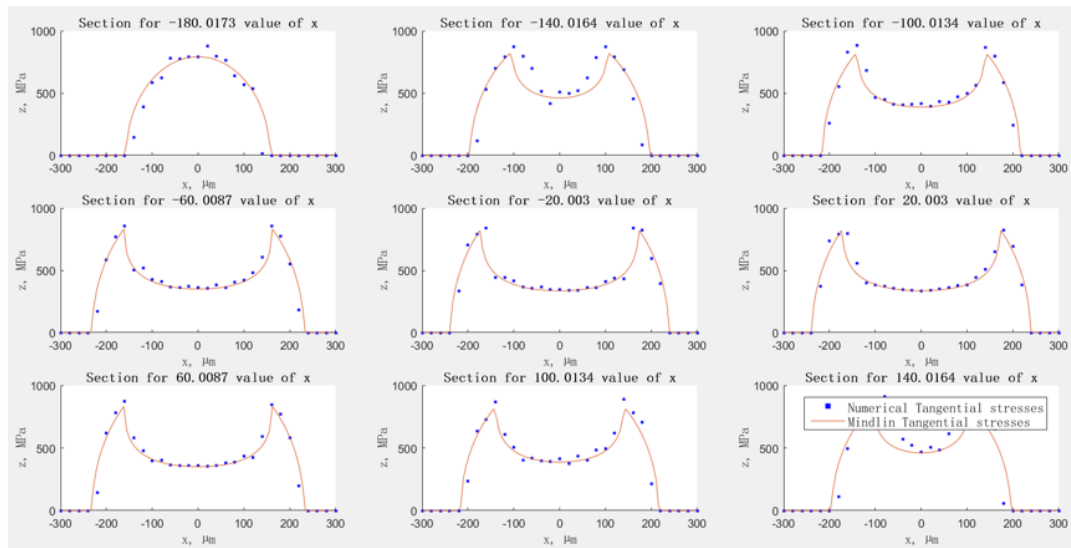


Figure 83: Tangential traction comparison 2D: sphere STD.

Appendix B (continued)

B.3.2.2 Large tangential displacement

The tangential displacement is almost doubled ($'du' = 6\mu m$ leads to the sliding condition) so the stick area should be significantly reduced and the traction distribution should have the same shape of the pressure distribution of the normal problem solution (in the slip zone the tangential stress is proportional to the pressure).

Stick/Slip areas

The system has the expected behavior and the solutions are coherent.

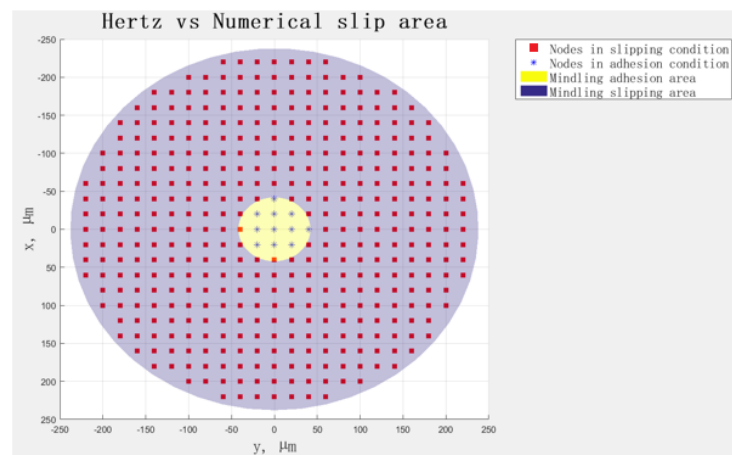


Figure 84: Stick/Slip areas: sphere LTD.

Tangential traction distribution

Figure 87 and Figure 88 confirm the program results are correct even when a large tangential displacement is imposed to one of the two bodies.

Appendix B (continued)

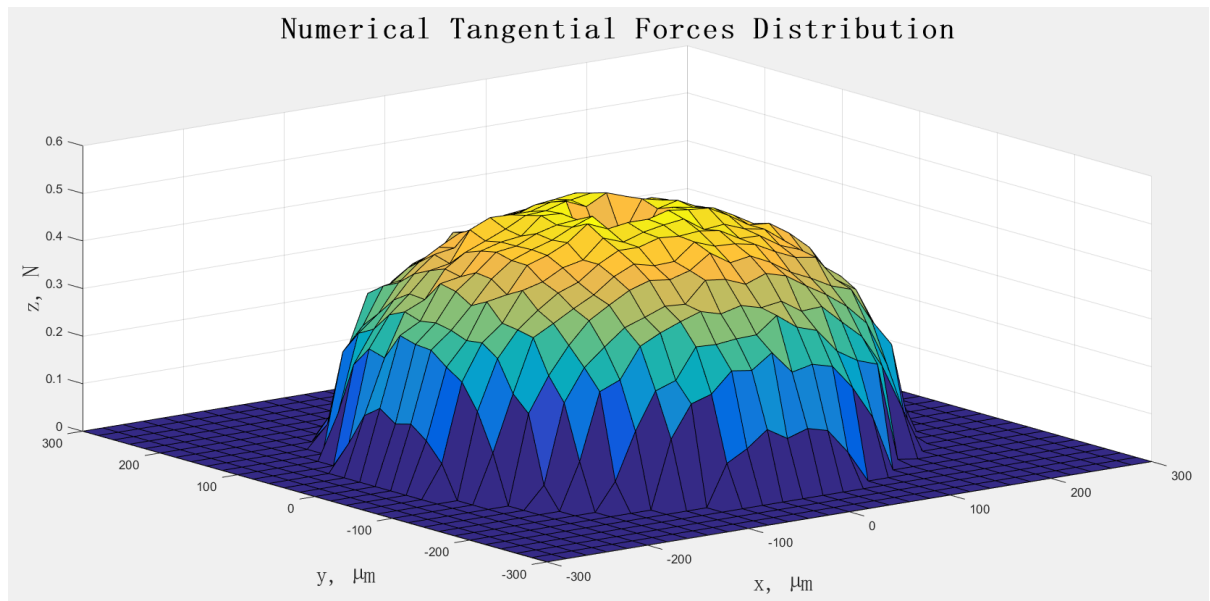


Figure 85: Numerical tangential force: sphere LTD.

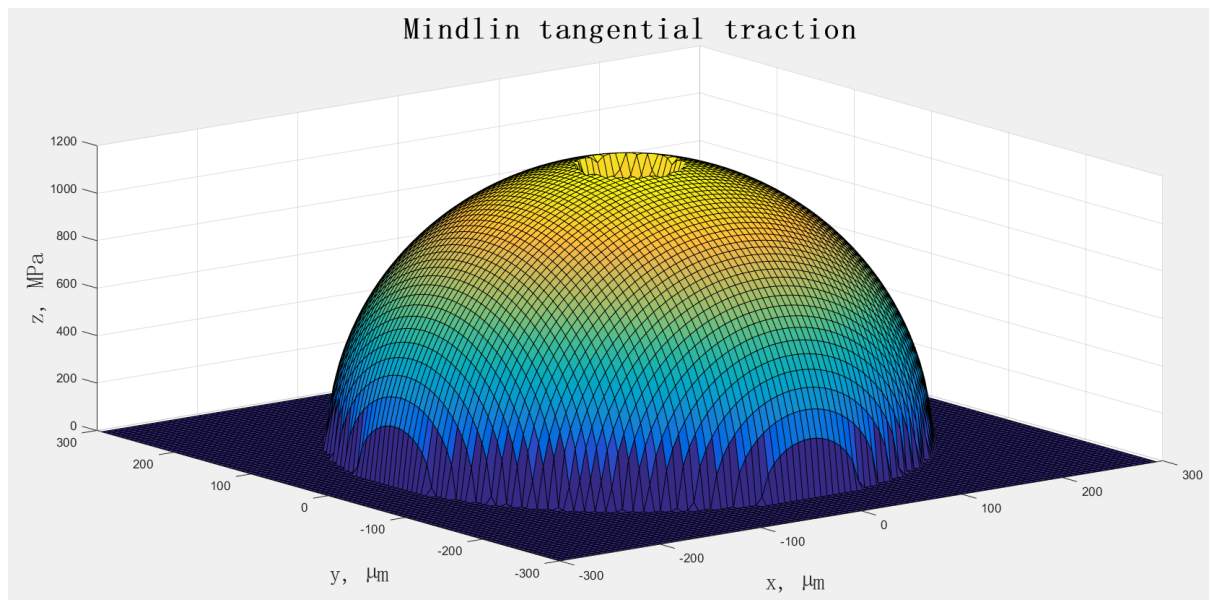


Figure 86: Mindlin tangential traction: sphere LTD.

Appendix B (continued)

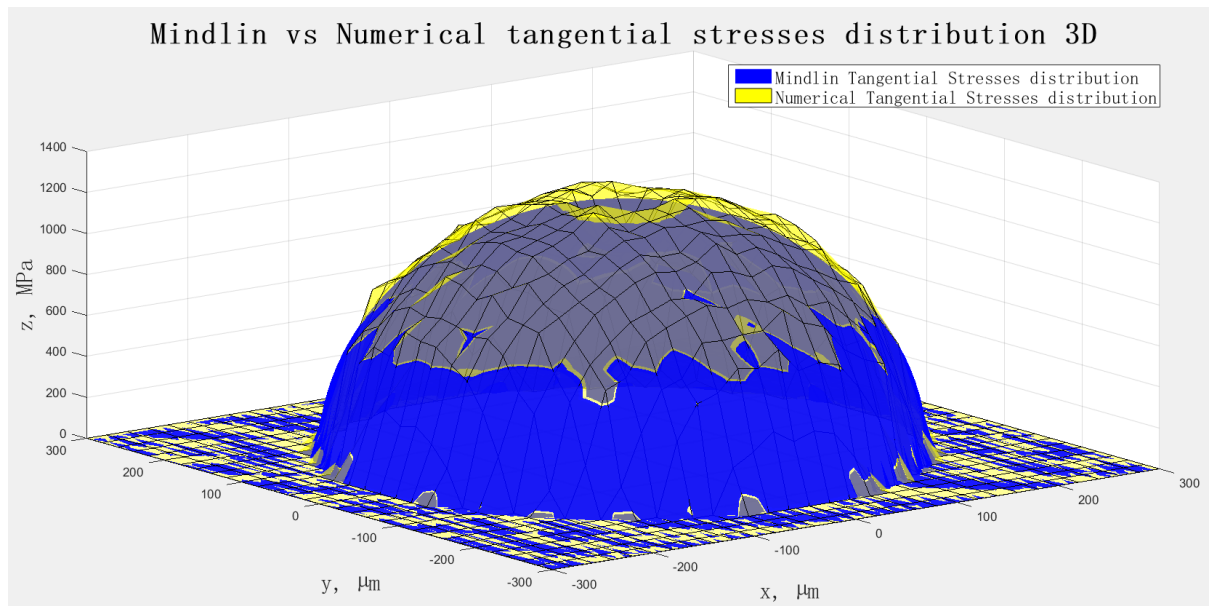


Figure 87: Tangential traction comparison 3D: sphere LTD.

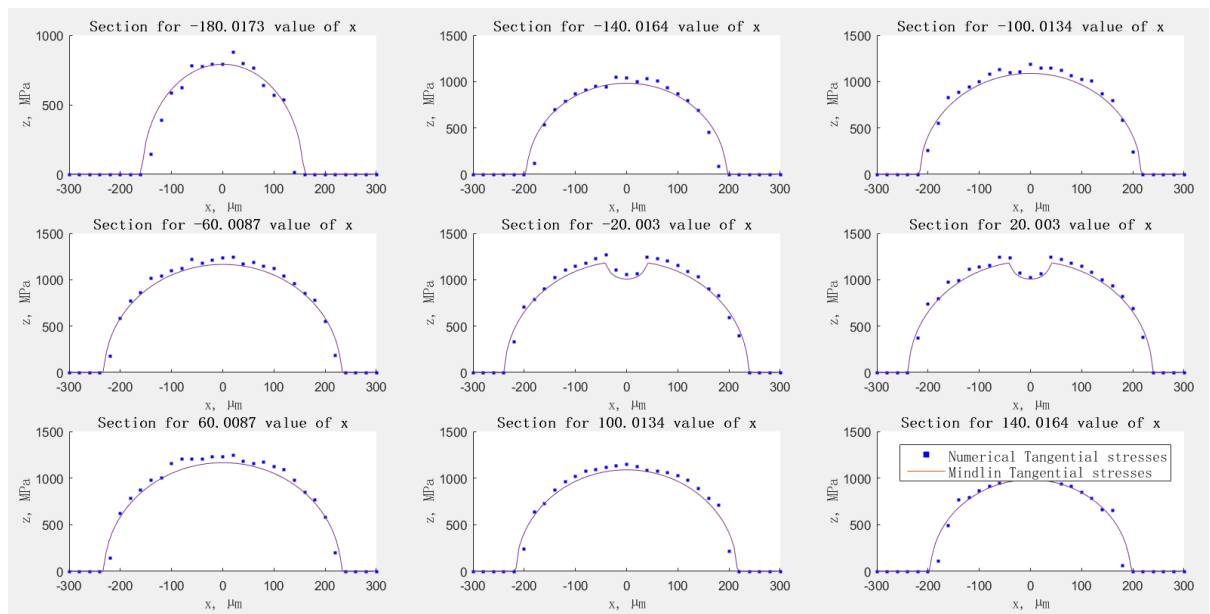


Figure 88: Tangential traction comparison 2D: sphere LTD.

Appendix B (continued)

The numerical tangential stresses are slightly higher in the center of the contact area with respect to Mindlin solution and smaller along the border. However, this do not affect the overall coherence of the program results.

Slip distribution

The last interesting result for this part concerns the slip distribution. The slip area has increased from STD to LTD and it is always zero in the center.

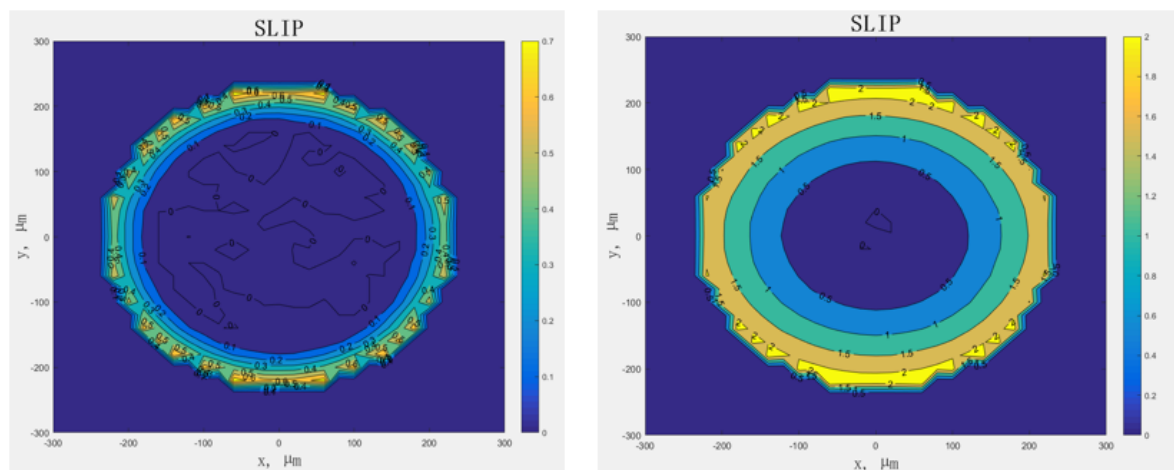


Figure 89: Slip: STD - LTD comparison.

B.3.3 System behavior for several tangential displacements

The tangential contact problem is strictly connected to the solution of the normal contact problem because the contact surface and the pressure distribution are kept constant for hy-

Appendix B (continued)

pothesis. As a consequence, $'dz' = 10\mu m$ is selected as vertical displacement to have a large range for tangential displacements before sliding condition is reached.

Even in this case, two trends are shown for numerical solution to investigate which are the best boundary conditions for 'distant' nodes (Figure 90). In the vertical direction they are fixed, in the x direction the displacements are imposed, in y direction they can be fixed or flexible. The BCs should not influence the solution at the contact.

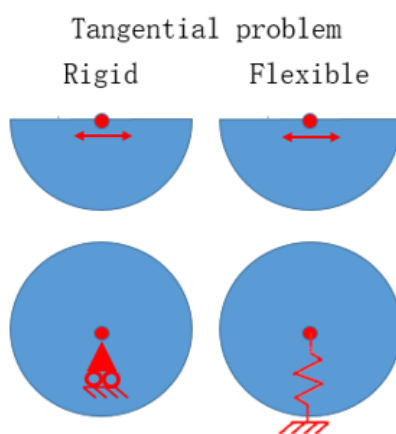


Figure 90: Boundary conditions: tangential problem.

Tangential force vs du

The numerical and the analytical solutions of Figure 76 are coincident. Even for the tangential contact problem the BCs do not affect the results. This graph is extremely important because it is the one that generates the frictional hysteresis loop. The curve presents an asymp-

Appendix B (continued)

tote, that is when the tangential force $T = \mu N$.

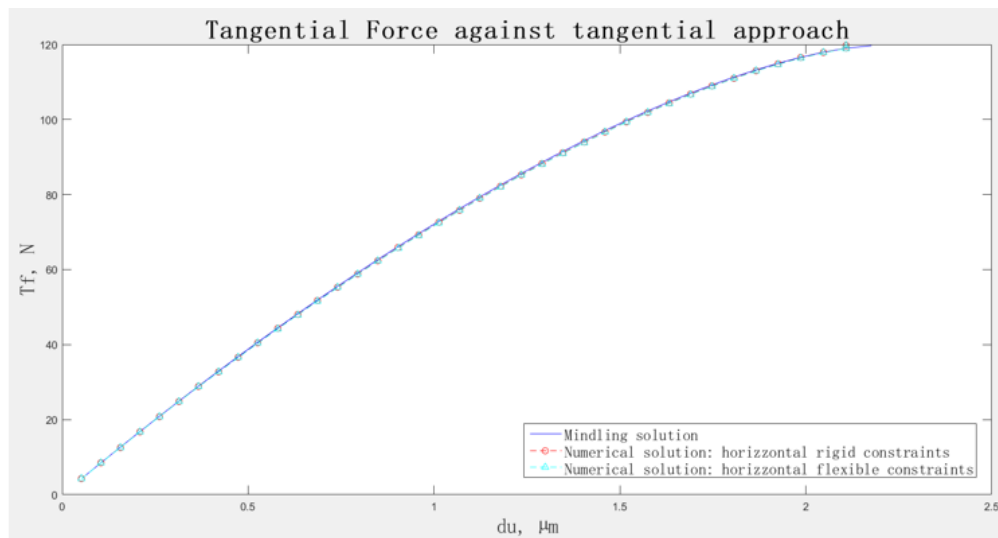
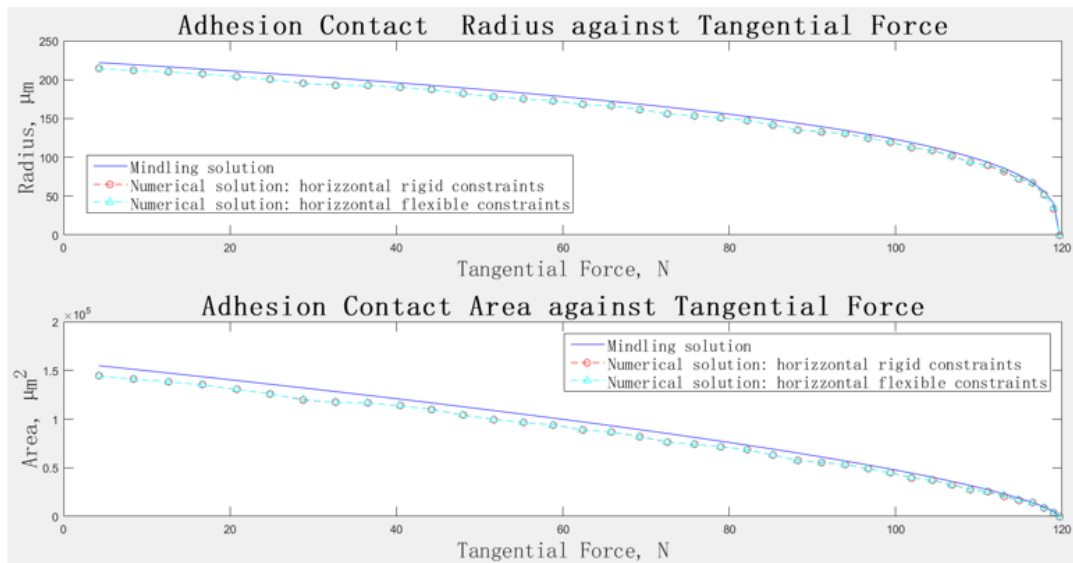


Figure 91: Tangential force vs du.

Stick area vs du

The stick area radius trend of numerical solution perfectly follows that of Mindlin model even if it is slightly smaller. The difference is higher for the entire area but it is due to the fact that a circular surface is approximated with a sum of squares: a mesh more dense, with smaller squares could approximate better the rounded shape.

Appendix B (continued)

Figure 92: Stick area vs du .**B.4** MATLAB program validation

This first chapter confirms the program can be trusted and used to simulate the contact between bodies with different shapes such as cylinders or planes. The analytical solutions are not always available for this models but the results obtained so far are so accurate that it is possible to expect errors associated only to the number and shape of finite elements that approximate the bodies.

CITED LITERATURE

1. Caughey, T. K.: Sinusoidal excitation of a system with bilinear hysteresis. American Society of Mechanical Engineers, Journal of Applied Mechanics, 27:640–643, 1960.
2. Iwan, W. D.: Application of nonlinear analysis techniques. ASME AMD, Applied Mechanics in Earthquake Engineering, 8, 1974.
3. Ewins, D. J. and Sanliturk, K. Y.: Modelling two-dimensional friction contact and its application using harmonic balance method. Journal of Sound and Vibration, 193(2):511–523, 1996.
4. Menq, C. H. and Yang, B. D.: Non linear spring resistance and friction damping of frictional constraint having two dimensional motion. Journal of Sound and Vibration, 217(1):127–143, 1998.
5. Menq, C. H., Chidamparam, P., and Griffin, J. H.: Friction damping of two dimensional motion and its application in vibration control. Journal of Sound and Vibration, 144(3):427–447, 1991.
6. Kosarev, O. I.: Application of augmented lagrangian techniques for non linear constitutive laws in contact interfaces. Communications in numerical methods in engineering, 9:815–824, 1993.
7. Ollerton, E. and Haines, D.: A dynamic lagrangian frequencytime method for the vibration of dry-friction-damped systems. Journal of sound and vibrations, 265:201–219, 2003.
8. Herzog, A. and von Scheidt Jorg Wallaschek, M. K. L. P.: Comparison of two widely-used frequency-time domain contact models for the vibration simulation of shrouded turbine blades. Proceedings of ASME Turbo Expo 2014: Turbine Technical Conference and Exposition, 2014.
9. Gola, M. and Liu, T.: A direct experimentalnumerical method for investigations of a laboratory under-platform damper behavior. International Journal of Solids and Structures, 51:42454259, 2014.

CITED LITERATURE (continued)

10. Gola, M., Liu, T., and dos Santos, M. B.: Design of a new test rig to evaluate under-platform damper performance. Proceedings of the ASME 2010 10th Biennial Conference on Engineering Systems Design and Analysis, 2010.
11. Ewins, D. J., Petrov, E., and Schwingschackl, C.: Validation of test rig measurements and prediction tools for friction interface modelling. Proceedings of ASME Turbo Expo 2010: Power for Land, Sea and Air, 2010.
12. The MathWorks, Inc.: , Natick, Massachusetts, United States MATLAB and Statistics Toolbox Release 2012b.
13. Hertz, H. R.: Uber die beruehrung fester elastischer koerper. Gesammelte Werke, 1:155–173, 1895.
14. Mindlin, R. D. and Deresiewicz, H.: Elastic spheres in contact under varying oblique forces. ASME J. Appl. Mech., 20:327–344, 1953.
15. Mindlin, R. D.: Compliance of elastic bodies in contact. ASME J. Appl. Mech., 16:259–268, 1949.
16. Mindlin, R. D., Mason, W., Osmer, I., and H.Deresiewicz: Effects of an oscillating tangential force on the contact surfaces of elastic spheres. Proceedings of the First U.S. National Congress of Appl. Mech., pages 203–208, 1952.
17. Brandlein, J.: Ball and Roller Bearings : Theory, Design, and Application. John Wiley & Sons, Ltd. (UK), 1999.
18. Harris, T. A.: Rolling Bearing Analysis. John Wiley & Sons, Ltd. (UK), 1991.
19. Kosarev, O. I.: Contact deformation and compression of cylinders. Russian Engineering Research, 31(2):27–31, 2011.
20. Norden, B. N.: On the compression of a cylinder in contact with a plane surface. National Bureau of Standards, 1973.
21. Young, W. C. and Budynas, R. G.: Roarks Formulas for Stress and Strain. McGraw-Hill, 2002.
22. Johnson, K. L.: Contact Mechanics. 40 West 20th street, New York, Cambridge University Press, 2003.

CITED LITERATURE (continued)

23. ANSYS, Inc.: , Canonsburg, Pennsylvania, United States ANSYS Mechanical APDL 16.0.
24. Dinnik, A. N.: Impact and compression of elastic bodies. Izobrannye trudy, Izd. AN UkrSSR, 1:13–114, 1952.
25. The MathWorks, Inc.: Optimization Toolbox User's Guide, 2003. Version 2.
26. Branch, M. A., Coleman, T. F., and Li, Y.: A subspace, interior and conjugate gradient method for large-scale bound-constrained minimization problems. SIAM Journal on Scientific Computing, 21(1):1–23, 1999.
27. Masing, G.: Eigenspannungen und vertfestigung beim messing. Proceedings of the second international congress of applied mechanics, Zurich, Switzerland, pages 332–5, 1926.
28. Masing, G.: Influence of nonlinear spring behavior of friction on dynamic characteristics of a rolling guide-way. Journal of Advanced Mechanical Design, Systems, and Manufacturing, 9(1), 2015.
29. Piskan, I., Janssens, T., Al-Bender, F., and Pupaza, C.: Experimental investigation of tangential contact stiffness and equivalent damping. Proceedings in Manufacturing Systems, 7(1), 2012.
30. Hartog, J. D.: Forced vibrations with combined viscous and coulomb damping. Philosophical Magazine, 7(9:59):801–817, 2009.
31. Gola, M. and Gastaldi, C.: Understanding complexities in underplatform damper mechanics. Proceedings of ASME Turbo Expo 2014: Turbine Technical Conference and Exposition, 2014.
32. Bufler, H.: Zur theorie der rollenden reibung. Ingenieur-Archiv, 27(3):137–152, May 1959.
33. Guyan, R. J.: Reduction of stiffness and mass matrices. AIAA Journal, 3(2):380, 1965.
34. Amontons, G.: De la resistance cause dans les machines, tant par les frottemens des parties qui les composent, que par roideur des cordes qu'on y employe, et la maniere de calculer l'un et l'autre. Mmoires de l'Acadmie royale des sciences, pages 206–222, 1699.

CITED LITERATURE (continued)

35. Ollerton, E. and Haines, D.: Contact stress distribution on elliptical contact surfaces subjected to radial and tangential forces. Proceedings Institution of Mechanical Engineers, 177(95):204–260, 1963.
36. Masing, G.: Zur heynschen theorie der verfestigung der metalle durch verborgen elastische spannungen. Wiss Veroffentl aus dem Siemens-Konzern, 3(1):231–9, 1923.
37. Boussinesq, J.: Application des potentiels l'tude de l'quilibre et du mouvement des solides lastiques. Gauthiers-Villars, 1885.
38. Radzevich, S. P.: Geometry of Surfaces: A Practical Guide for Mechanical Engineers. John Wiley & Sons, 2013.
39. Totten, G. E.: Steel heat treatment handbook, Second Edition. CRC Press, 2006.
40. Bhadeshia, H. and Honeycombe, R.: Steels: Microstructure and Properties, Third Edition. Butterworth-Heinemann, 2006.
41. Typical poisson's ratios for some common materials. engineeringtoolbox.com. <http://www.engineeringtoolbox.com>, Retrieved 31 March 2016.
42. Bouc, R.: Forced vibrations of mechanical systems with hysteresis. Proceedings of the fourth international conference on nonlinear oscillations, Prague, Czechoslovakia, 1967.
43. Popov, L.: Contact Mechanics and Friction. Physical Principles and Applications. Springer-Verlag, 2010.

VITA

NAME	Francesco Beccarisi
<hr/>	
EDUCATION	
	Master of Science in Mechanical Engineering”, University of Illinois at Chicago, July 2016, USA
	Master of Science in Mechanical Engineering, July 2016, Polytechnic of Turin, Italy
	Bachelor’s Degree in Mechanical Engineering, July 2014, Polytechnic of Turin, Italy
<hr/>	
LANGUAGE SKILLS	
Italian	Native speaker
English	Full working proficiency
	2014 - IELTS examination (7.0/9)
	A.Y. 2015/16 One Semester of study abroad in Chicago, Illinois
	A.Y. 2014/15. Lessons and exams attended exclusively in English
French	Basic
	Three years of lessons in the high school
German	Studying
<hr/>	
SCHOLARSHIPS	
Spring 2016	Bosch scholarship to study German in Goethe Institute
Fall 2015	Italian scholarship for studying abroad at UIC
Fall 2015	Italian scholarship for TOP-UIC students
<hr/>	
TECHNICAL SKILLS	
Basic level	HTML5 programming
Average level	Industrial systems organization and management/ Optimization design for additive manufacturing/ PID controller assembling and testing
Advanced level	Gearbox design/ Solar panel plant design

VITA (continued)

WORK EXPERIENCE AND PROJECTS

Sep 2015 - Dec 2015	PID controller assembling and testing project for Mechatronics course
Sep 2015 - Dec 2015	Mechanical differential design and modeling with Solidworks for CAD course
May 2015 - June 2016	Additive manufacturing for aerospace components project for ASP at Politecnico di Torino
Jan 2015 - June 2015	Turbine wind gearbox design project for Machine Design course
Jan 2015 - June 2015	Solar panel plant design for Advanced Engineering Thermodynamics course
Mar 2014 - Apr 2014	Training to non-destructive testing with magnetic particles at ByTest (TUV)
Jan 2014 - June 2014	Logistic administration of an industrial warehouse project for Industrial Plants course
Aug 2012 - Sep 2014	Internship at OTM Consulting (Guildford, UK)
